QUANTITATIVE ANALYSIS OF DISTRIBUTED ACOUSTIC SENSING DATA FOR TIME-LAPSE VERTICAL SEISMIC PROFILING AND MULTIPHASE FLOW MONITORING

by

Aleksei Titov

A thesis submitted to the Faculty and the Board of Trustees of the Colorado School of Mines in partial fulfillment of the requirements for the degree of Doctor of Philosophy (Geophysics).

Golden, Colorado

Date ______________________

Signed: ______________________

Aleksei Titov

Signed: ______________________

Dr. Ge Jin
Thesis Advisor

Golden, Colorado

Date ______________________

Signed: ______________________

Dr. Paul Sava
Professor and Department Head
Department of Geophysics

ABSTRACT

Distributed acoustic sensing (DAS) technology has proven to be extremely valuable in oil and gas industry applications, such as seismic imaging, completion monitoring, and production monitoring. However, quantitative analysis of DAS data is necessary to realize the full potential of the technology. Furthermore, the benefit of DAS technology comes from multiple usages of the same fiber. Hence, this thesis aims to advance the acquisition, processing, and interpretation of DAS data for the following applications in different stages of a well life cycle: time-lapse vertical seismic profiling (VSP) during completion operations, and multiphase flow monitoring during production.

In the first part of the thesis, we developed a processing workflow to quantitatively analyze unique time-lapse DAS VSP datasets acquired after each hydraulic fracturing stage. This workflow inverts properties of transmitted PS-waves observed in the field data to the geometrical and physical characteristics of the stimulated rock volume (SRV). For each VSP dataset, the PS-wave is generated due to the interaction of the incident P-wave from the surface seismic source with the SRV, which can be represented as a temporary low-velocity anomaly. We found that the analysis of the PS-waves can constrain SRV height, SRV width, and fracture closure time. First, we applied the developed workflow in a single well completion case and then validated this workflow with 2D finite-difference time-domain (FDTD) modeling. Next, we extended it to a case of zipper-fracturing stimulation, when multiple wells are completed simultaneously. Finally, we showed and validated with 3D FDTD modeling that the previously developed workflow can be used to invert SRV properties in a fiber well and adjacent wells. Our work provides critical information to optimize hydraulic fracturing operations.

We then used laboratory experiments to advance DAS acquisition and analysis for multiphase flow monitoring, focusing on a slug flow, one of the most common flow types in

both wells and surface facilities. The slug flow consists of two phases — a gas phase Taylor bubble and a liquid phase slug. Such flow type can be damaging to facilities; consequently, active flow monitoring is essential and can reduce operational costs through proactive facility management. We built a vertical flow loop facility equipped with air/water inlets, a thermal injection apparatus, and a wrapped single-mode fiber to research slug flow. The flow loop allows the study of acoustic and thermal energy propagation within the slug flow using DAS. After data processing, two moveouts were observed in the data, one associated with the thermal slug, propagating at water velocity, and another with Taylor bubbles, propagating at air velocity. Therefore, by applying our workflow, we demonstrate that velocities of both liquid and gas phases can be measured. Furthermore, the same workflow can be applied to field data.

As a next step, we modified the flow loop and added a special bubble-generating apparatus, which allowed us to study the rising Taylor bubbles in a controlled environment. We explored how DAS response changed with bubble size. We confirmed that no velocity change is observed due to bubble size difference, and DAS can be used as a pressure gradient sensor to estimate the size of Taylor bubbles. Additionally, we demonstrated that DAS is a valuable laboratory tool because it captures spatially distributed processes, such as Taylor bubbles merging, in more detail than is possible with conventional point sensors.

The thesis shows that DAS is a unique tool for reservoir monitoring. Time-lapse VSP allows for characterization of SRV during well stimulation, including the case of multiwell completions. Later in the life of the well, the same fiber cable can be used for flow monitoring, which was studied in a controlled laboratory environment for the slug flow case.

TABLE OF CONTENTS

LIST OF FIGURES

LIST OF TABLES

ACKNOWLEDGMENTS

First of all, I am genuinely thankful to my advisor, Dr. Ge Jin. I knew if I had any problem or concern related to scientific and professional development, Dr. Jin would be there to help and advise. Dr. Jin has been a great example to follow as a scientist, advisor, and person.

I am thankful to my committee members. To Dr. Ali Tura for accepting me to the program within Reservoir Characterization Project (RCP) consortium to start a new Fiber Optic Research Program and for advising me for the first two years in the program. To my minor advisor in Petroleum Engineering (PE) department, Dr. Jennifer Miskimins, for opening a new and exciting world of hydraulic fracturing via course taught and discussions we had. To Dr. Jeffrey Shragge, who was a great source of knowledge to answer my numerical modeling questions and for his suggestions to improve the manuscript. To Dr. Reza Hedayat for his support, interest in my work, and excellent chairship during a number of the committee meetings we had. To Dr. Gary Binder for the collaborative work and help during his time at RCP and after that.

I am thankful to RCP faculty, staff, and students. To Dr. Jim Simmons for help and discussions from the very beginning of the program. To Melinda Gale and previous RCP program managers Sue Jackson and Noelle Vance for their administrative support during the program. To Larry Irons for his IT support and my development in the IT field. To Dr. Yesser Haj Nasser for his helpful input. To all RCP students for camaraderie within the group, and my collaborators Kagan Kutun, Youfang Liu, and Diana Tomayo for their contributions. I want to thank all RCP consortium company members for their financial support and the fruitful discussions we had during our biannual meetings. I thank Geophysics and Petroleum Engineering faculty and staff for their support during the program, especially Geophysics Department manager Michelle Szobody for her support and

Dr. Yilin Fan for help on theoretical and laboratory aspects of flow monitoring.

Also, I want to thank my colleagues outside the Mines community for their influence on my professional development and interesting discussions on DAS and geophysics, including Dr. Jonathan Ajo-Franklin, Dr. Nate Lindsey, Dr. Veronica Rodriguez Tribaldos, Dr. Julia Correa, and Dr. Feng Cheng, whom I met during my two summer visits to Lawrence Berkeley National Laboratory, Dr. Vikram Jayaram and Dr. Shuang Zhang at Pioneer Natural Resources, and Dr. Konstantin Osypov, Dr. Vladimir Kazei, Dr. Andrey Bakulin, Dr. Ezzedeen Alfataierge and Dr. Ali Aldawood whom I met during my internships at Aramco Research Center in Houston.

Finally, I am infinitely thankful to my family for their love and support. To my parents Nadezhda and Valerii, my brothers Arsenii and Evgenii, and their families. To my beloved wife Anna who made this journey over the seas with me, for her love, support, and continuous inspiration to move forward to future achievements.

CHAPTER 1
INTRODUCTION

Distributed acoustic sensing (DAS) technology utilizes conventional telecommunication or specially engineered fiber-optic cable [e.g., 1, 2] as a sensor array [3]. DAS systems consist of the interrogator unit (IU) and fiber-optic cable. The IU, which has a laser onboard, sends one or several laser pulses (a pulse train) into the fiber cable [3]. Then, at each point of the cable, light is scattered by density inhomogeneity within the fiber core, either natural or induced (in the case of engineered fiber). Rayleigh scattering forces light to scatter without changing the light frequency. A small portion of the light energy scatters backward and propagates back to the IU, and a photodetector within the IU captures the backscattered photons. Also, the IU measures the time delay between the outgoing pulses and incoming photons. As the speed of light within a particular type of fiber is known (about $n = 1.45$ times slower than the speed of light in a vacuum), the IU can calculate the location along the fiber cable from where the photons were scattered using the optical time domain reflectometry (OTDR) principle. The IU also measures the optical phase change $\Delta\phi$ observed in the backscattered light. This phase change is linear to the applied longitudinal strain ε_z [3]:

$$\Delta\phi = \frac{4\pi n \xi L_g}{\lambda}\varepsilon_z, \tag{1.1}$$

where n is the refractive index, $\lambda = 1550$ nm is the probe laser wavelength, $\xi \approx 1.7$ is the photo-elastic coefficient, and L_g is the gauge length (which varies from 1 to 100 m; the most common value being about 10 m). The DAS system outputs the relative strain values averaged along the gauge length; hence, the spatial resolution of the measurement is a function of the gauge length. The IU can provide measurements with nanostrain sensitivity along >100 km fibers [4]. DAS technology makes measurements with high spatial resolution (down to 1 m) along the length of the fiber-optic cable. The laser pulse transmission and receiving process can be repeated as often as there is no interference between measurements occurring.

DAS registers strain signals in a wide band of frequencies, from 1 mHz to 100 kHz [e.g., 4, 5], demonstrating the high sensitivity to not only mechanical but also thermally induced strain at low frequencies [6]. For oil and gas, geothermal, or carbon capture utilization and storage industrial applications, the cable can be installed in a variety of ways along a borehole, such as cemented behind the casing [e.g., 7, 8], clamped to tubing [e.g., 7, 8], lowered down with wireline [e.g., 9] or even conveyed as a disposable bare fiber [e.g., 10]. Thus, DAS technology in these industries can be used for three main applications using the same fiber:

- seismic imaging and monitoring (vertical seismic profiling (VSP), microseismic, cross-well seismic);
- completion monitoring (injection allocation, low-frequency DAS); and
- production monitoring in wells and on the surface (acoustic and thermal analysis).

Not all applications are possible with all types of installations, and only permanent installation behind the casing allows a full suite of DAS applications. Moreover, the cost-effectiveness of DAS technology comes from multiple uses throughout the life span of the well. That is why in this thesis, we aim to advance DAS applications related both to the early stage of a well life cycle (well completion) and to the longest stage (production).

In the case of seismic applications, the fiber cable can be considered a line of geophones along the wellbore axis. The difference between DAS data and geophone data is in the measured quantities [e.g., 11]. Multicomponent geophones measure particle velocity in three directions. In contrast, DAS measures strain or strain rate along the direction of the fiber, resulting in a different radiation pattern from geophones [12]. The one main disadvantage is that DAS data are single component. Several ongoing studies are related to this drawback. For example, research shows that instead of using a straight fiber, one could use multiple helically wound fibers to achieve multi-component DAS measurements [e.g., 13]. DAS VSP surveys have many advantages. Two main benefits are:

- seismic wavefields are recorded along the entire fiber or well length; and
- as fiber can be cemented in place, DAS provides exceptional receiver-side repeatability for time-lapse surveys.

These benefits allow use of DAS-based VSP for offshore [e.g., 14, 15] and onshore [e.g., 7] reservoir monitoring and hydraulic fracture characterization [e.g., 16–20].

Chapter 2 of this thesis focuses on understanding how seismic monitoring can applied in hydraulic fracturing monitoring through time-lapse DAS VSP surveys. As the DAS VSP surveys are repeated after each hydraulic fracturing stage, we refer to this type of acquisition as interstage DAS VSP. The unique dataset provided by Apache Corporation allows us to investigate seismic waves scattering on the stimulated rock volume (SRV) due to hydraulic fracturing. We found that the scattered converted PS events allow for characterizing SRV anomaly. We propose a new method for calculating SRV height based on analysis of the extent of transmitted PS-waves recorded by DAS. We support our study with analytical traveltime curve derivation, 2D finite-difference time-domain (FDTD) full-wavefield modeling results, and applying our method to the field data.

Chapter 3 extends the workflow developed in Chapter 2 and applies it to another field dataset provided by Apache Corporation. In the new case, multiple wells were undergoing fracturing operations simultaneously, which complicates the analysis of the scattered events. However, we showed that the study of PS-waves converted by SRV observed during interstage DAS VSP surveys allow for SRV characterization of not only the fiber well itself, but the wells of the zipper-group, constraining the geometrical and physical properties of SRVs. 3D FDTD full-wavefield modeling confirms that the heights of the SRVs from the fiber well can be estimated and the heights and lengths of other SRVs in the zipper group can be constrained. The results can be used to constrain hydraulic fracturing numerical models and evaluate completion quality.

After demonstrating that DAS VSP could be successfully used to monitor well completion, we moved to the next critical stage of the well life cycle. We used laboratory experiments to advance multiphase flow monitoring with DAS. Production flow profiling is one of the most important potential uses of DAS data both for downhole and surface applications. Production allocation along a horizontal well can further evaluate the success of completion. This knowledge can help optimize hydraulic fracturing operations in different regions and formations. From DAS data, one can measure the speed of sound in the fluid and estimate the flow rate using the Doppler Effect [e.g., 21, 22]. Flow rate can also be calculated by sensing the slugs and turbulent eddies in the flow using DAS data [e.g., 22, 23]. A recent study demonstrated using low-frequency DAS (LFDAS) signals to track the thermal slugging in the wellbore to estimate flow velocity for low-rate oil producers [24]. The implications of these potential capabilities are substantial for the oil and gas industry. While a significant amount of work has been done for single-phase flow analysis, there is still a knowledge gap in evaluating multiphase flows.

In the following chapters of the thesis, we focus on studying DAS response to slug flow, which consists of intermittent phases of gas in the form of Taylor bubble and liquid in the form of liquid slug [25]. This flow type is one of the most common and damaging flow patterns observed in wellbores and surface facilities.

In Chapter 4, we investigate the thermal and acoustic response of DAS data to two-phase slug flow. We built a vertical flow loop test facility and equipped it with fiber optic cable wrapped along the pipe. We generated various slug flow regimes and studied the recorded DAS response. First, we found that DAS can detect the velocity of rising bubbles. Next, we added a thermal injection apparatus that introduces temperature variations in the flow. As DAS can measure minute temperature variations we could determine velocity of the thermal slug. Moreover, this velocity is found to be very close to that of the liquid phase. Therefore, we conclude that DAS can be used to extract both liquid and gas phase velocities in a two-phase slug flow.

In Chapter 5, we modified our existing flow loop by adding bubble apparatus, which can generate Taylor bubbles of pre-defined sizes and facilitate the study of two bubble interactions with DAS. We developed a workflow to extract accurate bubble velocity and apply it in experiments with different bubble sizes. We confirm with the DAS data that velocity does not change with bubble size, as predicted by classical theory [26]. Moreover, we extracted the velocity of the wake region following the Taylor bubble, which is slower than the Taylor bubble velocity. The distributed nature of DAS measurements allows for detailed analysis of the spatially distributed processes, which is difficult to monitor with the point sensors. For the study of two bubble interactions, we observed that when the second bubble enters the wake region of the first bubble, it accelerates and merges with the first bubble. Meanwhile, using quantitative amplitude analysis of DAS data, we were able to estimate the size of the Taylor bubbles. Our findings demonstrate that DAS can be used as a unique tool to study flow dynamics, and our workflow can be upscaled easily for field applications.

In Chapter 6, we summarise the main results of the thesis and discuss integration and possible future application of the gained knowledge.

CHAPTER 2

MODELING AND INTERPRETATION OF SCATTERED WAVES IN INTERSTAGE DISTRIBUTED ACOUSTIC SENSING VERTICAL SEISMIC PROFILING SURVEY

A paper published in *Geophysics*.

Aleksei Titov[1,2], Gary Binder[2], Youfang Liu[2], Ge Jin[2], James Simmons[2], Ali Tura[2], David Monk[3], Grant Byerley[3], and Mike Yates[3]

2.1 Abstract

Optimization of well spacings and completions are key topics in research related to the development of unconventional reservoirs. In 2017, a vertical seismic profiling (VSP) survey using fiber-optic-based distributed acoustic sensing (DAS) technology was acquired. The data include a series of VSP surveys taken before and immediately following the hydraulic fracturing of each of 78 stages. Scattered seismic waves associated with hydraulic fractures are observed in the seismic waveforms. Kinematic traveltime analysis and full-wavefield modeling results indicate these scattered events are converted PS-waves. We tested three different models of fracture-induced velocity inhomogeneities that can cause scattering of seismic waves: single hydraulic fracture, low-velocity zone, and tip diffractors. We compare the results with the field observations and conclude that the low-velocity zone model has the best fit for the data. In this model, the low-velocity zone represents a stimulated rock volume (SRV). We propose a new approach that uses PS-waves converted by SRV to estimate the half-height of the SRV and the closure time of hydraulic fractures. This active seismic source approach has the potential for cost-effective real-time monitoring of hydraulic fracturing operations and can provide critical constraints on the optimization of unconventional field development.

[1]Primary researcher and author
[2]Department of Geophysics, Colorado School of Mines, Golden, CO
[3]Apache Corporation, Houston, TX

2.2 Introduction

Unconventional oil and gas resources play a significant role in the hydrocarbon resource potential of the United States [27, 28]. Horizontal drilling and hydraulic fracturing are the key technologies that lead to the success of unconventional reservoirs. Horizontal wells allow larger contact areas to targeted reservoirs, while the hydraulic fracturing operation stimulates production via permeability enhancement of tight reservoir rocks. Current stimulation designs can have multiple stages along the horizontal part of the wellbore, where each stage can have multiple perforation clusters [29]. The completion design and well spacing need to be optimized to achieve the best financial results. The characterization of stimulated rock volume (SRV) is critical for this optimization.

The developed geophysical tools to characterize SRV include microseismic monitoring [30], microdeformation measurements [31], and strain measurements [32]. Microseismic emissions, excited during the hydraulic fracturing treatment, can be recorded with surface or borehole sensor arrays. Knowing subsurface velocity models, one can map the location of each event. The cloud of the events, associated with a particular stage, determines an SRV [33]. Microdeformation monitoring uses surface and borehole tiltmeters [34]. These tools can capture small subsurface deformations and provide an estimation of induced fracture geometry. Both microseismic and microdeformation methods can estimate the 3D geometry of hydraulic fractures, but with limited spatial resolution. On the other hand, fiber-optic-based crosswell strain measurements reported by [32], can provide hydraulic fracture geometry estimation with a high spatial resolution (< 5 m), but limited only to the monitor well locations.

Other techniques to characterize induced fractures use surface or borehole active seismic sources with downhole receivers. [35] present one of the first Vertical Seismic Profiling (VSP) tests to monitor changes in subsurface associated with explosive fracturing of the target zone. The survey was recorded with borehole receivers using surface sources. They observed a reduction in P- and SH-wave velocities and an increase in attenuation after fracturing. The fractured zone height was estimated as a result of the experiment. Another active source technique utilizes S-wave shadowing, which is based on a theoretical fact that no S-wave energy should transfer through open fluid-filled fractures at normal incidence [36]. In this study, borehole sources (air guns) were used to illuminate hydraulic fractures at almost normal incidence. The shadow was recorded in the offset well with seismic receivers. [36] report decreasing S-wave amplitudes for about an hour after hydraulic fracturing, which indicate the opening of the fractures. The reinforcement of S-wave amplitudes indicates fracture closure. These two examples show analyses of direct or transmitted waves. On the other hand, scattered waves, which include reflected, converted, and diffracted waves, can also be utilized to estimate hydraulic fracture properties.

The use of scattered waves for hydraulic fracture and SRV characterization was tested previously in field and lab settings. The field data were acquired with conventional geophone arrays, mostly in vertical wells. [37] demonstrate that S-waves generated on the surface could scatter on the hydraulic fractures induced from a vertical well. The scattered diffracted waves were recorded in an offset monitoring well. The authors showed how the ray-tracing and full-wavefield modeling based on the Born approximation could explain the observed results. Despite that only the phases of the recorded and the modeled wavefields were matched, the authors estimated the length and height of the fractures using the scattered waves. [38] apply full wavefield modeling based on the Kirchhoff approximation to the same dataset. In this study, both the amplitudes and phases of recorded scattered waves were matched, and more precise estimation of fracture geometry was provided. [39] demonstrate through laboratory and numerical experiments that both incident P- and S-waves generate a broad range of scattered waves, including diffracted, reflected, converted, and guided waves in a water-filled layer. The authors conclude that scattered waves measured in different configurations (i.e., VSP, crosswell, single-well) could be used to "monitor fracture growth in the field." [40] examine experimental, numerical, and analytical evidence of the interaction of seismic waves with a shared fracture. The authors show that waves, converted on a fracture from P- to S-wave can be detected and used to estimate shear stress. [41] propose a methodology to estimate the quality (opening) of hydraulic fractures from VSP survey data. The authors demonstrate in a 3D model-based study that a combination of microseismic and VSP data could provide improvement in scattered wave extraction. Time-lapse seismic response to scattered waves was utilized to determine fracture compliance and distinguish between economically significant open fractures and not important closed ones. [42] recently illustrate the use of scattered energy. The waves scattered by hydraulic fractures (coda) from microseismic sources were used to image hydraulic fractures. All these studies motivate us to understand how scattered waves can be used in an inter-stage distributed acoustic sensing (DAS) VSP survey.

DAS is a novel technology valuable for SRV monitoring. The DAS technology turns fiber-optic cable into an array of strain-rate sensors. Both conventional telecommunication and specially engineered optical fibers can be used for sensing. DAS utilizes phase-sensitive optical time-domain reflectometry [3]. The DAS interrogator unit sends a highly stable pulse (or several pulses) down the fiber cable. Due to Rayleigh elastic scattering, a small part of the incident energy scatters on natural inhomogeneities within a cable. The photodetection system within the DAS interrogator captures the backscattered photons. The interrogator unit then compares the phase difference between two points in the fiber separated by a certain length (namely gauge length, typically about 10 m). The phase difference is in direct proportion to the applied strain changes along the axial direction of the fiber at the backscattered location [3]. The interrogator assigns a strain-rate measurement to a particular point along the fiber (fiber channel) based on the traveltime delay between the incident and the backscattered energy.

DAS has a vast potential for different geophysical applications, as it has a broad (< 1 mHz to > 100 kHz) frequency response [4, 32], wide (> 100 km) aperture [43], and small (0.25 m) spatial sampling intervals [4]. Geophysical applications of DAS in the oil and gas industry typically employ borehole deployment of fiber-optic cable, which can be cemented outside casing, clamped to tubing, or installed on a wireline unit. These applications include VSP [44], microseismic monitoring [45, 46], and crosswell strain monitoring [32, 47].

DAS-based VSP has been successfully used for offshore [15, 44] and onshore [7] reservoir monitoring, as this technique provides high repeatability in time-lapse data. [16, 17, 48, 49] show the possibility of using DAS VSP to characterize hydraulic fracturing. They saw time delays in P-wave arrivals, which was attributed to P-wave slow-down in the SRV. We present a DAS-based method to estimate the half-height of SRV, which utilizes scattered waves observed during the inter-stage VSP survey.

In 2017, a VSP survey was acquired [17]. The data include a series of VSP surveys before hydraulic fracturing and shortly after the completion of each of 78 fracturing stages. The completion was done using sliding sleeve technology. The hydraulic fractures were initiated from sleeve ports. The time between adjacent stages varied from one to three hours. Two vibroseis sources were located along the horizontal well direction, and about 1.6 km from the toe and the heel of the well, as shown with red dots in Figure 2.1 (modified from Binder et al., 2020). Seismic data were recorded using DAS in the treatment well, where the sensing fiber was cemented outside the casing. DAS provides high data repeatability [50], which is crucial for time-lapse surveys. In the processed field data, time delays between stages were observed in both P- and S-wave arrivals [17, 19]. In addition, scattered waves from the hydraulic fractures are also observed [17, 19]. Understanding both observations could lead to a new cost-effective tool for SRV monitoring.

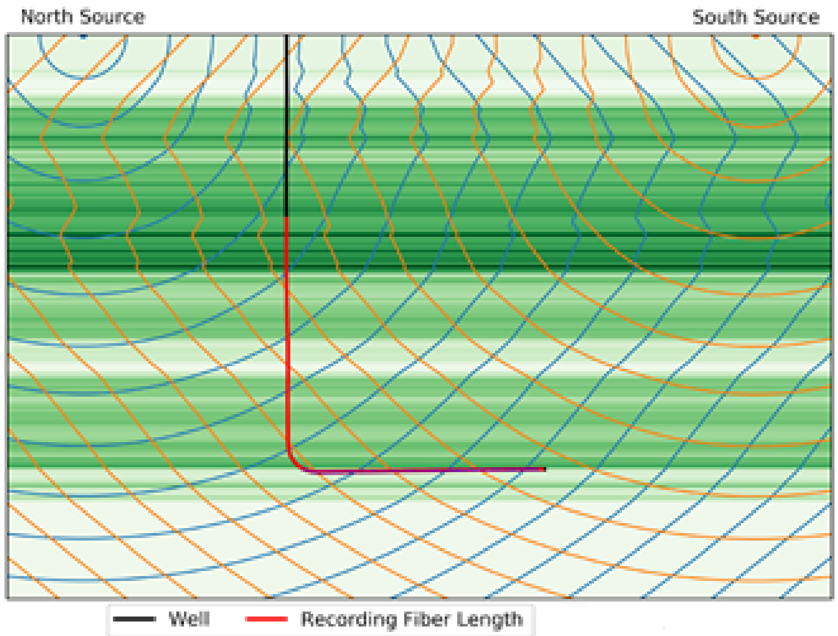

Figure 2.1 The geometry of the interstage DAS VSP survey illustrating the well (black), points along the fiber optic cable sampled by the interrogator (red), and two source locations north (blue) and south (orange) of the well. A P-wave velocity model is shown in green derived from a sonic log. Eikonal-based wavefronts are shown illustrating incident angles along the well from both sources (modified from [19]).

We focus on a detailed analysis of observed scattered waves. Figure 2.1 shows an example of an event caused by incident P-wave scattered by the SRV from a survey taken after completion of stage 30 with baseline subtracted. Time and distance axes are relative to the port location (i.e., stage center). We propose three different models of fracture-induced velocity inhomogeneities that can cause seismic waves scattering. For each model, we derive analytic traveltime equations for different modes of the scattered waves and analyze event amplitude using finite-difference (FD) modeling. Finally, we compare the synthetic results with the field data. From the scattered waves, we estimate the SRV half-height and the fracture closure time.

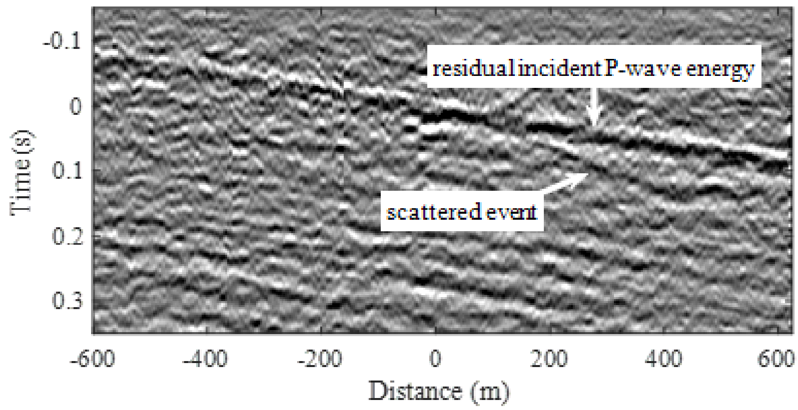

Figure 2.2 An observed scattered event in the field data. Time-lapse response from north source for VSP survey after completion of stage 30.

2.3 Modeling

We propose three different velocity models that mimic the velocity perturbation induced by hydraulic fractures: single hydraulic fracture (HF), low-velocity zone (LVZ), and tip diffractors (TD). We analyze the kinematic and dynamic properties of the scattered wavefields of these three models.

2.3.1 Models

2.3.1.1 Hydraulic fracture model

Hydraulic fractures, even of a millimeter width, can lead to relatively strong scattered events [41]. There are two approaches to model a single hydraulic fracture with FD method. The first one utilizes a non-equidistant, locally adapted grid, where the smallest cell is smaller than the fracture width. The fracture in this method is treated as water-filled cells [51]. Another approach is to use equivalent medium theory [52], where fractures are represented by anisotropic cells on a uniform grid. These cells correspond to changes in boundary conditions with a linear-slip model. [53] show that these two approaches provide nearly the same results for scattered waves. The only difference is the slow-wave traveling in the fluid layer, which is observed with the first approach but not with the second. In our modeling, we do not consider the slow-wave propagation. Also, the equivalent medium approach is more computationally efficient [53]. As a result, we adopt the latter method to construct the model.

For the background medium (BM), we use a homogeneous and isotropic medium with P-wave velocity $V_P^{BM} = 3776$ m/s, S-wave velocity $V_S^{BM} = 2200$ m/s, and density $\rho^{BM} = 2.55$ g/cm^3 derived from the well logs corresponding to the targeted reservoir. The stiffness tensor for BM in Voight notation is C_{ij}^{BM}:

$$\begin{gathered} C_{11}^{BM} = (\lambda + 2\mu), \\ C_{13}^{BM} = C_{31} = \lambda, \\ C_{33}^{BM} = (\lambda + 2\mu), \\ C_{55}^{BM} = \mu, \\ C_{15}^{BM} = C_{51}^{BM} = C_{35}^{BM} = C_{53}^{BM} = 0, \end{gathered} \tag{2.1}$$

where λ and μ are Lamé parameters of the background medium. To model a single HF of width (w^{HF}) 5 mm, we follow the equivalent medium approach and use the stiffness tensor C_{ij}^{HF} equation reported in [54]:

$$\begin{gathered} C_{11}^{HF} = (\lambda + 2\mu)(1 - \delta_N), \\ C_{13}^{HF} = C_{31} = \lambda(1 - \delta_N), \\ C_{33}^{HF} = (\lambda + 2\mu)(1 - r^2\delta_N), \\ C_{55}^{HF} = \mu(1 - \delta_T), \\ C_{15}^{HF} = C_{51}^{HF} = C_{35}^{HF} = C_{53}^{HF} = 0, \end{gathered} \tag{2.2}$$

with

$$r = \nu/(1 - \nu), \tag{2.3}$$

$$\delta_N = Z_N(\lambda + 2\mu)/[L + Z_N(\lambda + 2\mu)], \tag{2.4}$$

$$\delta_T = Z_T\mu/(L + Z_T\mu), \tag{2.5}$$

where ν is the Poisson's ratio of the background medium, Z_N and Z_T are the normal and tangential fracture compliances, and $L = 4$ m is the size of the numerical grids. The anisotropic cells have a horizontal symmetry axis, i.e., represent an HTI material.

For a fluid-filled fracture, $Z_N = w^{HF}/K$, where $K = 2.25$ GPa is the bulk modulus of the fluid and $Z_T = \infty$ [53]. The comparison between the values of stiffness tensor components for BM and hydraulic fracture cells indicates that the difference between C_{33}^{BM} and C_{33}^{HF} is only about 0.1%, and the differences between C_{11}, C_{13}, and C_{31} are about 1%. The most significant change is in the C_{55} component. Assuming $Z_T = \infty$, δ_T is equal to 1, and $C_{55}^{HF} = 0$. Thus, the difference between C_{55}^{BM} and C_{55}^{HF} is 100%.

Figure 2.3a shows the C_{55} homogeneous BM field. The horizontal and vertical axes correspond to distance and relative depth, respectfully. The point with coordinates (0,0) corresponds to the port location, from where the hydraulic fracture is initiated. The orange line shows a DAS optical fiber line with 1.02 m channel spacing. Figure 2.3b shows the HF model with a half-height of 200 m.

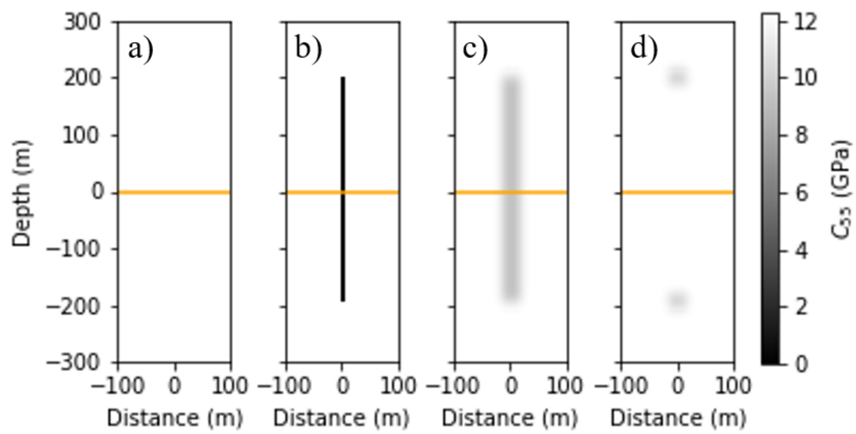

Figure 2.3 Models of velocity inhomogeneity induced by a hydraulic fracture in terms of C_{55}. (a) Background medium (BM), (b) hydraulic fracture (HF), (c) low-velocity zone (LVZ), (d) tip diffractors (TD).

2.3.1.2 Low-velocity zone model

The low-velocity zone (LVZ) model, first introduced by [55], includes a LVZ surrounding the hydraulic fracture. The LVZ can be created by two possible mechanisms. First, the seismic velocity of rocks changes with effective stress [56]. In the process of hydraulic fracturing, the pore pressure near the fracture increases, causing a drop in effective stress, and hence a reduction in the local seismic velocity. A second possibility is the creation of secondary fractures near the major hydraulic fractures [57]. In both mechanisms, one can treat the LVZ as an approximation of the SRV.

The LVZ causes delays in P- and S-wave arrival times between the monitor survey acquired after completion of each stage and the baseline. Our starting LVZ model has P- and S-wave velocities 20% slower than BM. The LVZ has 20-m width and 200-m half-height. We also apply a triangular filter to smooth the LVZ boundary, as shown in Figure 2.3c.

2.3.1.3 Tip diffractors model

The tip diffractors (TD) model was inspired by finite-element modeling of fracture propagation [58] and strain signals observed in low-frequency DAS data recorded in the monitor well during a treatment process [32]. Both studies show that a zone with strong extensional stress exists close to the hydraulic fracture tip, which leads to a localized decrease of seismic velocity. We use the same algorithm to generate the TD model as we did for the LVZ model. We assume that the size of each diffractor is 20 m by 20 m. The diffractors are co-located with fracture tips 200 m away from the well. We decrease velocity for each box by 20% in comparison with the BM, as shown in Figure 2.3d.

2.3.2 Kinematics analysis

We derive traveltime equations for different modes of seismic waves and explain how moveouts change with the change of fracture half-height h. To simplify the problem, we assume an incoming seismic wave propagates in a homogeneous isotropic BM. The wave impinges from the left with the angle of incidence θ that is measured from the normal to the DAS receiver line. The model h is measured from the fiber to the upper tip of the model, and the model width is w. The receiver coordinate $x = 0$ m corresponds to the port location (see Figure 2.4).

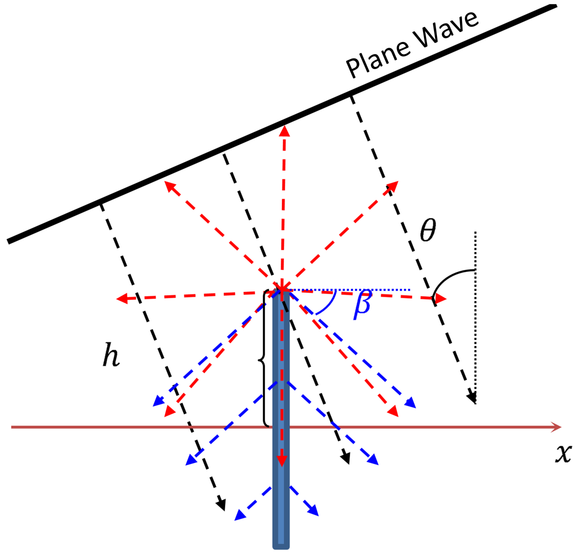

Figure 2.4 An incident P-wave impinges the model with half-height h and width w. Diffracted PP- and PS-waves from the top tip are shown in red. Converted reflected and transmitted PS-waves are shown in blue. Diffracted pure and converted waves from the bottom tip are not shown.

Using ray theory and assuming that the fracture plane, which defines model orientation, is perpendicular to the receiver line, we derived traveltime equations for the scattered wavefields. We define $t = 0$ s as the arrival time of the incident wave to the port location ($x = 0$ m). Below, we consider the selected traveltime equations for scattered PS modes:

$$t_P^i = \frac{\sin\theta}{V_P^{BM}} x, \tag{2.6}$$

$$t_{PS}^d = -\frac{h\cos\theta}{V_P^{BM}} + \frac{\sqrt{x^2 + h^2}}{V_S^{BM}}, \tag{2.7}$$

$$t_{PS}^c = \left(-\frac{\cos\theta\tan\beta_{PS}}{V_P^{BM}} + \frac{1}{V_S^{BM}\cos\beta_{PS}}\right) \mid x \mid, \tag{2.8}$$

where t_P^i corresponds to incident wavefield, t_{PS}^d to diffracted PS wavefield, and t_{PS}^c to converted wavefields (reflected and transmitted). The incident angle for converted PS-wave β_{PS} is defined from the Snell's law:

$$\frac{\sin(\pi/2 - \theta)}{\sin\beta_{PS}} = \frac{V_P^{BM}}{V_S^{BM}}. \tag{2.9}$$

It can be seen from equation 2.7 that the diffracted-wave arrival time depends on the SRV half-height h. So, it may be theoretically possible to estimate h from diffracted wave moveout. However, as we show later, the diffracted waves are weak and can hardly be used for the SRV half-height estimation. Equation 2.8 for transmitted and reflected waves does not have h as a parameter. Nevertheless, we still can use these scattered modes to determine h. The reflected and transmitted scattered waves are detectable only in a limited number of DAS channels. For example, reflected and transmitted PS-waves are detected only on the interval

$$x \in [-s_{PS}, s_{PS}], s_{PS} = h/\tan\beta_{PS}, \tag{2.10}$$

where s_{PS} is the "shadow" of converted PS-wave. Consequently, we can use this shadow to characterize the SRV half-height using the scattered wave signal in an inter-stage DAS VSP. To determine h, we need to extract the length of PS-wave shadow. The shadow of transmitted/reflected scattered modes starts at the port location and ends where these modes merge with corresponding diffracted modes. After we determine s_{PS}, we can calculate h combining equation 2.9 with 2.10:

$$h = \frac{V_S^{BM}}{V_P^{BM}} \frac{\cos\theta}{\sqrt{1 - \left(\frac{V_S^{BM}}{V_P^{BM}}\right)^2 \cos^2\theta}} s_{PS}. \tag{2.11}$$

Solving equation 2.11 for s_{PS} allows us to calculate the PS-wave shadow for the given model's half-height. The calculated s_{PS} for $h = 200$ m is equal to 387 m. To illustrate how moveouts change with SRV half-height, we plot the traveltime curves of two SRV models with different half-height in Figure 2.5. Figure 2.5a-Figure 2.5d illustrates the traveltime curves for $h = 50$ m, while Figure 2.5e-Figure 2.5h for $h = 200$ m. In this example, we assume that the far-field source is located to the left from the fracture location, and the plane-wave incident angle is 41°.

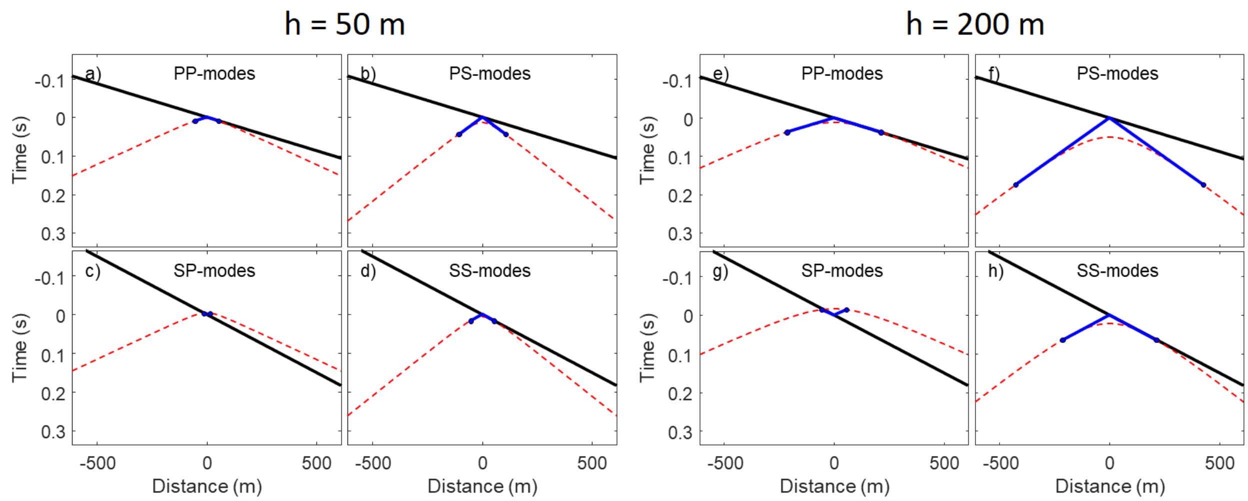

Figure 2.5 Traveltime curves for (a,b,c,d) $h = 50$ m and (e,f,g,h) $h = 200$ m. Black lines correspond to (a,b,e,f) incident P-wave or (c,d,g,h) S-wave. Blue lines show converted, transmitted, or reflected modes. Red dashed lines show diffracted events.

Figure 2.5a,b,e,f show PP-modes (incident P, diffracted PP, transmitted and reflected PP), PS-modes (incident P, diffracted PS, transmitted and reflected PS). Figure 2.5c,d,g,h show SP-modes (incident S, diffracted SP, transmitted and reflected SP), and SS-modes (incident S, diffracted SS, transmitted and reflected SS), respectively. All blue curves with the positive distances are transmitted waves, and the ones with the negative are reflected waves.

In this survey, the estimated central frequency from the extracted wavelet is about $f_c \approx 30$ Hz. The P-wave wavelength $\lambda_P^{BM} = V_P^{BM}/f_c \approx 126$ m, and S-wave wavelength $\lambda_S^{BM} = V_S^{BM}/f_c \approx 73$ m. The width of the inhomogeneity is much less than the P- and S-wavelengths for all three models. It means that kinematic results will be the same for the HF and the LVZ models. For the TD model, the reflected and transmitted waves are not generated, and only diffracted waves are considered (red lines in Figure 2.5).

We subtract baseline to observe time-lapse effects in the field data. Some residual energy of incident wave preserved in the time-lapse seismogram (see Figure 2.2). This energy may interfere with some scattered modes, make it challenging to observe non-diffracted PP-, SP-, and SS-modes (blue lines), which arrive right before or after the incident wave (black lines). The most promising modes to extract model's half-height are reflected and transmitted PS-waves.

2.3.3 Numerical simulation and dynamic analysis

One may analytically derive the amplitudes of converted, reflected, and transmitted waves for the HF model [59]; however, for the other models and diffracted waves, it can be challenging. We ran FD elastic modeling for each model to verify our traveltime equations and estimate the scattered to incident waves amplitude ratio. We adapt *sfewefdm* program within the *Madagascar* package to simulate the seismic wave propagation in isotropic and anisotropic media [60]. We use the models presented earlier in Figure 2.3 with a grid cell size of 4 m. A vertical acceleration source was placed -2500 m to the left and -2856 m above the port location. A Ricker wavelet with a center frequency of 30 Hz is selected as the source function. We calculate the seismic wavefields in terms of x component of the displacement field, $u_x(x)$, along the horizontal receiver line with 1.02 m increments. $u_x(x)$ is then converted to DAS measurement $\dot{\varepsilon}(x)$, assuming a gauge length L_g of 16 m, using [3]:

$$\dot{\varepsilon}(x) = \dot{u}_x(x + L_g/2) - \dot{u}_x(x - L_g/2). \tag{2.12}$$

Figure 2.6 shows the DAS record for BM (a) and each model (b-d) for incident P-wave, and Figure 2.7 for S-wave, with the BM subtracted. The amplitudes were normalized by those of the incident P- or S-wave. The amplitude scales in all panels are kept the same. The half-height of each model is 200 m, which corresponds to traveltime curves shown in Figure 2.5e-h. Figure 2.8 shows the maximum amplitude distribution of the scattered energy for different models. They were automatically picked using the Hilbert transform. We discuss P-wave scattering first. The most energetic are the reflected and transmitted PS-waves. For the HF model, the amplitude of scattered PS-waves is very high (blue line Figure 2.8a). The amplitude distribution is symmetric for reflected and transmitted waves. The rapid decay in amplitude is observed for $\mid x \mid > 400$ m, which is about $s_{PS} = 387$ m, calculated using equation 2.11. At these locations, the reflected and transmitted PS-waves merge with the diffracted PS-wave. On the other hand, for the LVZ model, we see an asymmetric behavior. More energy is observed in the "transmitted" part (for $x > 0$). The amplitude achieves a maximum value of about 20% of incident wave amplitude. The TD model shows that all diffraction waves are very weak.

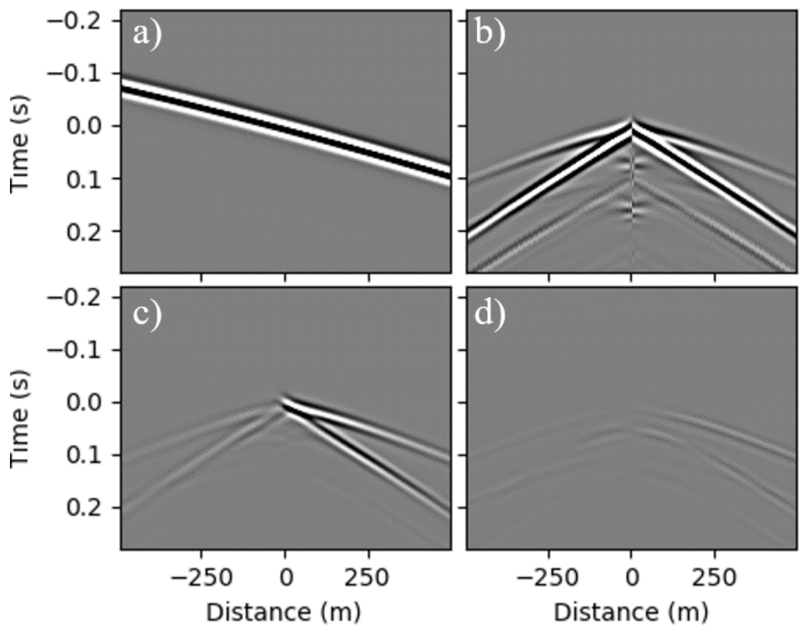

Figure 2.6 Synthetic DAS record. (a) Incident P-wave for BM, and scattering of the P-wave on (b) HF, (c) LVZ, and (d) TD models.

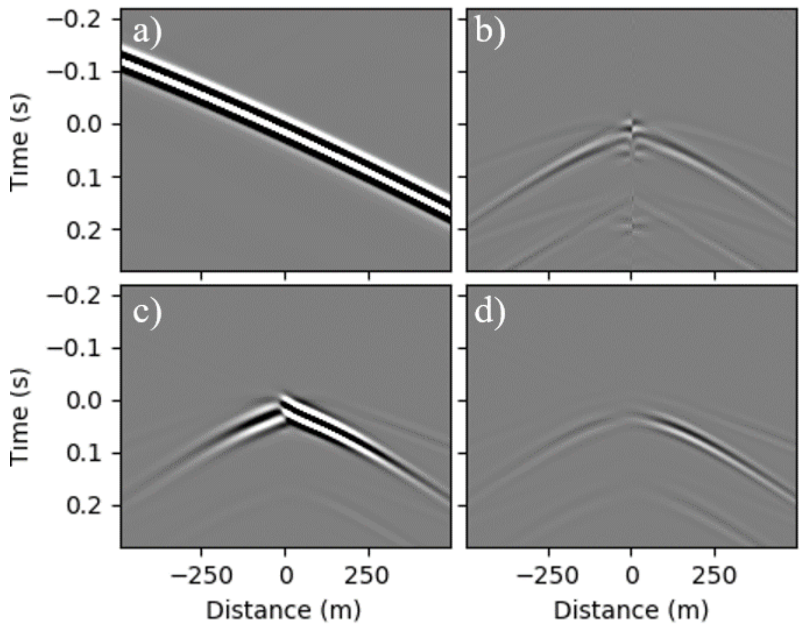

Figure 2.7 Synthetic DAS record. (a) Incident S-wave for BM, and scattering of the S-wave on (b) HF, (c) LVZ, and (d) TD models.

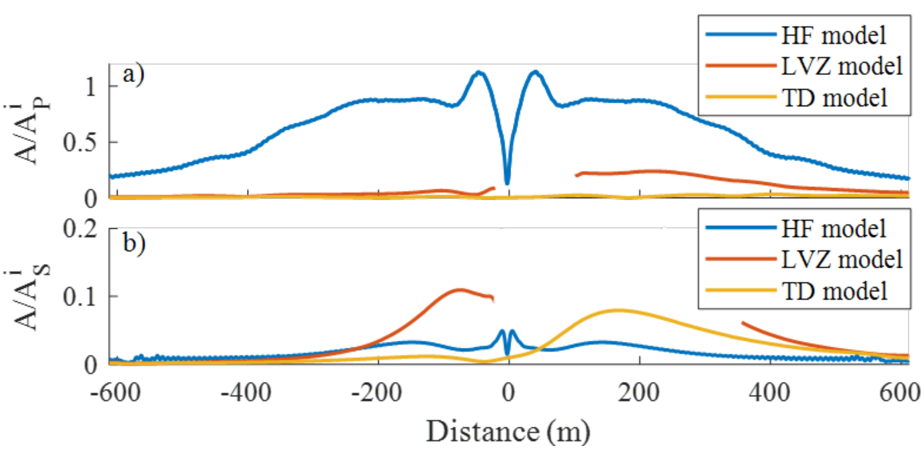

Figure 2.8 Amplitudes of (a) scattered PS- and (b) SS-modes normalized by the amplitudes of incident P- and S-waves for different models. For the LVZ model, part of the amplitudes is muted as they are disturbed by the interference with the delayed incident wave.

For the incident S-wave, we observe most energy for transmitted SS-modes for LVZ and TD models. However, these modes interfere with the delayed incident S-wave, which disturbs the actual amplitude values after baseline subtraction. So, the amplitude values for transmitted S-waves are not reliable. For the HF model, the amplitudes of scattered waves do not exceed 5% of the incident S-wave amplitude.

We qualitatively compared the results derived from our modeling with the field observation of the scattered waves, as shown in Figure 2.2. The LVZ model best fit the data due to the similar amplitudes of scattered events and asymmetry in the response. To quantitatively investigate how different parameters of the LVZ model influence the seismic response, we ran a series of sensitivity tests. We varied the velocity contrast (ΔV), half-height (h), width (w), and smoothness (σ) of the LVZ. The smoothness is an artificial modeling parameter that affects the transition in velocities between BM and LVZ. Table 2.1 shows the variation of the parameters. Figure 2.9 shows the results of the sensitivity analysis. We do not trust PS-wave amplitude close to the port location as it is disturbed by the interference with other modes. The analysis shows that the amplitude distribution of scattered waves is sensitive to all parameters mentioned above. The arrows in Figure 2.9 indicate these variations. The amplitude is directly proportional to velocity contrast (Figure 2.9a) and half-height (Figure 2.9c) and inversely proportional to smoothness (Figure 2.9d). The dependence of the amplitude to the model width is non-linear and has a maximum at about 36 m or $\lambda_P/4$. While the response is asymmetric relative to the port location, the shifted symmetry axes can be found. These axes are shown in Figure 2.9 with the dashed lines.

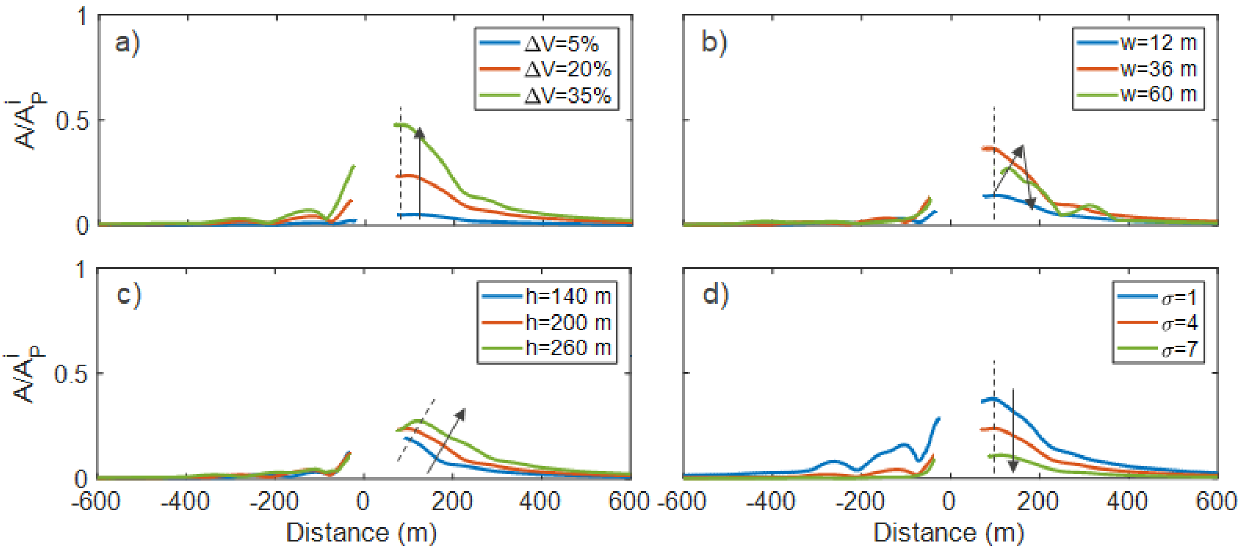

Figure 2.9 Amplitudes of scattered PS-modes normalized by the amplitudes of the incident P-wave. Sensitivity tests to (a) velocity contrast, (b) width, (c) half-height, and (d) smoothness. Dashed lines show the shifted symmetry axis, and arrows illustrate the change in amplitude with a parameter increasing. Part of the amplitudes close to the port location ($x = 0$ m coordinate) is muted as they are disturbed by the interference with the delayed incident wave.

Table 2.1 LVZ model parameters. Bold values are kept fixed while varying another parameter.

ΔV (%)	h (m)	w (m)	σ
5	140	12	1
10	160	16	2
15	180	**20**	3
20	**200**	24	**4**
25	220	28	5
30	240	32	6
35	260	36	7
40	280	60	8

2.4 Field data observations and interpretation

2.4.1 Data acquisition and processing

The data include a series of VSP surveys before hydraulic fracturing and shortly after the completion of each of 78 fracturing stages. The field geometry is shown in Figure 2.1 (modified from Binder et al., 2020). Two vibration points were located about 1.6 km from the toe and the heel of the wellbore. Two vibes were sweeping on each location from 4 Hz to 80 Hz for 15 s with extra 4 s of recording time. VSP data were acquired prior, after, and in between 78 fracturing stages. 20 sweeps or more were made each time at each vibration point. There are 158 total correlated stacked seismograms to be processed and analyzed. The recording was done with the 2015 generation interrogator unit. The gauge length was selected to be 16 m. The spatial sampling is 1.02 m, providing 3200 channels distributed along the vertical and horizontal parts of the well.

To achieve the optimal signal-to-noise ratio (S/N), the data were processed in the following order: first, we removed interrogator noise common across all DAS channels, as explained by [61]. To do this, we subtracted the median trace formed from DAS channels in the vertical well subsection. Second, correlation with the vibroseis sweep and stacking was made. Then, to further suppress noise, *f*-*x* deconvolution, dip filtering, and a 4 Hz to 90 Hz band-pass filter were applied [19]. Finally, the baseline was subtracted from all monitor seismograms for each source.

2.4.2 Observations and interpretation

We applied a post-processing workflow to enhance the S/N of scattered transmitted PS-waves. The workflow is based on applying *f*-*k* filtering to differently flattened data. The illustration of our workflow for the VSP survey after stage 30 is shown in Figure 2.10. First, we flatten the data along the incident P-wave arrival. The *f*-*k* spectrum and seismogram are shown in Figure 2.10a and Figure 2.10d. Negative wavenumbers correspond to upgoing, and reflected PS-wave energy. Hence, the flattened incident P-wave propagates with infinite apparent velocity across the fiber channels. The residual incident P-wave energy is centered around $k = 0$ 1/m in f-k plots. We zeroed all $k < 0.002$ m^{-1} to suppress the residual incident P-wave and upgoing energy. Next, we put zeros above the incident P-wave arrival and flatten the data along scattered transmitted PS-waves. After that, we kept only $-0.003 < k < 0.003$ m^{-1} to filter out the downgoing waves propagated with velocities different from transmitted PS-wave (see Figure 2.10c). The result of this post-processing workflow is shown in Figure 2.10f. The scattered event is observed in the relative time of 0.13 s. Also, a second-order scattered multiple is observed in the relative time of 0.23 s.

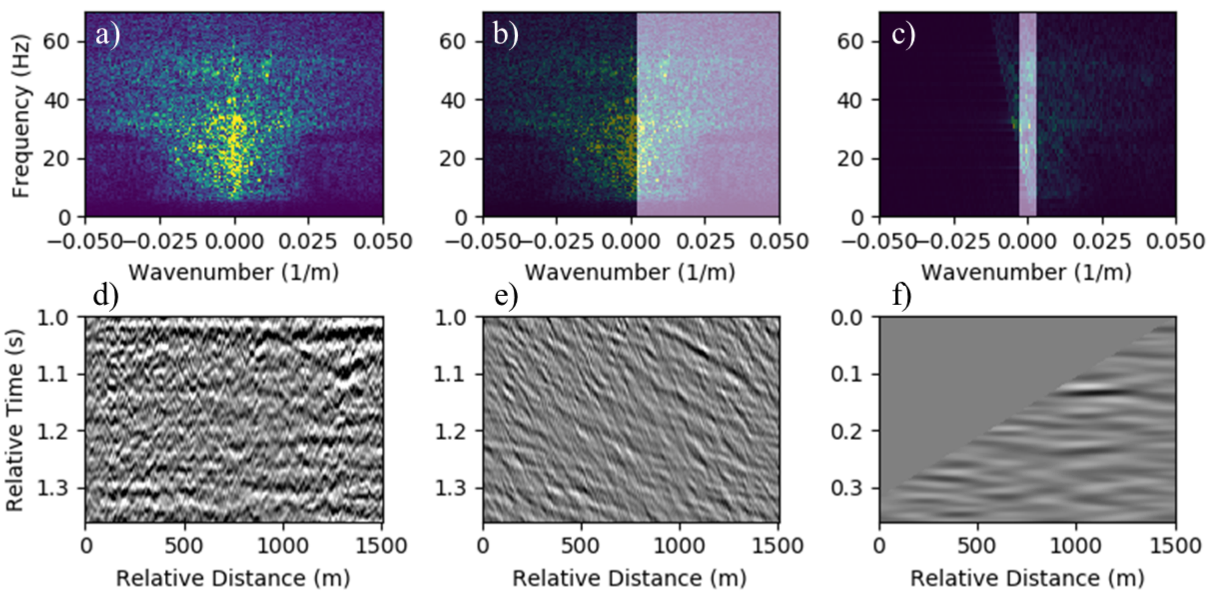

Figure 2.10 Post-processing workflow to increase S/N of PS-wave shown in Figure 2.2. (a,b,c) The f-k spectra with applied masks and (d,e,f) corresponding seismograms for (a and d) flattened incident P-wave data, (b and e) flattened incident P-wave data after filtration of direct arrival and (c and f) upgoing energy, and flattened transmitted PS-wave data.

After the post-processing, the scattered waves from the incident P-wave can be observed from several stages. Figure 2.111a,b,c show the processed flattened transmitted PS-wave data for north source after stage 30, 45, and 60. The top axis shows the port number derived from the port location. Using the known incident P-wave arrival time, we correlate the relative time to the port number. We use Figure 2.11a to clarify the axes. The scattered event indicated by the blue arrow is observed in relative time 0.13 s from a relative distance of 820 m, corresponding to port 29. The same procedure can be applied to the VSP survey after stage 45 (Figure 2.11b) and stage 60 (Figure 2.11c). The corresponding times and ports for events indicated by orange and green arrows are 0.19 s (port 42) and 0.25 s (port 58), respectively. Port numbers do not match the VSP survey number. This observation indicates that scattered PS-waves endure for some time.

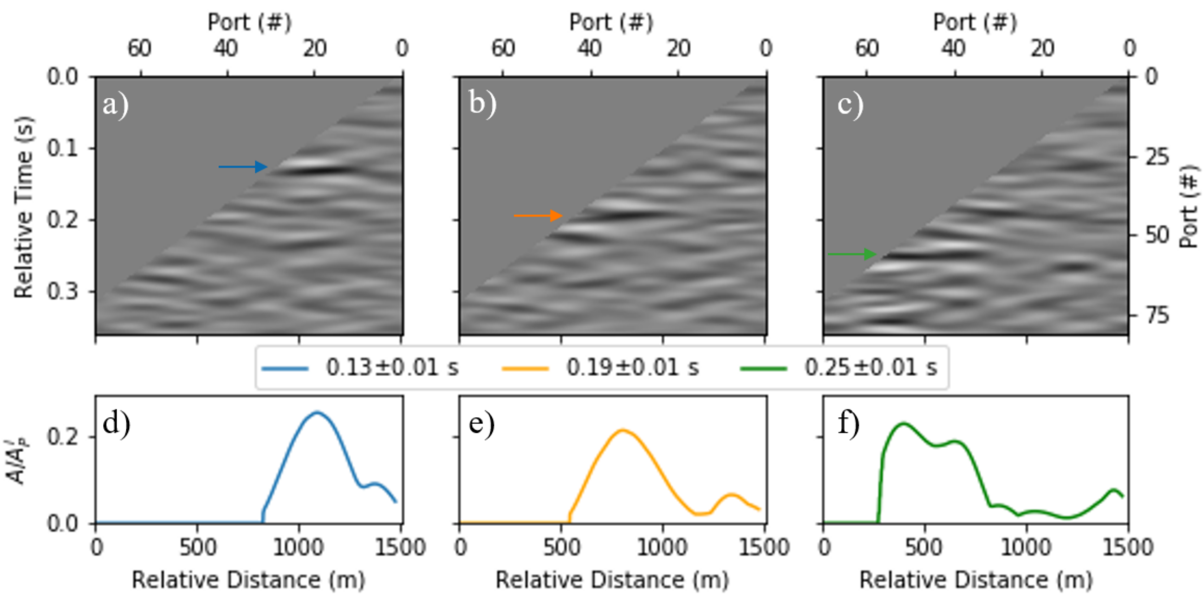

Figure 2.11 Scattered events observed in the field data for north source after completion of (a) stage 30, (b) stage 45, and (c) stage 60; (d,e,f) corresponding amplitude slices for different relative times or port locations.

The bottom row of Figure 2.11 shows corresponding distribution of the absolute value of minimum normalized amplitude in a 20 ms time window centered on relative times of 0.13, 0.19, and 0.25 s for VSP surveys after stage 30 (Figure 2.11d), 45 (Figure 2.11e), and 60 (Figure 2.11f). These amplitude curves allow extracting the shadow of transmitted PS-waves. However, with the current data quality, it is challenging to precisely pick the point where the shadow ends. Our shadow length uncertainty is about 20 m. Table 2.2 shows the length of the estimated shadows and calculated half-heights using equation 2.11.

The angle of incident θ was determined using a ray-tracing analysis, as shown in Figure 2.1. The field amplitude curves are very similar to the amplitude curves for the LVZ model, shown in Figure 2.8. Assuming stage 29 SRV half-height is 245 m, $w = 20$ m, and modeling parameter $\sigma = 4$, the rough estimation of velocity variation between SRV and undisturbed rock is about 25%.

Table 2.2 Estimated PS-wave shadows and SRV half-heights from north source for VSP surveys after stage 30, 45, and 60.

VSP survey after stage (#)	Port (#)	θ (°)	s_{PS} (m)	h (m)
30	29	37.9	473 ± 20	245 ± 10
45	42	34.4	566 ± 20	310 ± 11
60	58	30.7	526 ± 20	304 ± 12

As a final step of our interpretation, we stacked the amplitudes along transmitted PS-wave moveout for each time-lapse seismograms for north and south sources. The result of this procedure is shown in Figure 2.12. The top subplots show the stacked seismogram for the north (Figure 2.12a) and south (Figure 2.12b) sources. Each vertical trace here represents a single seismogram, shown in Figure 2.11, stacked along the relative distance axis. The top axis represents the timeline of fracturing. As the well was completed using sliding sleeve technology, the average speed of completion was ten stages a day. We are interested mostly in the response above the diagonal black line, which represents a VSP survey after completion of a particular stage versus corresponding to this stage port number. The noise below this line is caused mainly by multiples of scattered PS-waves. We observe three major events in north source data indicated by arrows. The same events are observed in south source data. Also, in the south source data, we observe multiple events before stage 20, which are not visible in the north source data. We do not see them in the north source, as we did not record the full length of the scattered events due to the fiber termination at the toe of the well.

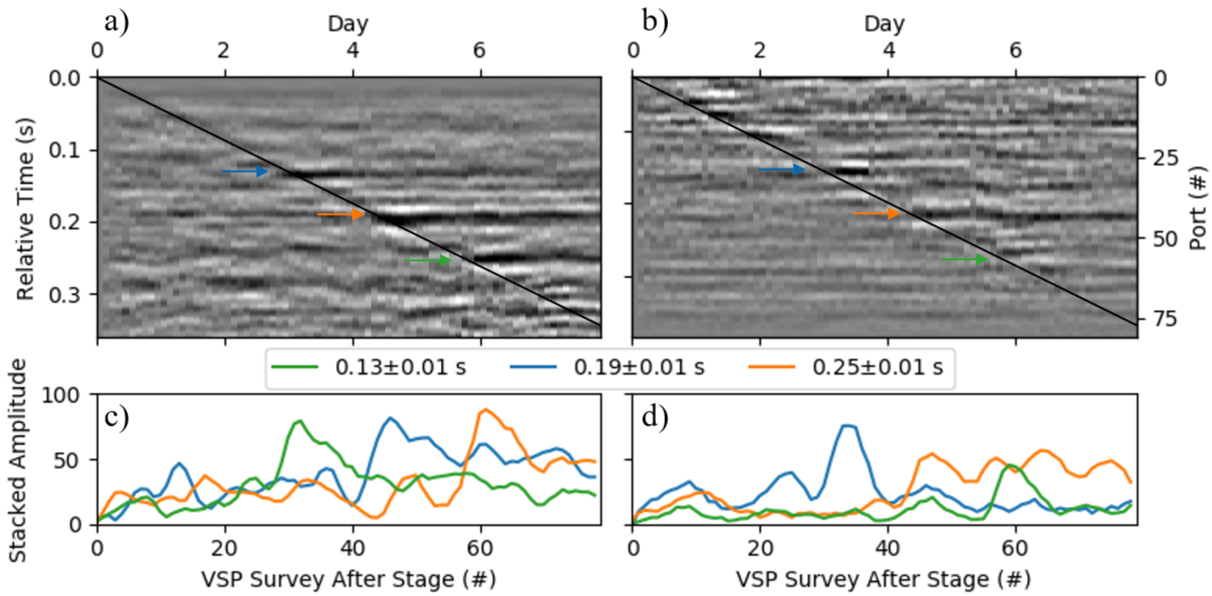

Figure 2.12 Amplitude stack along transmitted PS-wave moveout of the scattered events for (a) north and (b) south sources; (c and d) correspond to amplitude slices. Three major events were observed for both sources initiated after stage 28, 42, and 56. The diagonal black line represents the VSP survey vs. the port number.

The bottom row of Figure 2.12, similar to Figure 2.11, shows the distribution of the absolute value of minimum normalized amplitude in a 20 ms time window centered on relative times of 0.13 s, 0.19 s, and 0.25 s for north (Figure 2.12c) and south (Figure 2.12d) sources. The amplitude response for north source is similar for all of the three events. The maximum values of stacked amplitude also are approximately the same. Considering the response for relative time 0.13 s, we see that time-lapse signal initiated after stage 29. After stage 31, it reaches the maximum amplitude, after which it decays. After stage 42, it returns to the background noise level. However, the time-lapse response is still visible for the rest of the experiment, which may indicate that some fractures remain open. The response for relative time 0.19 s, which corresponds to SRV generation at stage 42, decays slowly than the one generated at stage 29. Analysis of the amplitude decay time can provide us with insight into the fracture closure rate. The amplitude response for south source looks differently with significantly varying maximum amplitudes. The cause of this could be the incident P-wave, which for the south source travels in previously stimulated rock. Further investigations and modeling work are needed to interpret the observed responses fully.

2.5 Discussion

The proposed method for estimating SRV half-height and the closure time of hydraulic fractures involves the analysis of the seismic waves scattered by SRV and recorded with DAS during completion. [17] and [19] demonstrate that the time delay is observable and can be used to constrain both SRV half-height and leak-off time. Figure 2.13 shows the half-height estimation derived from scattered-wave analysis overlaid with the prediction of SRV half-heights from [19]. While the results are comparable, scattered-wave analysis indicates lower half-heights. The time-delay analysis is based on changes in velocity along the raypath from the surface to the fiber; therefore, multiple SRVs associated with different frac stages can contribute to the observed time delay for a particular frac stage. In contrast, for the scattered waves, the seismic response is more localized in its nature. If SRVs are further apart than a 1/4 of an S-wave wavelength, then the responses from adjacent SRVs can be separated.

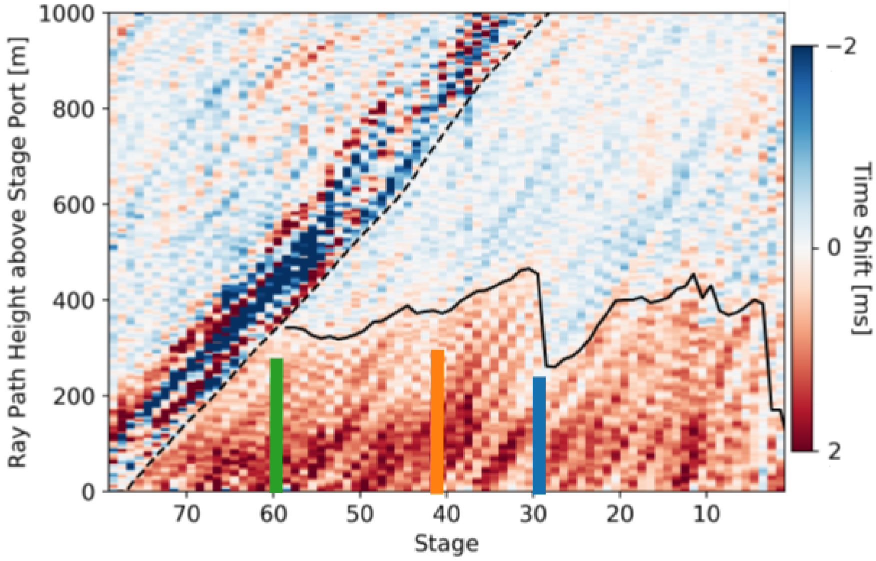

Figure 2.13 Time-shifts in incident P-wave (modified from [19]). The solid black line shows the estimation of SRV half-height from the incident P-wave shadow. The zone of unreliable time shift estimation due to poor fiber angular sensitivity in the heel of the well falls to the left from the dashed line. Blue, orange, and green bars show the estimated SRV half-heights from scattered transmitted PS-wave analysis.

The LVZ model provides the best description of the field data. This model causes the asymmetric response in scattered PS-waves. Another possible model that can describe asymmetric results with reasonable amplitudes is found in [40]. The authors introduce coupling fracture stiffness in the HF model, which causes asymmetric amplitude distribution in transmitted and reflected PS-waves. However, only the LVZ model can lead to a significant time delay in incident wave arrival presented in [17]. The velocity gradient within the LVZ model may relate to the secondary fractures proposed by [57]. In the LVZ model, the amplitude of the converted PS-wave depends on multiple parameters, including velocity contrast and geometric characteristics of the SRV. These parameters can be used to constrain hydraulic fracture models.

We see great potential in using inter-stage DAS scattered wave analysis for real-time completion optimization, especially with the current achievements in fiber design and DAS interrogator technology. A new generation of interrogators and the specially engineered optical fiber are available on the market. The new systems could provide up to a 100x increase in S/N [1]. These advancements in DAS technologies should allow us to interpret the scattered events more quantitatively. With increased fiber sensitivity, even a single sweep could provide enough S/N to observe scattered PS-waves. In another direction of development, with increased instrument sensitivity, other scattered modes (such as diffracted pure and converted waves) potentially could be used. Moreover, the scattered events can be generated not only by an active surface source but also by microseismic events and perforation shots. [62] show that SRV length can be estimated using perforation shots from an adjacent well. Hence, with further advancements in the technology and data interpretation, one may be able to perform real-time monitoring of SRV.

Future work will target automatic inversion for SRV parameters. The ultimate goal is to connect the SRV characteristics with completion efficiency and production. Other possible applications for using scattered events will include analysis of zipper-frac treatment, estimating proppant placement, and leak-off distribution.

2.6 Conclusions

We derived traveltime equations and performed numerical modeling to interpret the observed scattered events in the inter-stage distributed acoustic sensing (DAS) vertical seismic profiling (VSP) data. The results indicate the events in the data are converted PS-waves. The low-velocity zone (LVZ) model, which represents a stimulated rock volume (SRV) around hydraulic fractures, provides the best description of the data, as it matches recorded field amplitudes of scattered reflected and transmitted PS-waves. Because the converted PS-waves can be observed only in a limited range of DAS channels, one can estimate the half-height of SRV by mapping the DAS channel through a simple ray-tracing model. In the field data, we observed three major scattered events by stacking along the transmitted PS-wave moveout to increase the S/N and understand the distribution of the scattered events. The estimated half-height of SRV from these three events ranges from

245 m to 310 m. Each event lasts more than a day. The stacked amplitude decay time is related to the fracture closure rate and indicates the permeability of the stimulated reservoir.

2.7 Acknowledgments

We thank Apache Corporation for providing the seismic data and permission to present it. We also thank members of the Reservoir Characterization Project (RCP) at the Colorado School of Mines for their financial support.

2.8 Data and materials availability

Data associated with this research are confidential and cannot be released.

CHAPTER 3

DAS TIME-LAPSE VSP ANALYSIS FROM ZIPPER-FRACTURING OPERATIONS: OBSERVATIONS, MODELING, AND INTERPRETATION

A paper submitted to *Geophysics*.

Aleksei Titov[1,2], Ge Jin[2], Gary Binder[3], and Ali Tura[2]

3.1 Abstract

Recent advances in distributed acoustic sensing (DAS) technology allow active seismic monitoring of stimulated rock volume (SRV) development. This study showcases an inter-stage DAS vertical seismic profiling (VSP) survey acquired during a zipper-fracturing stimulation. Incident P-waves scattered by the SRV and converted to S-waves are observed in the data. The signals are associated not only with hydraulic fracturing stages of the instrumented well, but also with fracturing of an adjacent well in the zipper group. A workflow is developed to monitor and characterize the SRV, fracture closure time, and interactions between zipper wells. 3D full wavefield modeling confirms the data interpretation and provides additional insight. As a result, we have been able to estimate SRV properties, including SRV height, width, and the fracture closure time for all wells within the zipper group. Moreover, for adjacent wells the length and azimuth of SRV can be constrained. Our work provides critical information for optimizing hydraulic fracturing operations.

3.2 Introduction

Production from unconventional reservoirs play an essential role in world energy markets. The optimization of completion operations is crucial in developing these

[1]Primary researcher and author
[2]Department of Geophysics, Colorado School of Mines, Golden, CO
[3]Automated Seismic LLC, Santa Clarita, CA

reservoirs. A common way to reduce completion cost is to use a zipper-fracturing design. This design involves simultaneous stimulation of multiple wells within the same pad. The positive economic impact comes from reducing rig time and potentially creating optimal fracture geometry [63].

Hydraulic fracture geometry is usually derived from pressure measurements and fracture propagation models; however, such results may have significant uncertainty [64]. Several established methods can constrain the models by mapping the geometry of hydraulic fractures and stimulated rock volume (SRV) [e.g., 65]. For example, microseismic monitoring [e.g., 66], also known as passive seismic, uses the seismic energy generated by small earthquakes during well stimulation to estimate the fracture geometry. Active time-lapse seismic surveys [e.g., 67] can also be used to monitor hydraulic fracture stimulation. Non-seismic techniques include electromagnetic imaging of conductive proppant [e.g., 68], fluid and proppant tracers [e.g., 69], and tiltmeters [e.g., 34].

A novel technique for fracture monitoring is distributed acoustic sensing (DAS). This technique utilizes telecommunication or engineered fiber-optic cable and turns it into a dense array of single-component strain-rate sensors along the cable length [3]. The cable can be cemented behind the casing [e.g., 7, 8], clamped to tubing [e.g., 7, 8], installed on a wireline along a horizontal well [e.g., 9], or bare fiber can be pumped through the well [e.g., 10]. The cable permanently installed behind the casing along the instrumented well provides a highly repeatable measurement of the seismic wavefield [e.g., 70]. More importantly, the data acquisition can occur during the completion operation of the well. Signals from various physical processes can be captured by DAS to monitor and evaluate the efficiency of hydraulic fracture treatment. Using DAS one can detect and characterize microseismic events [e.g., 71, 72], study near-wellbore conductivity using perforation shots [e.g., 73, 74], analyze acoustic noise from fluid injection to estimate cluster efficiency [75], and the fracture-induced strain field from adjacent wells observed in low frequency (LF) part of DAS spectrum (< 0.05 Hz), so-called LFDAS [32]. In addition to all applications mentioned above to monitor completion operations, DAS can also be used for time-lapse vertical seismic profiling (VSP). In case of horizontal wells profiling becomes far from vertical, but historically the name still holds.

Running VSP surveys before and after each completion stage, one can obtain a dynamic characterization of the stimulated reservoir. [16, 17, 19, 48, 76] showed that inter-stage DAS VSP data indicate time delays of incident P- and S-waves due to the fracturing of the instrumented well. The slow down occurs due to the low-velocity zone (LVZ) around the created hydraulic fractures. In this study, we define the rock volume in which elastic properties were changed during the stimulation as SRV [55]. [20] analyzed the scattered waves in similar interstage VSP data, acquired after each stage of hydraulic fracturing. The authors demonstrated that the scattered waves are P-waves converted to S-waves by the velocity contrast induced by SRV due to hydraulic fracturing process. The study shows that these signals can be used to estimate the SRV height. In this work, we extend the previous studies [19, 20] and analyze the scattered wave energy detected in the fiber well, which is caused by the treatment of a zipper-fracturing group of three wells. We then conduct a series of numerical modeling experiments to quantitatively interpret the scattered events in more detail.

3.3 Survey and data description

In 2018, inter-stage DAS VSP surveys were conducted using an instrumented well equipped with engineered fiber-optic cable. The cable is installed behind the casing and cemented in place. These surveys monitor the hydraulic fracturing operation of a three-well zipper group located in the Midland Basin. Figure 3.1 illustrates zipper wells and the survey geometry, with Figure 3.1a showing the map view and Figure 3.1b showing the gun-barrel view. The wells target different formations (A, B, and D as indicated in the well names), and were completed using a plug-and-perf design. The pumping time of each stage varies from 2 to 3 hours.

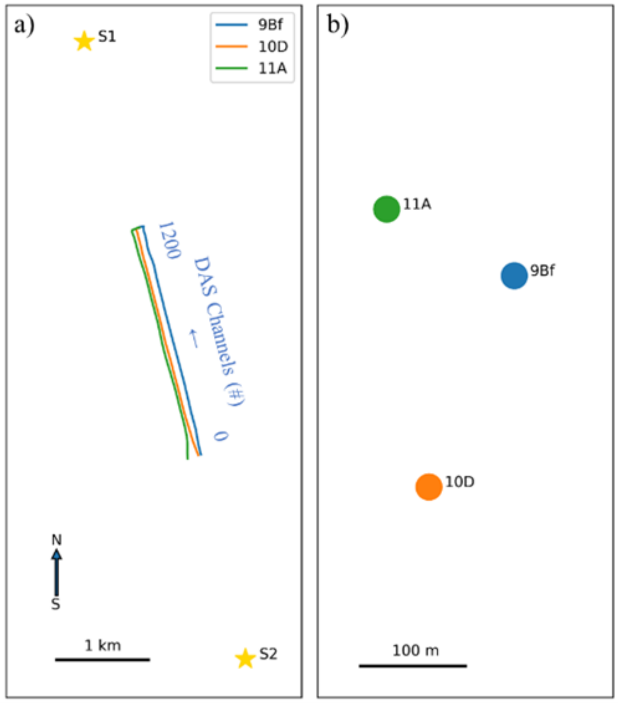

Figure 3.1 Well and survey geometries. (a) Map view. Source locations and well geometries are indicated. (b) Gun-barrel view (looking northward). Well locations are indicated.

The well 9Bf, indicated in blue color, is the instrumented well with engineered fiber-optic cable cemented behind the casing. Two shot points were used during fracturing, with each shot point location consisting of two vertical vibrators working simultaneously to increase S/N. The S1 source location was about 2.0 km to the NNW from the heel of the well. The S2 source location was about 2.4 km to the SSE from the toe of the well. The DAS data were acquired with a receiver spacing of 2 m and a time sampling interval of 2 ms (after downsampling). The interstage DAS VSP survey was composed of 60 VSP surveys for each shot point, including nine baseline VSP surveys before 9Bf treatment, 46 VSP surveys after each fracturing stage of 9Bf well, and five surveys after 9Bf completion to monitor leak-off. However, the baseline surveys do not represent undisturbed reservoir conditions in this case as other wells were being fractured before and during the acquisition time.

The side view of the wellbore geometries is shown in Figure 3.1a. Rhombi in Figure 3.1a illustrates the fracture initiation locations (center of the stages) before VSP survey 25, which is selected for demonstration. Figure 3.1b shows the completion timing, where the vertical axis corresponds to time and the horizontal axis to the distance along the wellbore, similar to Figure 2a. The relative time zero in Figure 3.1b corresponds to VSP survey 25. This shot was taken after completion of stage 16 of the 9Bf well, about 3 hours after completion of stage 12 of well 10D, and about 7 hours after completion of stage 30 of well 11A.

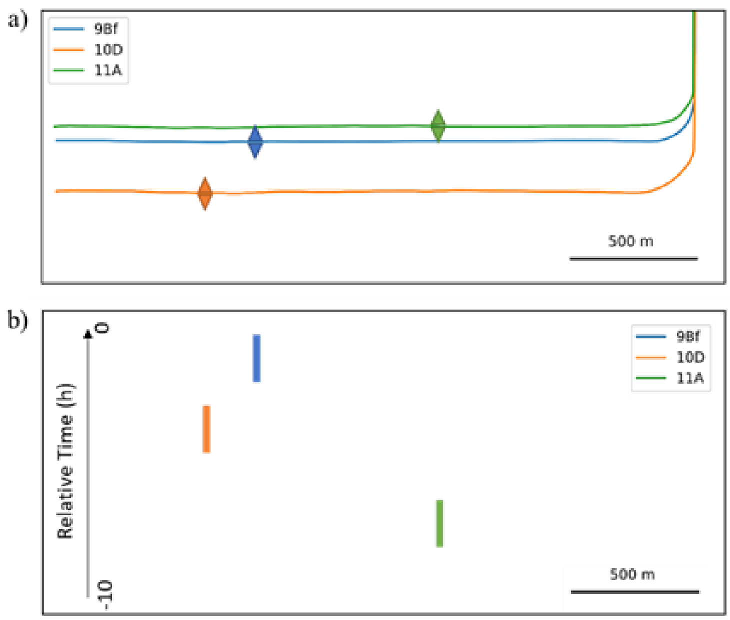

Figure 3.2 (a) Location of initiation ports (side view looking westward) and (b) relative completion timing of the zipper-group wells for VSP survey 25 taken after completion of stage 16 of well 9Bf, stage 12 of well 10D, and stage 30 of well 11A.

3.4 Field data analysis

3.4.1 Data processing

The data exhibited improved SNR compared to previous examples found in the literature [17, 20, 49], and 4D effects can be even seen in the individual sweeps without stacking. This improvement was primarily attributed to the use of the engineered fiber-optic cable, which significantly increase the energy of Rayleigh backscattering [1, 2]. The data input to our analysis were provided after applying a 4D processing sequence to optimize S/N and enhance stage-by-stage time-lapse effects. The processing sequence includes interrogator noise removal from uncorrelated records, correlation with the applied sweep, stacking of all seismograms corresponding to particular fracturing stage, and mild noise suppression followed by spiking deconvolution. All processing steps were carried out within each stage individually.

To analyze time-lapse effects the baseline data was generated by averaging the nine baseline VSP records. Stage average time shifts and amplitude operators were used to match each stage to the baseline. These latter steps were useful in suppressing unwanted time-lapse effects caused by weathering conditions and small location changes in the seismic vibrators. Finally, the baseline seismogram was subtracted to obtain the waveform difference.

An example of a time-lapse seismic response is shown in Figure 3.3. The time-lapse data correspond to VSP survey 25 from source S2 (the toe source, located to the left in Figure 3.2a). The shot was taken immediately after completion of stage 16 of well 9Bf. Earlier in time, stage 12 for well 10D and stage 30 for well 11A had been completed, as is shown in Figure 3.2b. The transmitted PS-wave (PS_T) through the SRV is clearly observable at the fiber well. The transmitted PP-wave (PP_T) is also visible; however, it interferes with the residual incident P-wave, as they arrived at almost the same time with a slight delay of about 1 ms. The reflected PS-wave (PS_R) from the SRV is very weak, which is consistent with observations presented by [20]. We focus on PS_T waves in this paper, which we will also refer as transmitted PS scattered events.

3.4.2 Scattered events analysis

In this dataset, transmitted PS-waves scattered at SRV can be observed for every stage of the fiber well in the time-lapse response. [20] show that these waves can be used to estimate half-height of SRV generated due to the fiber well completion. In this study, we

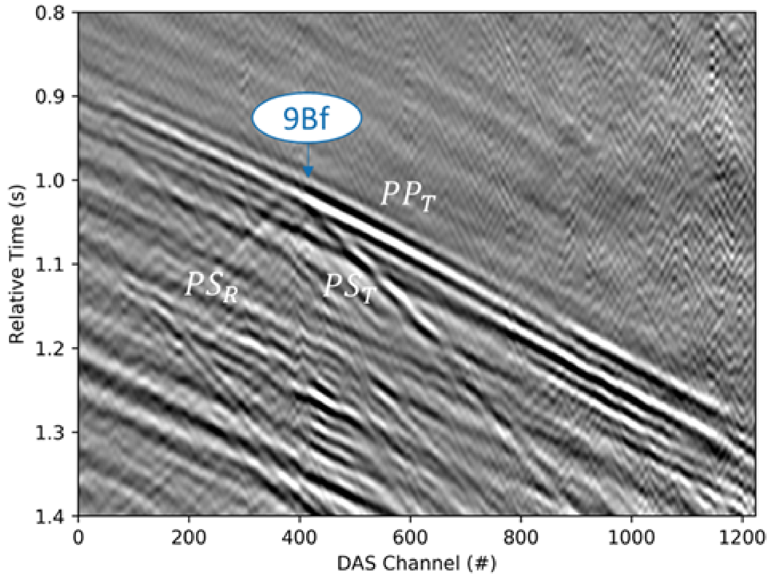

Figure 3.3 Time-lapse response from VSP survey 25 (baseline is subtracted) from source location S2 (see Figure 3.1).

demonstrate that similar analysis can be applied not only to the SRV created by the fiber well, but also to the SRV created by adjacent wells.

The processing workflow developed by [20] is applied to make scattered PS-waves more visible: first, the incident P-wave arrival was flattened using a linear moveout correction. Next, an *f*-*k* filter was used to suppress the residual incident P-wave energy by filtering out all wavenumbers larger than the chosen threshold. After that, data was flattened along transmitted PS-wave moveout, using the linear moveout method with shear-wave velocity extracted from the sonic log. The signal was bandpass filtered in wavenumber domain to leave only transmitted PS-wave energy. Finally, all residual noise arriving before the incident P-wave arrival was masked. The result for VSP survey 25 from source S2 is shown in Figure 3.4. Here, the PS-wave extent, i.e., the distance along the fiber which can sense the PS-waves, is defined as the PS-wave shadow.

To estimate the half-height for any stage one can use [20]:

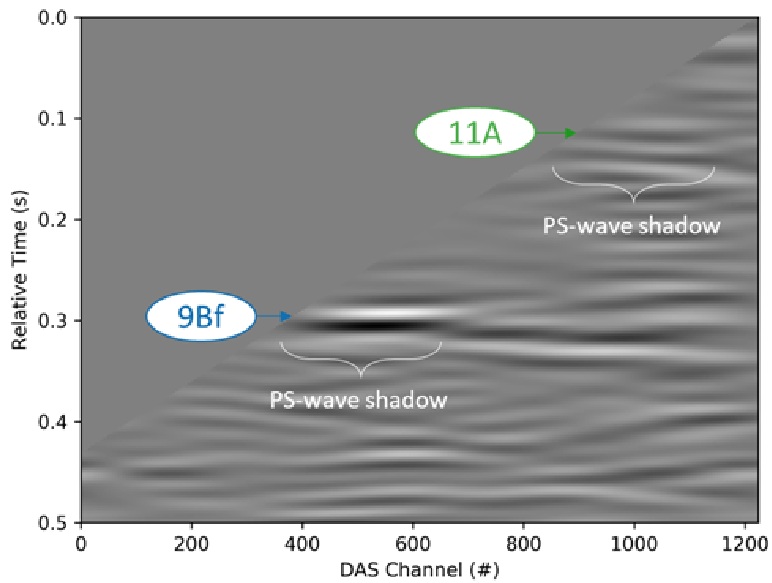

Figure 3.4 Time-lapse response from VSP survey 25 (baseline is subtracted) from source location S2 after applied post-processing workflow. Transmitted PS-wave shadows (s_{PS}) are highlighted for SRVs from wells 9Bf and 11A.

$$h = \frac{\cos\theta}{\sqrt{1 - \left(\frac{V_S^{BM}}{V_P^{BM}}\right)^2 \cos^2\theta}} s_{PS}, \tag{3.1}$$

where θ is angle of incidence, V_S^{BM} and V_P^{BM} is the S-wave and P-wave background medium velocity (averaged reservoir velocity before hydraulic fracturing stimulation), and s_{PS} is the length of PS-wave shadow. The shadow started at P-wave arrival time, and the extent of the shadow is determined by its half-height (h). The amplitude of scattered events does not disappear sharply, as the transmitted PS-wave gradually merges with the diffracted PS-wave. This nature of the scattered events brings complexity to the shadow length extraction. Also, the model simplifies the scattered wave propagation in a homogeneous layer with reservoir velocities, which applies to our case only to some extent.

The scattered event for well 9Bf is observed for a relative time of 0.3 s. It starts from DAS channel 400 and lasts for about 290 DAS channels, which given 2 m channel spacing equals to 580 m. Using Equation 1 we can estimate the half-height for this well, which is about 250 m. The scattered event for well 11A becomes visible at a relative time of about 0.14 s, and is weaker than the event for 9Bf well. Note that stage 30 for well 11A was completed about 7 hours before the VSP shown in Figure 3.3 and Figure 3.4, and therefore the impedance contrast could have dissipated with time. The average half-height for adjacent well 11A was estimated at about 250 m. Note for this analysis, half-height is defined as the fracture height above the instrumented well, which means that to calculate true half-height (fracture height above the injection well depth) for an adjacent well, vertical offset needs to be added or subtracted accordingly. Scatter events from 10D cannot be observed, which indicates that the SRV created by well 10D may not reach the fiber at well 9Bf.

To analyze the distribution of the scattered events of all the stages, we stacked the data shown in Figure 3.4 along the DAS channel direction for each time-lapse VSP survey. The results of this procedure are shown in Figure 3.5a and Figure 3.5b for source points S1 (the heel source) and S2 (the toe source), respectively. The horizontal coordinate in this type of plot corresponds to VSP shot number. The vertical axis is similar to Figure 3.4, i.e., relative time after applying transmitted PS-wave flattening procedure. Each vertical trace represents one VSP survey, and maximum energy of this trace is related to the transmitted PS scattered event.

To explain the plots, we consider survey 25 from source S2. After stacking the seismogram shown in Figure 3.4, we receive a trace with amplified amplitudes corresponding to scattered events. We observe scattered events from well 9Bf in corresponding relative times (0.14 s for S1 and 0.30 s for S2) for VSP shot 25 (horizontal axis). The plot also indicates that scattered PS-waves are present for every stage as the corresponding responses migrate with the completion stage locations. Moreover, the stacked plots allow for tracking the scattered events distribution, determining their duration, and quantitatively analyzing the stacked amplitudes.

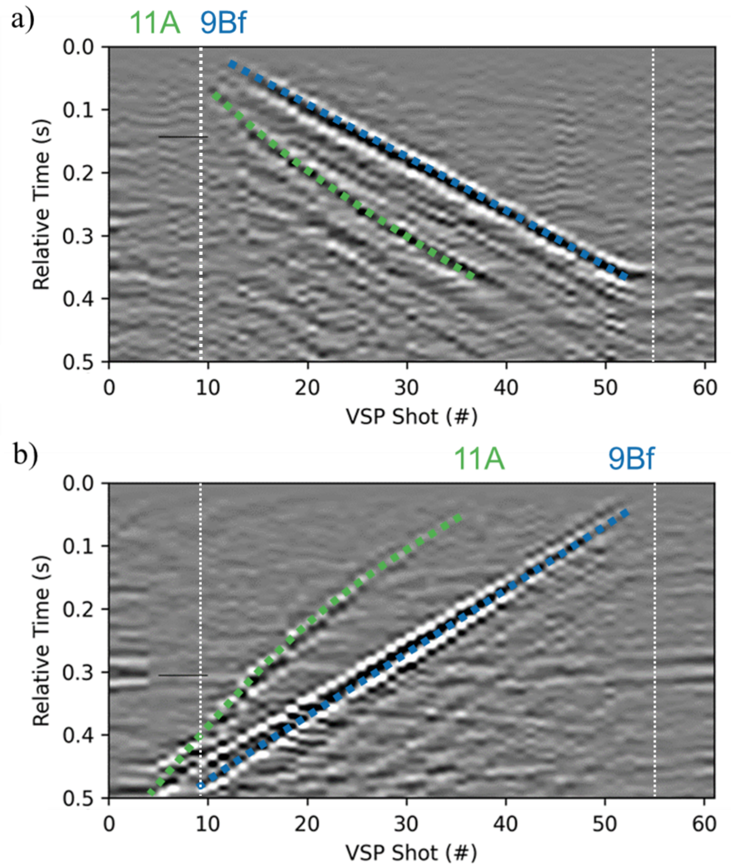

Figure 3.5 Scattered events distribution for (a) S1 and (b) S2 source locations. Each vertical trace represents a stacked record shown in Figure 4 along the DAS channel axis for different VSP shots. Trends for well 9Bf are highlighted in blue, and for well 11A in green. White dashed lines limit VSP shots taken during the completion of well 9Bf.

Scattered events distribution plots for both sources have a common response; however, the S/N is higher for S2, possibly due to different surface and/or near-surface conditions. We observe two prominent trends, one follows the completion of instrumented fiber well 9Bf (highlighted in blue) and the other follows the adjacent well 11A (highlighted in green), which is located to the side and in the next shallower formation. Note that there is a direct relationship between relative time and distance along the fiber (see Figure 3.4). For S1 (Figure 3.5a), the earlier relative time corresponds to toe-ward stages, while for S2 (Figure 3.5b), the earlier time corresponds to heel-ward stages. That is the reason that the observed event distributions follow the trend from top left to bottom right for S1 and from bottom left to top right for S2. Raw scattered events distribution plots have artifacts from subtraction of the baseline in the form of horizontal bands. We mentioned that the baseline was generated by stacking nine surveys. Among these surveys there could be some which contain scattered events from other wells, hence the horizontal band artifacts can persist in all the differential data. We have filtered out the baseline bias via *f-k* filtering to generate Figure 3.5. We make sure that this procedure does not significantly affect the analyzed signals. A more robust way to suppress these signals is to acquire a baseline survey prior to any pad stimulation. We suggest this approach for further similar data acquisition projects.

The VSP surveys from 10 to 56 were shot right after the completion with uniform stage spacing for instrumented well 9Bf. Hence, the observed trend for well 9Bf is a straight line. The well 11A was completed ahead of well 9Bf (with smaller stage measured depths and larger DAS channel numbers, see Figure 3.2), and the time interval between stages increased with time (or VSP shot number), which explains the curved trend for well 11A. We can see from Figure 3.5 that the energy of scattered waves for both wells does not last much longer than the 9-hour time interval between VSP surveys. It is highly likely that the velocity anomaly associated with the created SRV diminished in about 9 hours due to pressure drop post fracking, as otherwise we should observe destructive interference among any sequential traces, which we do not observe in Figure 3.5. With accurate rock physics models, this information could be used by petroleum engineers to analyze fracture closure time and effective permeability.

The amplitudes of toe stages for S1 and heel stages for S2 are incomplete since the full length of PS_T shadows cannot be captured due to the limited fiber length. During the processing step, we corrected for DAS angular sensitivity to P-wave amplitudes using incident P-wave normalization. However, the scattered PS-wave amplitudes still can slightly vary due to differences in incident angle. Otherwise, the amplitude changes are associated with SRV properties, such as induced velocity contrast, SRV height, and width. Also, due to the 3D nature of zipper-fracturing treatment, the distance between SRV from adjacent wells to the instrumented well might influence the amplitude of scattered events. We observe that there is a general match between datasets corresponding to both source locations. The maximum effect due to fracturing of well 9Bf is observed during VSP shot #30 (taken after completion of stage 21 of well 9Bf). The differences between datasets may be due the fact that transmitted PS-waves from source location S1 (toe source, see Figure 3.1) propagate in previously stimulated rock, while for source location S2 (heel sources) in unstimulated rock. We will further discuss the interpretation of the observed amplitude variations in the 3D numerical modeling section.

3.4.3 Field data analysis summary

Analysis of scattered events shows responses from the fracturing operation in the instrumented 9Bf and adjacent 11A wells. Figure 3.6 summarizes the SRV geometries interpreted from analysis of scattered PS-waves in a gun-barrel view.

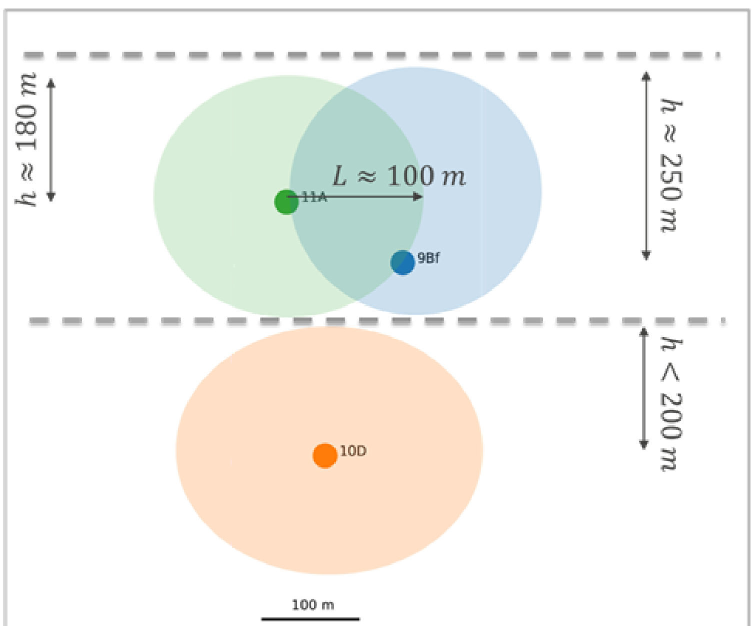

Figure 3.6 Gun-barrel view of SRV geometries estimated from analysis of scattered PS-waves.

The average half-height for SRVs due to hydraulic fracturing of well 9Bf is about 250 m, while for well 11A, it is about 180 m. The upper bound for SRV half-height induced by the fracturing of well 10D on average is less than 200 m, as we do not see a 10D response. These results imply that there could be stress barriers that control fracture height growth. These geometrical constraints provide critical information for fracture propagation models, well stacking, and well spacing decisions. The fact that scattered waves generated by well 11A SRV can be observed at well 9Bf might indicate that the average SRV half-length is more than 100 m. However, it is not entirely clear whether the SRV generated by well 11A has to reach the fiber well 9Bf in order to generate the observed signals due to ray geometry and finite-frequency effects. Moreover, the azimuth of fracture propagation can affect scattered event locations. To better understand and interpret the scatter-wave signals and answer the questions regarding SRV length and azimuth, we conduct 3D elastic modeling to simulate the wavefield.

3.5 3D modeling of scattered events

Several studies have previously conducted 2D modeling to understand interstage VSP observations [19, 20]. The geometric and elastic properties of SRV generated from different wells may vary as a function of all three spatial coordinates. Also, the fiber monitoring well can be located differently relative to SRV. Hence, to explain the zipper group interference, 3D elastic modeling can be conducted. We select the LVZ model as it provides the best field data fit [20]. The LVZ model is generated by introducing Gaussian smoothed low-velocity anomaly of particular geometrical dimensions into a homogeneous background model. The smoothing converts sharp velocity contrasts to gradient velocity variations. [77] shows that such gradient anomalies lead to asymmetric amplitude responses for transmitted PS (PS_T) and reflected PS (PS_R) waves, as observed in field data (Figure 3.3). The PS_T/PS_R ratio can be used to estimate the smoothness of the LVZ transition, which is related to SRV width [20].

3.5.1 Modeling setup

We used SOFI3D modeling code [78], which is a 3D finite-difference elastic wave simulator, to model PS-waves in 3D. We choose a homogeneous background model with the P- and S-wave velocities and density extracted from well logs of the reservoir section. The model has a grid discretization (dx, dy, dz) of 4 m. To save computational costs, we decided to generate and propagate plane waves only in the vicinity of the reservoir depth instead of simulating point sources from the surface. This effort reduces our domain size to 400x400x400 cells. To generate plane waves, we create a plane of explosive sources. The explosive sources are chosen because they do not generate S-waves in a homogeneous isotropic medium, and as a result, S waves can only be generated by a velocity inhomogeneity. This allows us to separate the converted PS-wavefield from the pure P-wavefield by applying a curl operation to the computed wavefield. We do not analyze transmitted PP-waves as they are interfering with the residual incident P-wave, and the reflected PP-waves are hardly visible in the field data. We set up a perfectly matched layer (PML) to suppress reflected waves from the model boundaries. However, the suppression was not perfect for the boundaries $Y = \pm 800$ m. To avoid the effect of boundary reflections, we only analyzed wavefields in the center of the model $-500 \leq Y \leq 500$ m.

3.5.2 Modeling results

First, we created a simple 3D model by populating the same 2D model as in [20] in the Y dimension. The velocity model, the corresponding magnitude of PS-wave particle velocity, and maximum amplitude curves (for $Y = 0$ m) are shown in Figure 3.7. The test shows similar behavior reported by [20] for the 2D case. The transmitted PS-wave has a much higher amplitude than the reflected PS-wave. Also, the X location with maximum amplitude (i.e., peak location), indicated by the yellow arrow, determines the PS-wave shadow, and can be used to calculate SRV half-height (see equation 3.1). The maximum amplitude corresponds to a location where transmitted and diffracted PS-waves merge together.

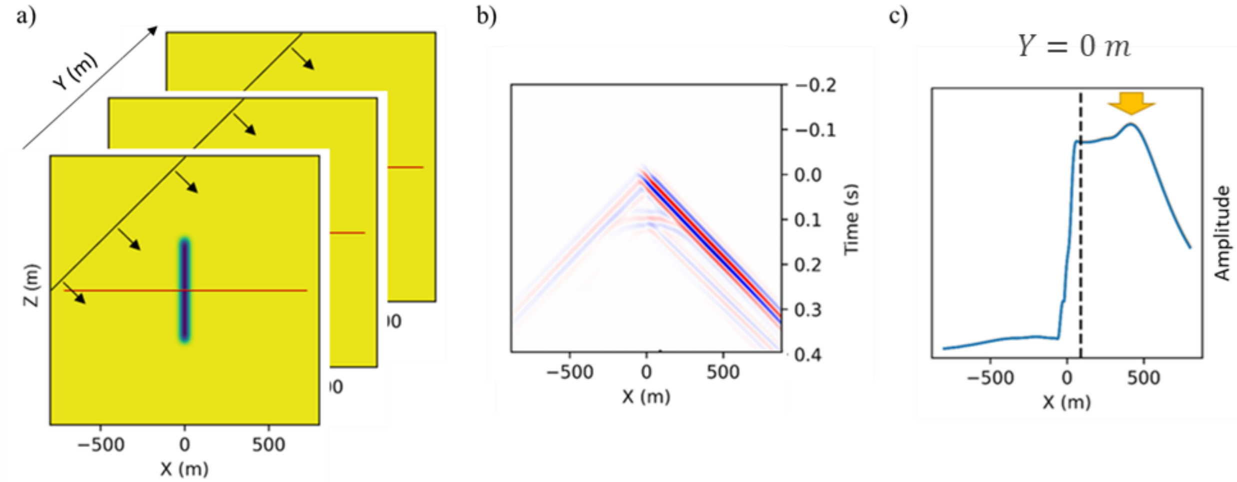

Figure 3.7 (a) '2D velocity model in 3D', (b) corresponding seismogram in terms of the magnitude of PS-wave particle velocity, and (c) maximum amplitude ($Y = 0$ m) extracted from seismogram. The yellow arrow in (c) indicates the end of transmitted PS-wave shadow, which can be used to determine the half-height of the SRV.

Next, we tested four different models to gain additional insights into estimating SRV properties using scattered PS-waves. The velocity anomaly associated with SRV is placed in the middle of the domain with the assumed injector located at (0 m, −700 m, 0 m) coordinates. Figure 3.8 represents $X - Y$ or map view, $Z - Y$ or gun-barrel view, and $Z - X$ or side view slices over the domain center. The receiver lines are distributed in $Z = 0$ m plane of the model along X direction. Different receiver lines allow us to extract seismic wavefields for monitor wells with various offsets. Figure 3.9 shows the resulting amplitude slices for three receiver line locations ($Y = -300$ m, $Y = 0$ m, and $Y = 300$ m) for the models shown in Figure 3.8.

The first model with half-infinite SRV is shown in Figure 3.8a. We use this model to understand whether SRV from an adjacent well should intersect the instrumented well for PS_T waves to be detected. Figure 3.9a shows the decrease in amplitude values of scattered waves as we are moving to the edge of the SRV and away from the velocity anomaly. We find that the amplitude slice away from the SRV edge ($Y = 300$ m) still shows a visible

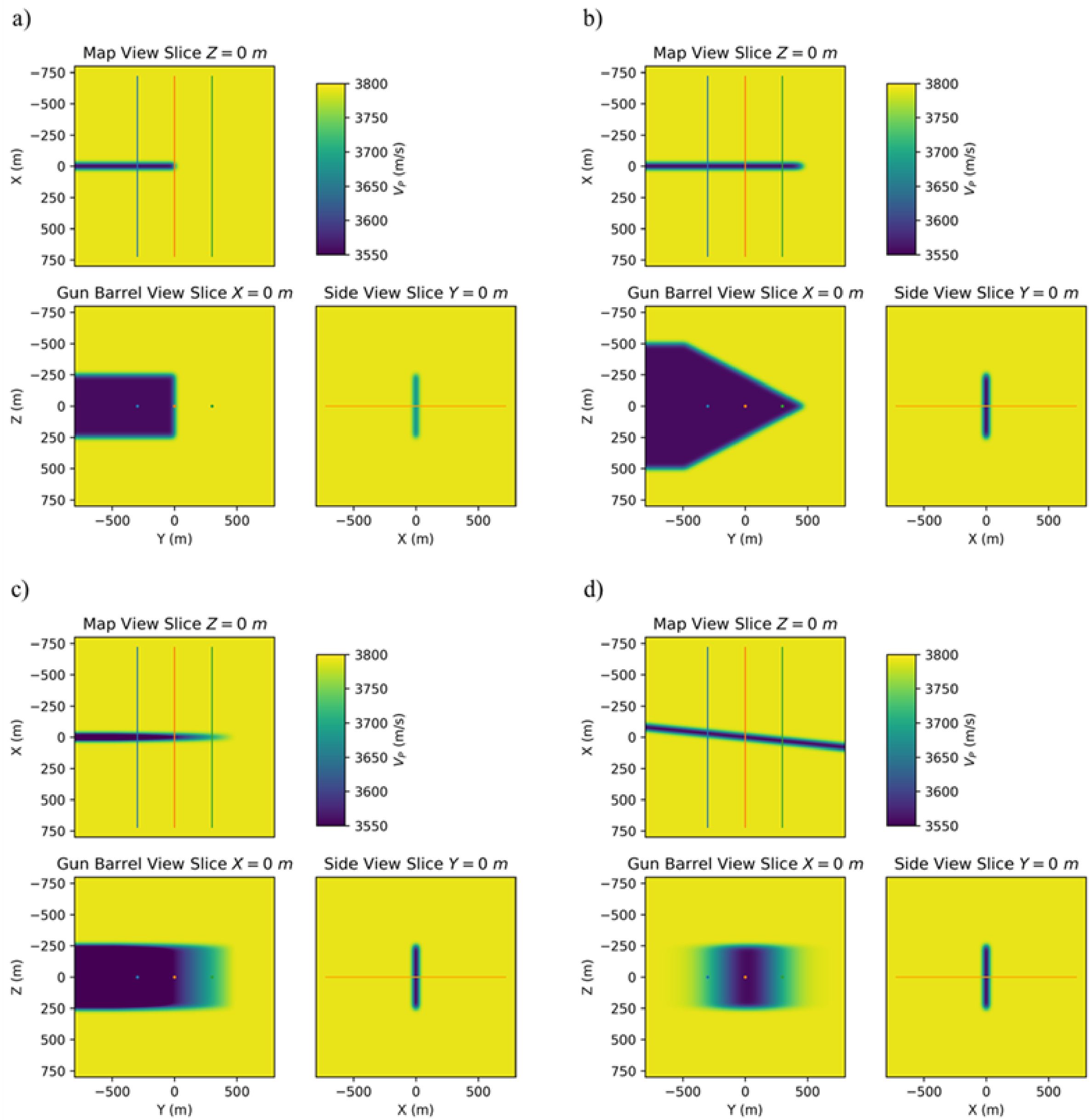

Figure 3.8 P-wave velocity model slices for (a) half-infinite SRV, (b) SRV with the half-height change, (c) SRV with a change in velocity contrast, (d) SRV with non-normal fracture propagation. The lines on X-Y and Z-X slices, as well as the dots on Z-Y slices represent virtual fiber receiver lines, so the modeling allows to obtain seismic wavefields for various geometries of instrumented fiber well relative to SRV locations.

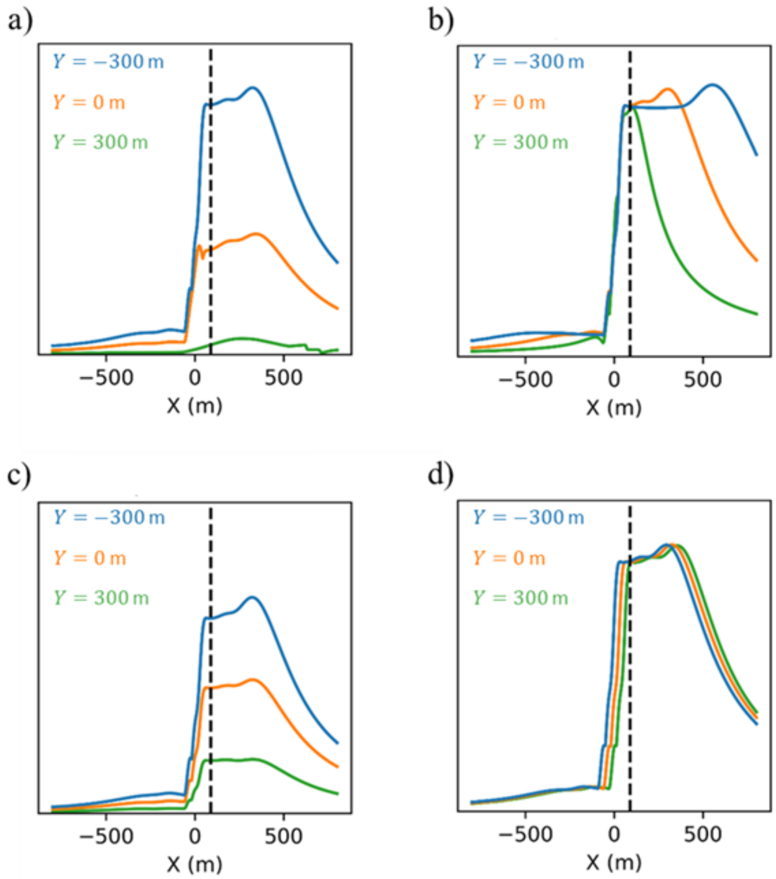

Figure 3.9 Amplitude slices for models shown in Figure 3.8. The slices are shown for fiber wells located on $Y = -300$ m, $Y = 0$ m, and $Y = 300$ m.

response. This means that the scattered waves can be detected even if the SRV does not cross the fiber well. Two mechanisms can explain this response: first, the seismic waves can be affected by the velocity structures within the Fresnel volume. The PS-wave converted by the SRV can be detected with DAS fiber if the SRV is within the seismic Fresnel volume, which could be hundreds of meters away from the ray path depending on the wavelength [79]. In this case, one can use the proposed calculation algorithm for half-height estimation (equation 3.1). Second, part of the energy could be diffracted from the edges of SRV. There is an opportunity to calculate the geometry of SRV from the calculation of the diffracted wave moveout [20]; however, diffracted waves could be too weak to be observed in field data.

The second model of SRV with half-height changing with offset is shown in Figure 3.8b. We see how the peak related to the PS-wave shadow (Figure 3.9b) moves with the SRV half-height change above the receivers. The largest height corresponds to fiber location $Y = -300$ m and the smallest to $Y = 300$ m. In the 3D case and our geometry, half-height calculation corresponds to the average half-height within the Fresnel volume. This modeling result demonstrates that the fracture height above an offset monitor well can be correctly estimated using our proposed method.

The next model, shown in Figure 3.8c, represents the case of a velocity contrast change within the SRV. Amplitude slices for this case are presented in Figure 3.9c. In this case, the change in half-height, does not influence on the location of the peak (around $X = 350$ m). The only difference is in the amplitude values for various fiber well locations. The amplitudes decrease proportionally to the decrease of the velocity contrast, and again, we need to consider the averaging effect within the Fresnel volume.

The last model (Figure 3.8d) represents SRV with non-normal fracture propagation relatively to the injection well. In this case (Figure 3.9d), we see that the entire amplitude slice shifts with the fracture azimuth, which can be used to calculate the fracture propagation direction.

The 3D modeling confirms previous findings of 2D modeling studies and highlights the value of inter-stage DAS VSP data for monitoring not only the completion process of the fiber well but also adjacent wells in its vicinity.

3.6 Discussion

Using the results of 3D modeling, we can further interpret the field data quantitatively to understand the observed similarities and differences in scattered wave properties generated by SRVs from the fiber well (9Bf) and the adjacent well (11A). We have not noticed a significant difference in the size of PS_T shadow zones between these two wells, which is associated with similar fracture heights above the fiber well. This implies that the shapes of 11A SRVs are rectangular at least in the distances of about 100 meters, which is the summation of well spacing and the radii of Fresnel volumes.

For both wells, we see high asymmetry in amplitudes between the reflected and transmitted waves, which according to our modeling, could be interpreted as a SRV with a width of more than 50 m [20]. The reflected PS wave is visible only at several stages. Further stage-by-stage analysis and comparison with validation datasets is necessary to evaluate if SRVs corresponding to these stages have smaller widths.

We observe converted waves with smaller amplitude for well 11A stimulation, which may indicate two possibilities: (1) the velocity contrast decreases away from the initiation point with the SRV intersecting the monitoring well, which may be related to the fracture width decreasing with distance, or (2) the SRV from an adjacent well does not intersect the monitoring well, and the observed scattered waves are caused by the Fresnel zone effect, as the first radius of the Fresnel zone can reach more than 200 m in our case [80]. The answer to this question is important, as it could significantly impact the interpretation of SRV geometry. The two competing interpretations can be distinguished with additional datasets, for example, additional source locations to illuminate the LVZ anomaly from various angles, and/or low-frequency cross-well strain measurements (LFDAS) to confirm fracture hits at the monitor well [32].

Despite changes in the amplitude values, we have not observed changes in amplitude decay rate. This means that the reservoir properties, such as permeability, could be quite similar around wells 9Bf and 11A. Besides, we found a mismatch between the observed trend in well 11A for scattered events distribution (Figure 3.5) and the locations derived from stage location information assuming normal fracture propagation. It means that the fractures which grew from the well 11A are not normal to the well, and the azimuth of the fractures can be estimated.

Future analysis of this data should include stage-level quantification of SRVs, which is possible as the scattered waves vanished quickly. Moreover, integrating this data with other types of DAS data, such as interstage DAS VSP time-shift data [19], low-frequency cross-well strain data [32], microseismic data [72, 81], perforation data [73, 74], will allow for a more comprehensive description of the SRV from DAS scattering measurements.

3.7 Conclusion

Inter-stage DAS VSP surveys provide valuable insight into zipper-fracturing treatment. High-quality data from engineered fiber-optic cable allow for amplitude analysis of the observed PS-waves scattered from the SRV. Amplitude distributions of these waves allow for stage-by-stage hydraulic fracturing effectiveness characterization. A single well with fiber allows monitoring not only the treatment at the fiber well, but also adjacent wells via analysis of PS scattered events to estimate SRV properties, including SRV height, width, and the fracture closure time. Moreover, for adjacent wells the length and azimuth of SRV can be constrained.

The results of 3D modeling gave insights into the 3D nature of seismic wave propagation and interaction of the seismic wavefield with SRV. 3D modeling confirms the feasibility of the proposed method to estimate the SRV properties of well with fiber and adjacent wells and supports the quantitative interpretation of SRV properties.

3.8 Acknowledgments

We thank Reservoir Characterization Project (RCP) members and contributors for making this research possible. We thank Apache Corporation for providing the unique dataset and allowing us to publish the work. We thank Mike Yates, Peter Aaron, Alan Gunnell, and James Simmons for the fruitful discussions.

3.9 Data and materials availability

Data associated with this research are confidential and cannot be released.

CHAPTER 4

EXPERIMENTAL INVESTIGATION OF DISTRIBUTED ACOUSTIC FIBER-OPTIC SENSING IN PRODUCTION LOGGING: THERMAL SLUG TRACKING AND MULTIPHASE FLOW CHARACTERIZATION

A paper submitted to *SPE Production & Operations*.

Aleksei Titov[1,2], Yilin Fan[3], Ge Jin[2], Ali Tura[2], Kagan Kutun[3], and Jennifer Miskimins[3]

4.1 Abstract

This study experimentally investigates the impact of gas bubbles on the thermal and acoustic energy prorogation within the wellbore, at various water and gas flow rates using distributed acoustic sensing (DAS), This is the first study to experimentally investigate the thermal and acoustic propagation at both single- and two-phase flow conditions using DAS. It is believed that the physical interpretation from this study will significantly improve the production logging algorithms especially at multiphase flow conditions, benefit the detection of gas leakage in the vertical section of a wellbore, as well as pipe line flow monitoring. Distributed fiber-optic sensing (DFOS) based production logging has drawn much attention in recent years. Comparing to conventional production logging tools, fiber-optic cables can endure much harsher borehole environments and can be deployed at a lower cost. This work presents an experimental study of using DAS to track the thermal slugging in single-phase (liquid) and two-phase (gas and liquid) flow within a vertical wellbore to estimate flow velocity and characterize multiphase flow behavior.

A vertical flow loop is constructed for this research, which consists of a 7 m long transparent PVC test section with a 1-inch pipe inner diameter. A single-mode optic fiber with thin plastic coating is wrapped evenly around the PVC pipe, with a fiber-to-pipe

[1]Primary researcher and author
[2]Department of Geophysics, Colorado School of Mines, Golden, CO
[3]Department of Petroleum Engineering, Colorado School of Mines, Golden, CO

length ratio of 10.7. Tap water and compressed air are used as the testing fluids. The water and air are injected at the bottom of the test section, similar to field conditions where oil and gas mixture flows into the wellbore from the bottom. The water is directly supplied from the building water system without using an additional pump to minimize the unrelated acoustic noise. Air is supplied from an air tank charged by the building compressor with a maximum pressure of 80 psi. A peristaltic pump is used to inject a small amount of hot water ($< 2\%$ of the minimum water volume from the inlet) to generate thermal slugs at the bottom of the test section.

For the case of single-phase water flow, the velocity of the thermal slugging signal is similar to the actual water velocity, as expected. For multiphase flow, the thermal signal looks almost identical with that for single-phase, although the bubble velocity is much higher than the water velocity. This observation indicates that gas, with low thermal capacity and in its bubble form, cannot carry enough heat to perturb the thermal slugs in the water severely. However, a detailed analysis of the thermal slugging velocity indicates a small increase with an increase of gas flow rate. We interpret that the thermal slugging velocity is associated with the actual water velocity. The existence of the gas bubble decreases the effective water holdup (cross-sectional area occupied by the water phase) in the pipe. We find that, with a constant water volumetric rate, smaller holdup leads to higher in-situ water velocity, thus higher thermal slugging velocity.

The decay of the thermal slugging signal is also analyzed. The signal decay is due to the heat exchange between the fluid and the surrounding, as well as between the warmer and cooler fluid within the pipe. We observe a faster signal decay associated with a higher bubble rate, which indicates a faster heat exchange rate with the existence of gas bubbles. Multiple physical processes may cause this correlation. First, as the gas bubbles travel through the water with a higher velocity, they generate local turbulence in the water phase and accelerate the heat exchange within the water. Another possibility is that the gas, although with much smaller thermal capacity, carries heat from the warmer section to the cooler section, therefore accelerating the thermal equilibrium process. The comparison between the single-phase water and two-phase air-water experimental results indicate that the gas bubbles generate acoustic energy as they move through the pipe. Even in the low-frequency DAS data band (< 0.5 Hz), it appears that the higher background noise-level is associated with the rising bubbles. Detailed analysis of the DAS data indicates individual bubbles can be traceable if they are separated more than a gauge length.

4.2 Introduction

More and more oil and gas companies are interested in utilizing distributed fiber-optic sensing (DFOS). This technology provides a reliable, cost-effective solution for many borehole sensing applications since only the optical fiber is deployed downhole, and all data acquisition hardware is located at the surface [3]. DFOS is widely used both for engineering (production and completion monitoring) and geophysical (vertical seismic profiling, microseismic) applications in the oil and gas industry. Due to the limited understanding of the recorded data, many DFOS data processing flows are still based on qualitative approaches. In this paper, we conduct experiments to help the development of more quantitative methods that can expand the applications of DFOS data.

DFOS technology is split into three main types. In distributed acoustic sensing (DAS), strain changes along the fiber are recorded. In distributed temperature sensing (DTS), the temperature along the fiber is recorded. In distributed strain sensing (DSS), the absolute strain value is recorded [3]. The critical piece of technology behind DFOS is an interrogator unit (IU) located on the surface and consisting of a stable laser and a very sensitive photodetector. The interrogator sends a laser pulse down the optical fiber, which scatters off inhomogeneities in the fiber. The interrogator then records backscattered light, which can be used to measure strain for DAS and DSS or temperature for DTS. By using the time delay of backscattered light, measurements of strain or temperature are distributed along the full length of the cable with a sampling interval as small as 1 m.

DFOS has many advantages for borehole applications compared to conventional tools (geophone, pressure gauges, temperature gauges, etc.). In most cases, the fiber cable is permanently cemented behind the casing. Once installed, fiber can monitor the entire length of the wellbore with an excellent spatial resolution for the whole life of the well. There is no electrical power in the optical fiber cable and no electronic hardware is deployed downhole which means the cable can withstand harsh borehole conditions and high borehole temperatures.

In this study we focus on using DAS to monitor borehole flow. Production flow profiling is one of the most important potential uses of DAS measurements. Knowing the production allocation along a well with multiple production zones can significantly improve the reservoir model, provide better understanding reservoir performance, and identify better producing formation and completion designs. DAS technology provides a unique opportunity as it is sensitive to a wide range of frequencies from 1 mHz to 100 kHz. This is the reason that, for production applications, DAS can be used not only to measure acoustic signals generated by the flow but also to capture subtle temperature changes due to thermal strain induced on the fiber core. According to [6], at extra low-frequencies (< 1 Hz), DAS is sensitive to temperature perturbations as small as 10^{-5} °C/s. In the case of DAS, the phase change of Rayleigh scattered light is measured over a distance called the gauge length, L_g. This provides an estimate of the average strain over the gauge length at each sampling point along the fiber. Depending on the interrogator, the strain rate instead of the strain may be measured [3].

Different components of the DAS signals could be extracted from the data for production logging purposes. One of the first use of DAS for flow monitoring was reported by [82] for a tight gas producers. The production profiles were generated by monitoring acoustic noise generated by produced gas flowing through perforations, and converting the noise intensity captured by DAS in a certain frequency band to flowrates. While this approach can provide some quantitative insight into the production allocation, there are still a lot of factors that can influence results, and the method does not work for oil producing wells. Another approach utilizes detection of sound waves propagated in the fluid within the wellbore. The speed of sound is a function of the fluid density and fluid composition [e.g., 83]. So one could invert the speed of sound for fluid composition. Moreover, analyzing the DAS signal in the frequency-wavenumber domain, one can detect the difference in the speed of sound waves propagating with and against the flow direction using the Doppler effect. The latter approach allows inverting for flow velocity [22, 84]. However, a lot of low-rate producers are very quiet and have low flow velocity, which leads to unreliable Doppler effect results. Flow rate can also be calculated by mapping the turbulent eddies in the flow using DAS data [22, 23]. These eddies are small vortices that can be tracked in the lower frequency band in comparison with sound waves. But this method also requires a high flow velocity in the borehole to generate acoustically detectable eddies.

Another approach is based on the high sensitivity of DAS to thermal changes. A recent study demonstrates the use of low-frequency DAS (LFDAS) signals for tracking the thermal slugging in the wellbore to estimate flow velocity. [24] shows how the combination of calibrated DTS [85] and DAS can be used for production monitoring of low-rate oil producers. DTS is used to measure borehole temperatures during steady states, and DAS is used to measure borehole flow velocities by tracking temperature slugging signals during transient states. Motivated by this research, we further develop the technique for two-phase (liquid and gas) flow, and namely to slug flow.

Slug flow is one of the most common flow patterns encountered in two-phase upward flows in vertical and inclined wellbores and facilities [e.g., 86, 87], and slug flow is characterized as an intermittent flow of large gas bubbles (also known as Taylor bubbles), and liquid slugs with dispersed small gas bubbles. The Taylor bubble has an elongated bullet shape [88]. The alternating impact of almost entirely gas and fully liquid phases can be quite destructive for downhole and surface equipment. Also, the transition to this type of flow can indicate the onset of liquid loading, which can lead to production disruption. In this research, with the help of a vertical flowloop setup, we demonstrate that DAS can be used to detect slug flow and generate a production log using a joint thermal slugging and acoustic tracking approach. The setup and initial results of this experiment are presented in [e.g., 89]. We also developed a novel approach for DAS data processing based on a multispectral analysis of the Taylor bubble oscillation. This approach can lead to a method for reliable production logging and monitoring for wells with two-phase slug flow.

4.3 Experimental setup

The flow loop in this experiment contains of a 7-m long, 1-inch internal diameter transparent PVC pipe, which is placed vertically to represent a vertical wellbore. A single-mode optical fiber with thin plastic coating (Corning SMF-28) is wrapped around the PVC pipe, with a fiber-to-pipe length ratio of 10.7 (about 75 m of fiber wrapped around the 7-m pipe, which lead to ≈ 930 wraps with ≈ 0.74 cm spacing between each wrap). This fiber installation allowed us to receive more data points and use a smaller effective gauge length of about 1 m. Water and air inlets are connected to the bottom of the pipe and flowing upwards by the pressure differential during the experiment. To reduce the unrelated acoustic noise from pump, we use tap water as the water supply. Also, additional insulation was added between strut channels and pipe clamps to minimize pipe vibration. The air is supplied by the building compressor, which can create up to 80 psi pressure difference. Figure 4.1a shows the diagram of the flow loop, and Figure 4.1b shows a picture of the bottom section of the pipe and the wrapped fiber. With this set up, we test two-phase slug flow production logging with an active thermal source. A peristaltic pump is used to add a small amount of hot water into the flow through an inlet at the bottom of the flow loop to generate thermal slugging signals. The hot water supplied from a thermally controlled circulatory bath is about 20°C higher than the tap water temperature, and the injection rate is lower than 0.1 L/min. An OptaSense ODH 3.1 IU was used to record the DAS data.

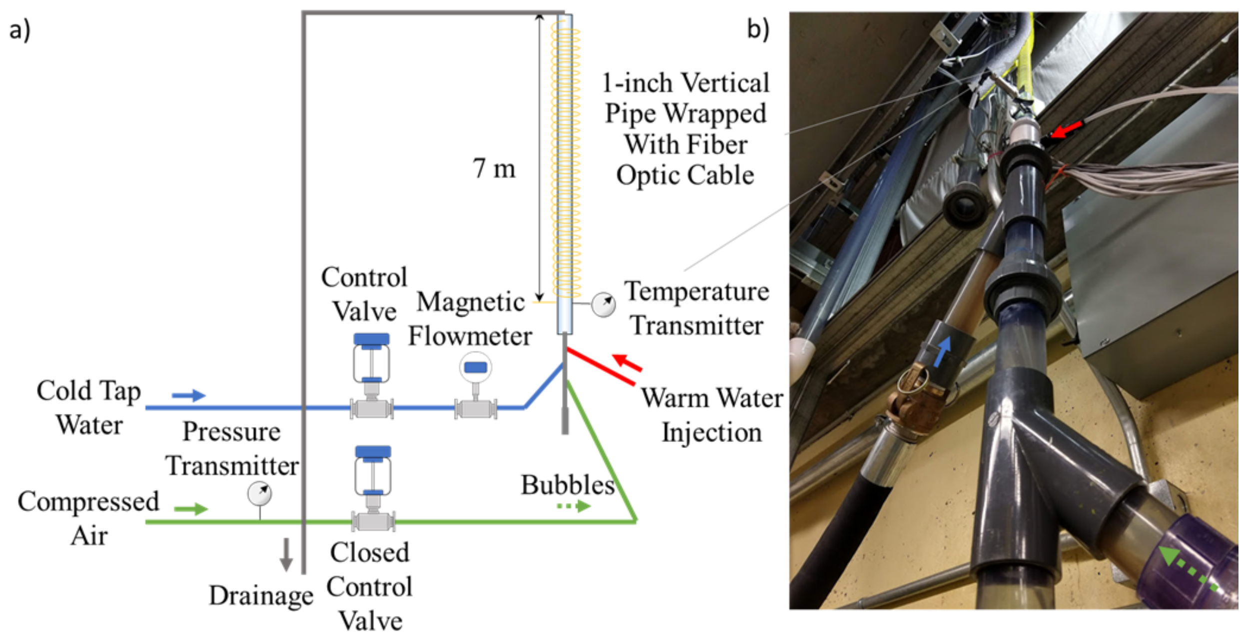

Figure 4.1 (a) Diagram of the vertical flow loop and (b) picture of the pipe bottom section and the wrapped fiber (modified from [88]).

We generate slug flow by injecting a small amount of gas into the flowing water. The main goal is to study how the gas affects the thermal and acoustic energy in the flow. To generate thermal perturbations, hot water was injected for 1 minute, then turned off for 1 minute. The cycle is then repeated several times. The notion is to generate a similar response as observed in field data reported by [24]. Cold tap water flowed with constant superficial velocity, v_{SW}, measured by a magnetic flowmeter. By adding a small amount of gas with different rates into the flow, we generated slug flow (see Figure 4.1). At each gas rate, the hot water injection is repeated for five to six cycles. The air rate is controlled by a small leakage at the control valve with different back-end pressures. Due to the instrument limitation, the volumetric air rate cannot be measured directly with a flowmeter, and a digital camera was used to estimate it.

A flow pattern for slug flow is shown in Figure 4.2a. Two main components of the flow are observed. A Taylor bubble is followed by a liquid slug with dispersed small gas bubbles. A high-definition (HD) video camera was used to acquire a video of slug flow with 60 frames per second. We developed algorithm that reads the video file frame by frame (as shown in Figure 4.2b), calculates averaged RGB color values from a selected area (red box in Figure 4.2b), and outputs an RGB color time series with the zero-mean value presented in Figure 4.2c. We visually compare the extracted time series with the video and set a threshold of –10 amplitude for this study detect a Taylor bubble. When an averaged color value is lower than the threshold, the algorithm detects the transit of the Taylor bubble within the red box. The same approach can be applied at a different location of the red box within the same video frame. Knowing the distance between the boxes, we calculate the Taylor bubble velocity (v_B). Using spectral analysis of the acquired color data time series, we also estimated the average Taylor bubble frequency (f_B), which is correlated with the gas injection rate.

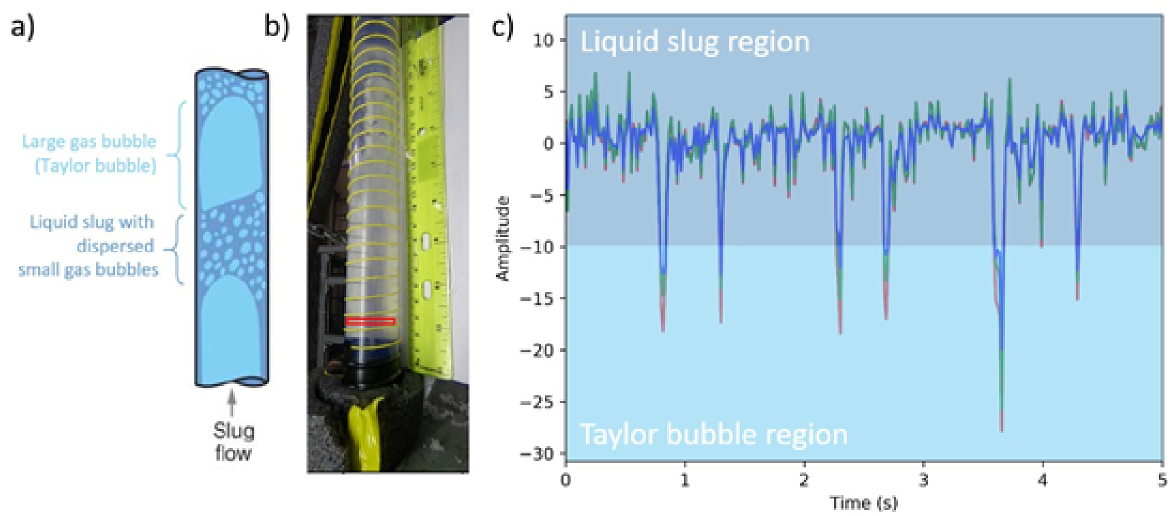

Figure 4.2 (a) Flow pattern for slug flow (modified from [87]). (b) Example of a video frame, the red box indicates the area of extracted averaged RGB color information, which shown in (c) for the 5-second section of the video recording. The dark blue area indicates a liquid slug region, while the bright blue area indicates the Taylor bubble region.

4.4 Thermal slugging for generation DAS-based production log for slug flow

The first experiment was designed to understand how DAS can be used to track artificially generated thermal slugging signals in two-phase slug flow. For this experiment water was flowing with v_{SW} of approximately 0.17 m/s. From video analysis, v_B was estimated to be about 1.6 m/s, and f_B varies from 0 (single-phase water flow) to 1.6 bubbles/s.

4.4.1 DAS data processing workflow

The raw DAS data is recorded in terms of the optical phase for our IU. The initial processing of the DAS data are as follows:

- Convert optical phase data to the phase rate by differentiating along the time axis.
- Remove noise by applying a median filter.
- Apply a low-pass Butterworth filter to pass the signals below 0.5 Hz.

Figure 4.3a shows the processed LFDAS data for single-phase water flow. The horizontal axis is the time of the experiment, while the vertical axis indicates the channel number. Channel 15 corresponds to the bottom and channel 90 to the top of the vertical pipe. One can observe the thermal slugging signal represented by the red (heating) and blue (cooling) bands. To illustrate this signal in more detail, we show the data slice for channel 50. Figure 4.3b shows the raw data itself, and Figure 4.3c shows its smoothed version. The phase rate is linearly proportional to the induced thermal strain changes [3]. Hence the increase and decrease in phase rates correspond to the heating and cooling processes, respectively. In Figure 4.3c one can clearly see the 5 pairs of heating and cooling cycles.

The next processing steps are:

- Cross-correlate each channel with the bottom channel.

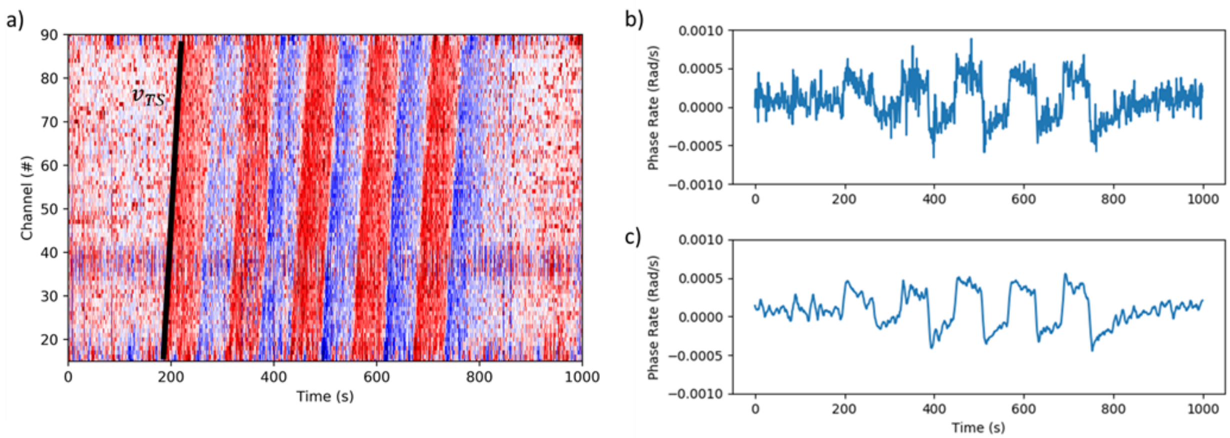

Figure 4.3 (a) LFDAS signal for single-phase water flow, black lines show thermal slugging velocity $v_{TS} \approx 0.19$ m/s. (b) Amplitude slice for channel 50 and its smoothed version (c).

- Analyze the observed time-lag in cross-correlation data for thermal slugging velocity extraction (v_{TS}).
- Analyze the maximum value of cross-correlation for estimation of the DAS amplitude decay rate.

The last step allows us to analyze how quickly thermal energy dissipates. Highlighted with a black line in Figure 4.3a, the velocity of the thermal slugging signal (v_{TS}) is 0.19 m/s, which is approximately 12% higher than the actual water velocity.

The thermal signal with gas injection (Figure 4.4) looks almost identical to single-phase water case (Figure 4.5a), despite the difference in bubble and water velocities ($v_B \gg v_{SW}$). This observation indicates that gas, with low thermal capacity and in its bubble form, cannot carry enough heat to perturb the thermal slugs in the water severely. However, the cross-correlation-based analysis of the thermal slugging velocity indicates a small increase of v_{TS} associated with a higher gas bubble rate (Figure 4.4). We interpret that the v_{TS} is mostly associated with the actual in-situ water velocity, v_w.

Using the effective channel spacing of about 9 cm, we can recalculate the slopes in metric units. The results for the thermal slugging experiment are summarized in

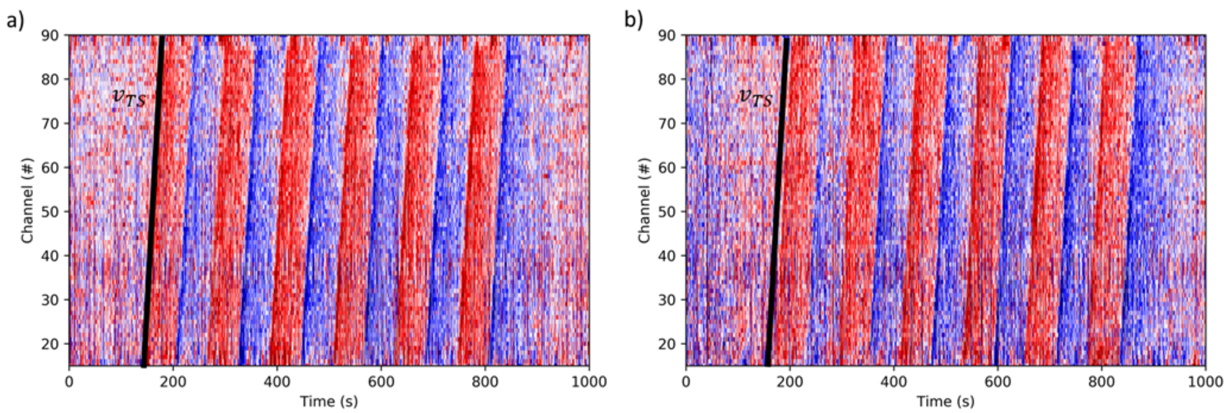

Figure 4.4 LFDAS signal for slug flow: (a) $f_B \approx 1.0$ bubbles/s, $v_{TS} \approx 0.2$ m/s and (b) $f_B \approx 1.6$ bubbles/s, $v_{TS} \approx 0.22$ m/s. Black lines highlight thermal slugging velocities.

Figure 4.5. Figure 4.5a shows how thermal slugging DAS velocity changes with Taylor bubble frequency, and Figure 4.5b shows how the DAS amplitudes decay. The minus sign in front of the logarithm in vertical axis of Figure 4.5b indicates that a higher value of decay means faster thermal dissipation. The Taylor bubble frequency is inversely correlated with the average liquid holdup (H_L); as the existence of the gas bubbles decreases the effective water holdup (volumetric fraction of pipe cross-sectional area occupied by water) in the pipe. With a constant water volumetric flow rate, a smaller liquid holdup leads to a higher actual water velocity, therefore a higher thermal slug velocity. We also observe a faster signal decay associated with a higher Taylor bubble frequency, which indicates a faster heat exchange rate with the existence of gas bubbles. Multiple physical processes may cause this correlation. As the gas bubbles travel through the water with a higher frequency, they generate local turbulence in the water phase and accelerate the heat exchange within the water.

The comparison between the water only example (Figure 4.3a) and two-phase example (Figure 4.4) indicates that gas bubbles generate acoustic energy as they move through the pipe. Even in the low-frequency band (< 0.5 Hz), the apparent higher background noise-level is associated with the rising bubbles. Detailed analysis of the DAS data

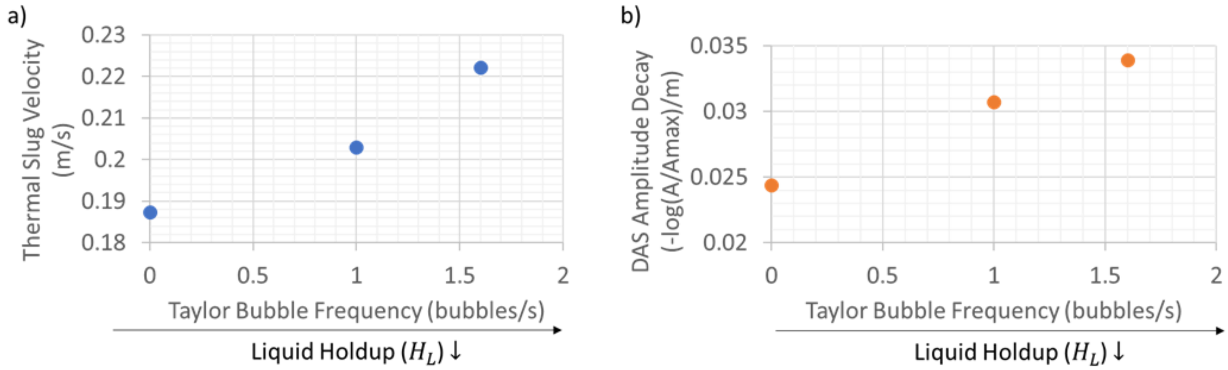

Figure 4.5 LFDAS signal analysis. (a) DAS flow velocity and (b) DAS amplitude decay as a function of the Taylor bubble frequency.

indicates individual bubbles can be traceable, which is detailed in the next section.

4.4.2 Acoustic signatures of rising Taylor bubbles recorded with DAS

A second experiment was conducted to analyze acoustic signatures associated with rising Taylor bubbles. For this experiment water was flowing with a lower superficial velocity, v_{SW} of about 0.07 m/s, in comparison with the first experiment. From video analysis, v_B was estimated to be about 0.3 m/s. This flow regime allows discrimination of acoustic signals from distinct bubbles.

One-minute raw DAS recording and corresponding LFDAS data in terms of phase-rate are shown in Figure 4.6a and Figure 4.6b, respectively. The signal-to-noise ratio for LFDAS thermal slugging, in this case, is very high and one can easily pick the velocity associated with thermal slugging signal of $v_{TS} \approx 0.075$ m/s, which is slightly higher than v_{SW}. This observation matches observations in the first experiment. Note prominence of the boundary between the blue color (cooling down) and the red color (heating up), which is highlighted with a black line in Figure 4.6b. Another interesting signal is associated with the rising Taylor bubble, and it is especially visible during the cool down period of the experiment as a dark blue band. One of these bands is shown with a white line. The v_B extracted from DAS data is very close to the v_B extracted from video analysis.

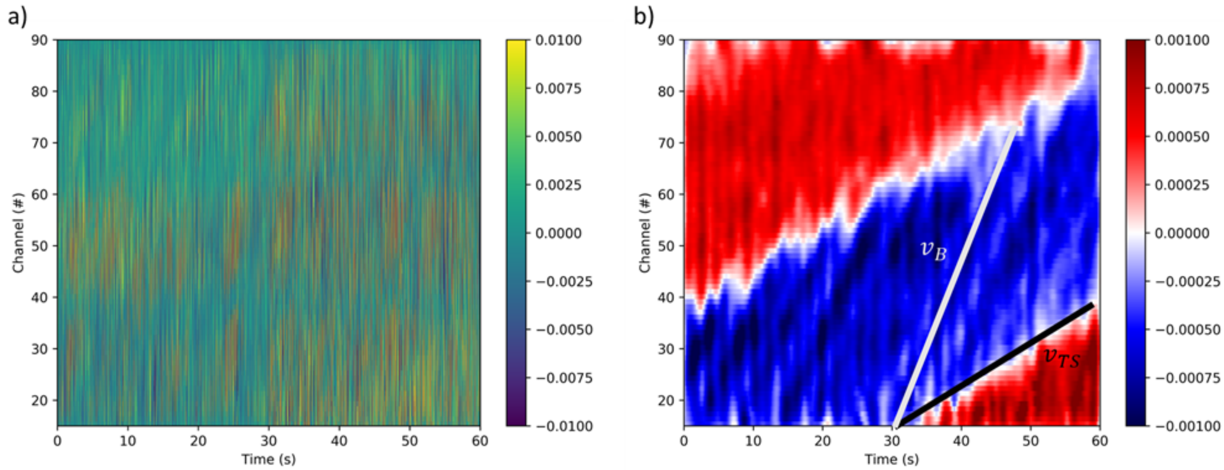

Figure 4.6 Example of DAS data; hot water injection starts at 30 seconds. (a) Raw phase-rate data. (b) Low-passed data (< 0.5 Hz). Thermal slugging trend with velocity $v_{TS} \approx 0.075$ m/s is shown in black and propagation of Taylor bubble signal with velocity v_B is highlighted with white line.

For further analysis of the rising bubble data, we calculate channel-by-channel variations of the Fourier spectrum and corresponding bandpassed DAS signal, which is shown in Figure 4.7. Two frequency bands capture our attention: 20-80 Hz (Figure 4.6a) and 160-200 Hz (Figure 4.6c). For the 20-80 Hz range, we observe multiple diagonal bands in the frequency domain. As acoustic energy propagates from the bottom to top of the pipe, the recorded frequency decreases. In the same frequency range, we have fundamental alternating current frequency about 60 Hz and 30 Hz inter-harmonic distortion, which appear as vertical lines and make the corresponding bandpassed data look noisy; however, one can distinguish signals propagating with v_B. We are associating this frequency range with resonance bubble frequencies, which change as Taylor bubbles are rising and elongated due to pressure decrease. For the 160-200 Hz range, there are no significant variations in the frequency domain, but we observe the signal propagating with the bubble velocity in the bandpassed data. Hence, this frequency band might be associated with liquid slugs.

We apply multispectral analysis to highlight the frequency change as the Taylor bubbles rise up. We divided the 20-80 Hz spectrum into three bands and color-coded them using

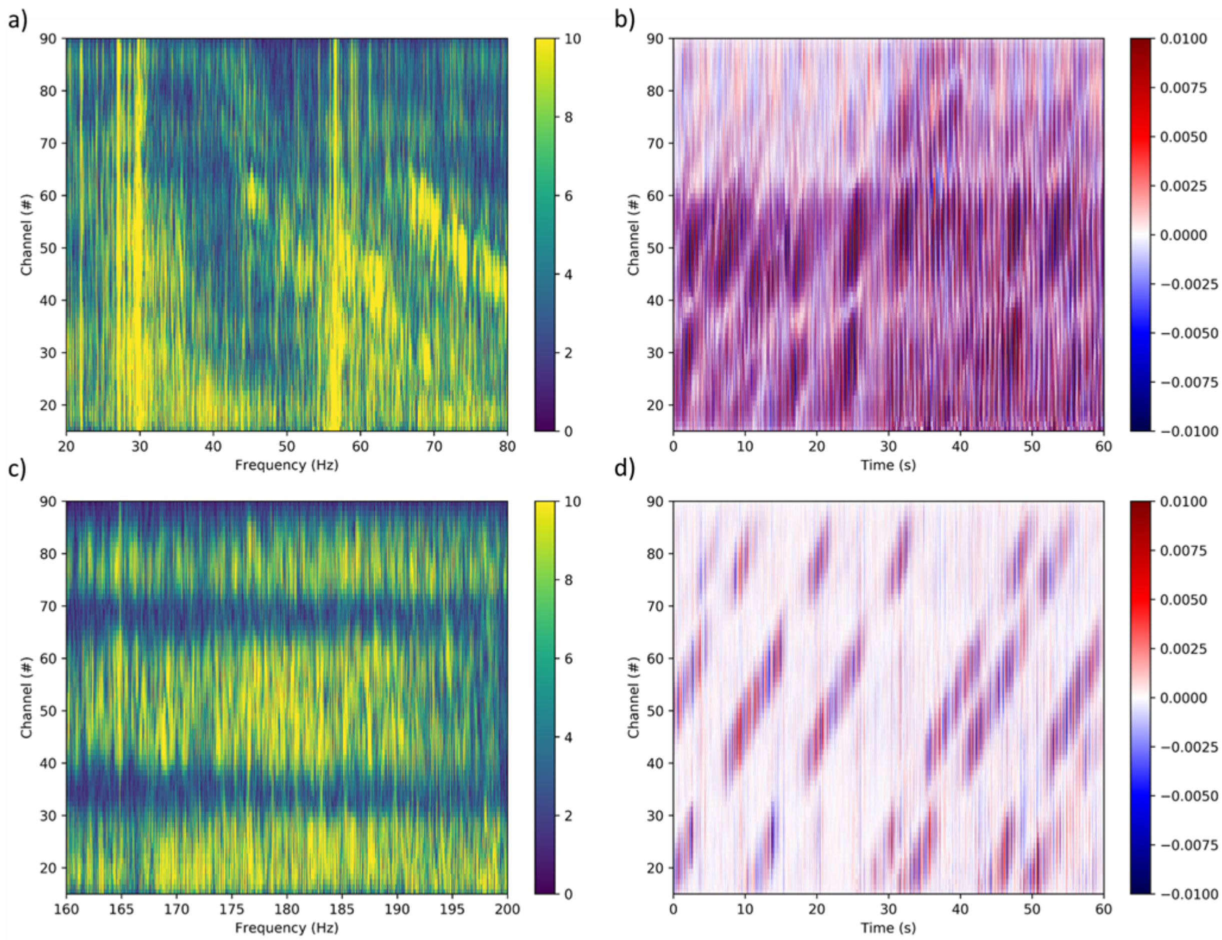

Figure 4.7 Channel-by-channel variations of the Fourier spectrum and the corresponding bandpassed DAS signal. 20–80 Hz (a) and (b), and 160–200 Hz (c) and (d). The first band corresponds to the Taylor bubble and second to liquid slug.

red (20-40 Hz), green (40-60 Hz), and blue (60-80 Hz) colors. After that, for each channel for 1 s of data, we calculated the mean value of spectral amplitude for each frequency band. Finally, we mix all colors to generate an image, shown in Figure 4.8. This is a multispectral time-variable representation of the DAS data. In this representation, blue color correspond to higher frequency and smaller bubbles, green color to a medium frequency and medium-sized bubbles, and red color to a lower frequency and larger bubbles. For various observed bubbles, we can see how the color changes as the bubble propagates along the pipe, which corresponds to a change of the Taylor bubble size. This example shows how DAS can be used to calculate the bubble size.

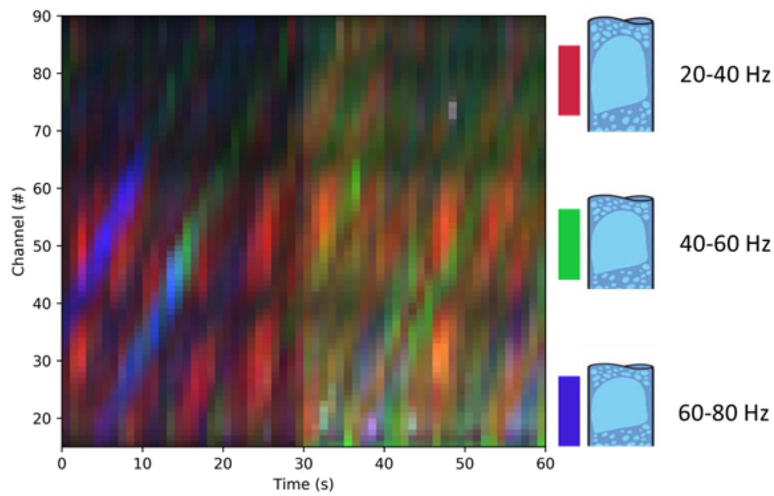

Figure 4.8 Multispectral time-variable representation of the DAS data corresponding to rising Taylor bubbles.

In the literature [e.g., 90], one can find that bubbles have a resonance frequency, also known as Minnaert resonance frequency:

$$\nu_0 = \frac{1}{2\pi R_0}\sqrt{\frac{3\kappa p_0}{\rho}}, \tag{4.1}$$

where R_0 is equilibrium radius of a spherical bubble, κ is a polytropic index ($\kappa = \gamma$ for an adiabatic process, where γ is a ratio of specific heat of a gas at constant pressure to that at constant volume, or $\kappa = 1$ for the isothermal process), p_0 is pressure and ρ is the density of fluid surrounding a bubble. For an air bubble in water under one atmosphere, under assumptions of negligible heat flow and negligible surface tension equation 4.1 reduces to:

$$\nu_0 R_0 \approx 3.3\ m/s. \tag{4.2}$$

Despite the fact that the Taylor bubble is not a spherical freely-oscillating bubble and some of the assumptions may not be correct for our experiment, we can use equation 4.2 to roughly estimate the size of the bubble associated with the frequency of 75 Hz. For the measured pressure of about 1.6 atmospheres at the half-length of the pipe, the $R_0 \approx 4.5$ cm, which is larger than the bubble half-width (1.2 cm) and bubble half-height (2 cm) estimated from the video. This indicates that further studies are required to describe the observed frequency change more precisely.

4.5 Future work

To improve the achieved results and overcome limitations of the current experimental setup, we are constructing a large horizontal flow loop with a real-life borehole. The 230-m flow loop (Figure 4.9) is located in the tunnels of a research mine (Edgar Mine). This flow loop focuses on understanding two-phase flow (water and air) in a horizontal well. A 40-m section (Figure 4.9b section #3) of the flow loop is a 6-in borehole drilled through the rock body in the mine. A 4-in metal casing will be instrumented with two permanently installed fiber cables and cemented into the borehole, to mimic a horizontal wellbore environment. This section of the flow loop is ideal for studying thermal slugging and acoustic wave propagation, as hundreds of feet of rock provides insulation. The other section of the flow loop (Figure 4.9b section #2) contains a 25-m transparent PVC pipe where the pipe inclination is adjustable. This section will be used to study the variation of water holdup due to well inclination and how to use DFOS to measure the holdup. Finally, we plan to develop a wireline DAS-based production tool with active acoustic and thermal source and test it utilizing the Edgar mine flow loop.

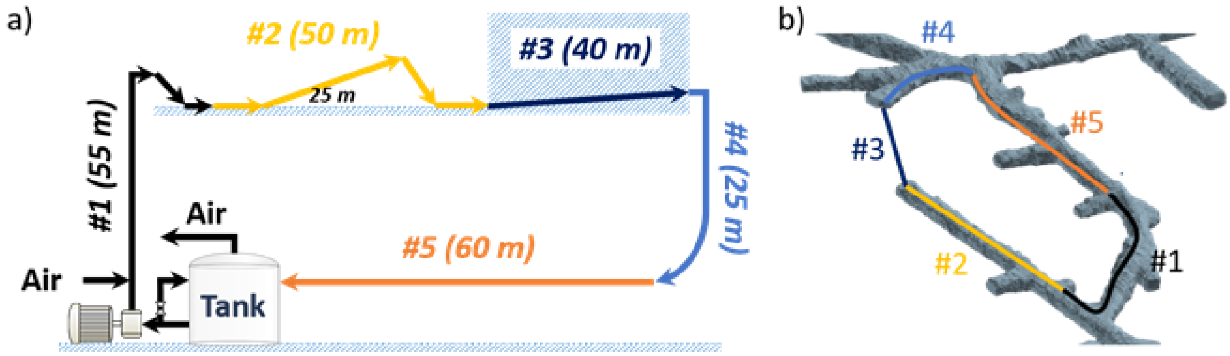

Figure 4.9 Edgar mine flow loop diagram (a) and 3D map (b). The 40-m long section #3 is the in-wellbore part of the flow loop and the 25-m long section #2 is a part with adjustable pipe inclination.

4.6 Conclusions

We have conducted a series of flow loop experiments to understand the fundamental physics of the interaction between the optical fiber and borehole flow. The goal of the experiments was to understand the potential of using fiber-optic sensing technology for production logging purposes in case of two-phase (liquid and gas) slug flow. Results from a vertical flow loop indicate both thermal and acoustic signals measured by DAS are sensitive to the existence of a small amount of gas injection. We found that thermal signatures derived from the DAS data are mostly sensitive to water phase of the flow, while air phase of the flow provides distinctive features in acoustic domain. Investigating both thermal and acoustic characteristics, it is possible to determine velocities of liquid and gas phases separately, as well as estimate liquid holdup. Based on these findings, a novel DAS-based production monitoring algorithm was developed. This approach can also be used for other applications, such as small gas leakage in the vertical section of a wellbore and pipe line flow monitoring.

4.7 Acknowledgments

We thank OptaSense for providing the DAS interrogator and the assistance given by Lisa LaFlame, Dr. Steve Cole, and Dr. Martin Karrenbach. We thank the Reservoir

Characterization Project (RCP), Fracturing, Acidizing, Stimulation Technology (FAST) consortia sponsors, and Dr. Yilin Fan's research group for their support. Also, we thank Dr. Gary Binder and Ana Garcia Ceballos for fruitful discussions.

CHAPTER 5

DISTRIBUTED ACOUSTIC SENSING (DAS) RESPONSE OF RISING TAYLOR BUBBLES IN SLUG FLOW

Ready to submit

Aleksei Titov[1,2], Yilin Fan[3], Kagan Kutun[3], and Ge Jin[2]

5.1 Abstract

Slug flow is one of the most common flow types encountered in surface facilities, pipelines, and wellbores. The intermittent gas phase in a shape of a Taylor bubble followed by the liquid phase can be destructive to equipment. However, commonly used point flow sensors have significant limitations for flow analysis. Distributed acoustic sensing (DAS) can turn optical fibers into an array of distributed strain rate sensors and provide substantial insights into flow characterization. We built a 10-m vertical laboratory flow loop equipped with wrapped fiber optic cable to study the DAS response of rising Taylor bubbles. Low-passed DAS data allows for velocity tracking of Taylor bubbles of different sizes and different water velocities. Moreover, we measured the velocity of the wake region following the Taylor bubble and explore the process of Taylor bubbles merging. The amplitude analysis of DAS data allows for the estimation of Taylor bubble size. We conclude that DAS is a promising tool for understanding Taylor bubble properties in the laboratory environment and monitoring such destructive flow in facilities across different industries for safe and cost-effective operations.

5.2 Introduction

Flow measurements play a crucial role in understanding the fluid dynamics in laboratory experiments as well as safe and economic operations of subsurface and surface

[1]Primary researcher and author
[2]Department of Geophysics, Colorado School of Mines, Golden, CO
[3]Department of Petroleum Engineering, Colorado School of Mines, Golden, CO

facilities. While the single-phase flow metering is well-established, the development of sensors for multiphase flow evaluation is still undergoing and currently the point flow meters have been used in most cases. There is increasing demand for distributed multi-phase-capable measuring solutions, both for laboratory and field environments. The need is even more demanding in in-well flow profiling for hydrocarbon producers. Some works suggest so-called distributed virtual flow metering based on advanced machine-learning algorithms [e.g., 91, 92]. This approach converts arrays of temperature and pressure sensors and point flowmeters to an array of distributed flowmeters. Despite that there is significant progress in this direction, the robustness of algorithms and availability of dense temperature and pressure sensors significantly limit this approach. Another solution utilized acoustic, strain, and temperature features of different flow types recorded by the fiber optic cable using distributed fiber optic sensing (DFOS) methods [93].

One of the most promising DFOS technologies is distributed acoustic sensing (DAS). DAS has developed rapidly in recent years. DAS utilizes telecommunication or special engineered fibers and turns them into a dense array of strain rate meters [3]. Due to the broad band of frequencies that DAS can capture, this technology has a broad spectrum of applications. For example, in the oil and gas industry, DAS applications include recording of seismic waves [e.g., 70], detection of fracture propagation [e.g., 32], and flow profiling [e.g., 23]. In addition, DAS is sensitive to subtle temperature variations in sub millihertz range and can be used as distributed temperature gradient sensors (DTGS). If the sensing fiber is installed on top of a structure which can change its dimensions due to pressure change inside (e.g., pipes [e.g., 94], mandrels [9]), DAS can act as a distributed pressure gradient sensor (DPGS).

From DAS data, one can measure the speed of sound in the fluid and estimate the flow rate using the Doppler Effect [e.g., 22, 84]. Flow rate can also be calculated by mapping the slugs and turbulent eddies using DAS data [e.g., 23, 84]. In addition, recent studies demonstrated using low frequency DAS signals to track thermal slugging in the wellbore to estimate flow velocity for low-rate oil producers [24] and in laboratory setup [95]. The implementation of these potential capabilities will highly benefit chemical, oil and gas, carbon sequestration, and geothermal industries. In this paper, we use a laboratory testing facility to advance DAS-based two-phase (liquid and gas) slug flow characterization.

Slug flow is a flow consisting of intermittent liquid and gas phases [25, 96]. Gas forms the Taylor bubble, which is followed by a liquid slug. Immediately after the Taylor bubble, there is a region with smaller dispersed bubbles (dispersed bubble train or wake [97]). Slug flow is one of the most common flow types encountered in wells and pipelines, which can be destructive for surface and downhole equipment. Moreover, for oil and gas industry applications, the transition to slug flow type can indicate the onset of liquid loading, leading to a shorter well life span. Hence, it is crucial to characterize such flow type, and DAS is one of the most promising solutions. We designed and built a vertical flow loop facility to study slug flow with DAS. Our work shows that DAS can determine the velocities of both the Taylor bubble and dispersed bubble train as well as the size of the Taylor bubble.

5.3 Data acquisition and processing

5.3.1 Flow loop testing facility

To study slug flow in a controlled environment, we built a vertical flow loop test facility. Figure 5.1 shows the design of a vertical flow loop located inside the lab space with high ceilings. Telecommunication single-mode fiber is wrapped around a 2-inch vertical schedule 40 PVC pipe and covers the entire length of the pipe. In addition, two pressure transmitters and a video camera were installed. Figure 5.1b shows the Taylor bubble generating apparatus, which produce air bubbles of controlled sizes. It consists of several valves connected by pipe sections. The air volume trapped between valves is released when the valves are consequently opened from top to bottom. The trapped volume between each pair of valves used in the experiment is indicated in Figure 5.1b. Figure 5.1c presents the modification of the bubble apparatus for studying interactions between two bubbles of the same size.

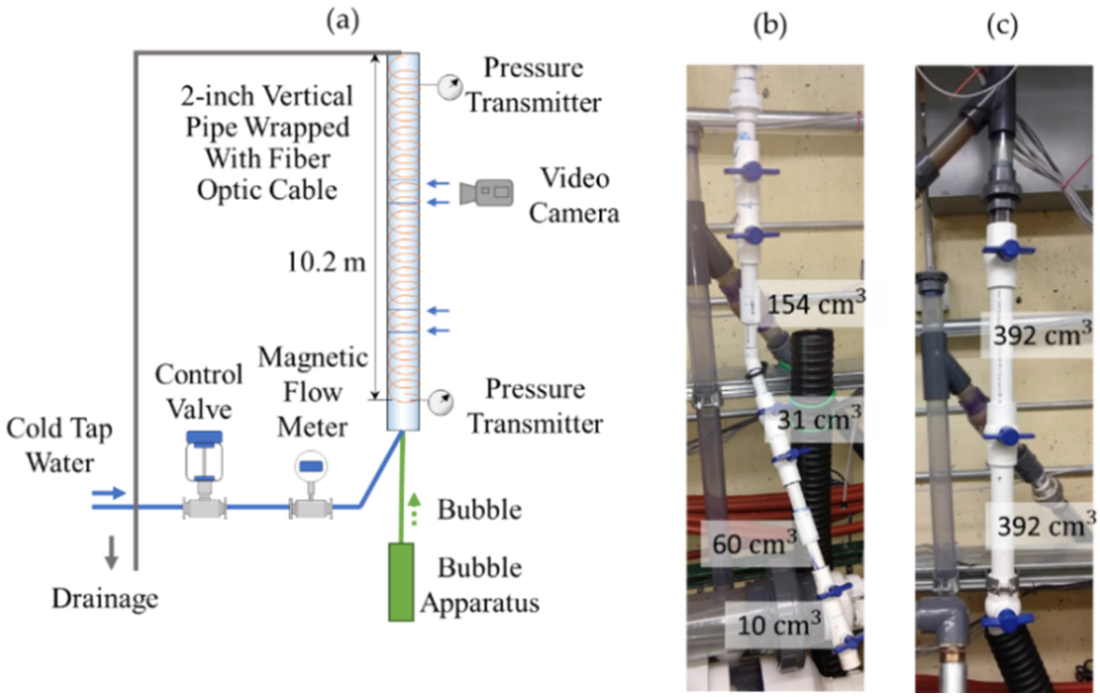

Figure 5.1 (a) Design of vertical flow loop facility with attached bubble apparatus. The main elements are indicated. Blue horizontal arrows point to the pipe joints. (b) Bubble apparatus to generate bubbles of different sizes. (c) Bubble apparatus to study the interaction of two bubbles of the same size.

The generated bubbles captured by the video camera are shown in Figure 5.2 for all studied bubble sizes. The bubble contours of are highlighted with gray lines for clarity. This figure also gives illustration of the fiber installation. The tight buffered fiber used for DAS acquisition is single-mode Corning SMF-28 with a yellow jacket of $D_f = 900$ μm in diameter. The orange fiber is a multi-mode fiber and was not used in this work. The distance (d_w) between wraps is 1 cm. The outer diameter of the PVC pipe (D_O) is 6.032 cm. Hence, to calculate the fiber-to-pipe length ratio (FPR) we use:

$$FPR = \sqrt{\left(\frac{\pi(D_O + D_f)}{d_w}\right)^2 + 1}, \tag{5.1}$$

where FPR here equals 19.26.

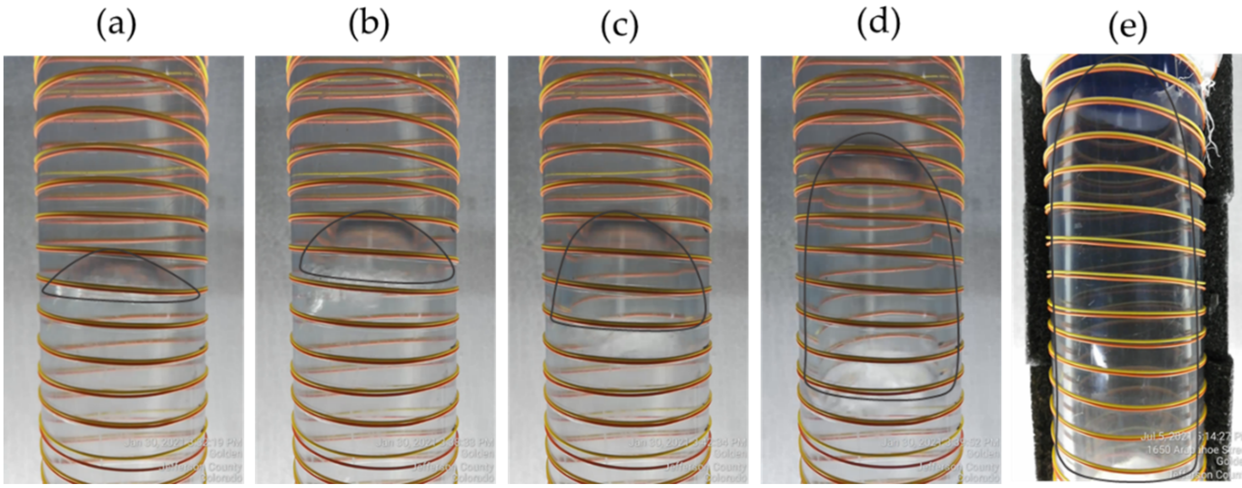

Figure 5.2 Example of generated Taylor bubble of different volume: (a) 10 cm^3, (b) 31 cm^3, (c) 60 cm^3, (d) 154 cm^3, and (e) 392 cm^3. The yellow tight buffered fiber was used for the DAS acquisition. The distance between neighboring wraps is 1 cm.

5.3.2 DAS data processing

We used the Treble interrogator unit (IU) from Terra 15 [98–100] to acquire the DAS data for this work. The IU natively measures and output the rate of fiber length change ($\dot{x}$ [m/s]) and allows for post-acquisition gauge length (GL, L_g [m]) assignment when data are converted to strain rate ($\dot{\varepsilon}$ [(m/m)/s]) by taking spatial derivative along fiber axis (x):

$$\dot{\varepsilon}(x) = \frac{\dot{x}\left(x + \frac{L_g}{2}\right) - \dot{x}\left(x - \frac{L_g}{2}\right)}{L_g}. \tag{5.2}$$

The optimal results are achieved when GL is equal to pulse width (PW), which in our case was equal to 2.45 m. We followed this rule of thumb, and as our first step of data processing, we converted the raw data to strain rate, using equation 5.2. The data were acquired with sampling rate $f_s = 4$ kHz and spatial sampling $dx = 0.82$ m along the fiber cable. Due to wrapped fiber geometry, the effective channel spacing and GL are obtained by division of fiber to pipe ratio and leads to the effective channel spacing $\widetilde{x} = 4.3$ cm and effective gauge length $\widetilde{L_g} = 12.9$ cm along the pipe length. Figure 5.3a shows an example of raw DAS data (waterfall plot) in terms of strain rate for a typical experiment. For all waterfall plots in this paper, the colormap limits are from $-0.2\ \mu\varepsilon/\mathrm{s}$ to $0.2\ \mu\varepsilon/\mathrm{s}$. In this experiment, the water velocity $v_w = 0$ m/s (stagnant water column) and the bubble volume $V_B = 392\ \mathrm{cm}^3$. The horizontal axis is the relative time from the beginning of recording for a particular experiment, and the horizontal axis is the distance along the vertical pipe. The initial data have a significant amplitude shift into negative values, which can be related to a slight environmental temperature decrease. So, the baseline signal was estimated by averaging 2.5 s (highlighted in Figure 3a with a blue box) of the recorded data for each DAS channel (Figure 5.3b). This baseline vector was subtracted from the initial data matrix. Using frequency-wavenumber analysis, we estimated that the frequency of the signal associated with rising Taylor bubble is below 1 Hz, which is consistent with previously published computational fluid dynamics (CFD) models of rising Taylor bubble [101]. Hence, as a next step we apply 1 Hz low-pass filter and downsample the data by a factor of ten, which led to time sampling of $\widetilde{dt} = 10/f_s = 0.0025$ s.

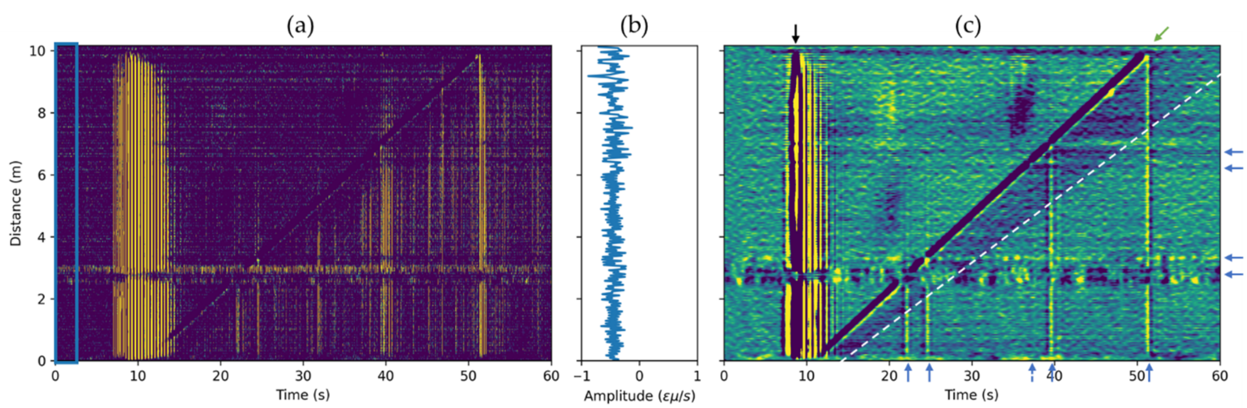

Figure 5.3 Example of DAS data processing for the Taylor bubble of 392 cm^3 rising in the stagnant water column. (a) DAS data after conversion to the strain-rate domain. The baseline signal is estimated by averaging data for the first 2.5 s, as highlighted by the blue box. (b) The estimated baseline signal. (c) DAS data after baseline subtraction, application of 1 Hz low-pass filter, and x10 downsampling. The green inclined arrow indicates the signal associated with constant rise velocity of Taylor bubble. The black vertical arrow indicates the noise (tube-waves) associated with ball-valve opening, while the blue vertical arrows point to tube-waves generated by the Taylor bubble passing through the pipe joints (indicated by horizontal blue arrows).

The result of the DAS data processing is shown in Figure 5.3c. The signal associated with the rising Taylor bubble is clearly seen in the processed data as a diagonal dark blue line (starting around 11 s and ending around 52 s). This signal corresponds to the negative strain rate, which corresponds to a very small pipe diameter decrease as the bubble passes through. In this experiment, each DAS trace in our wrapped installation is a proxy to the pressure gradient sensor. From this figure, one can conclude that the velocity of the Taylor bubble does not change as it rises in the water column. Moreover, one can estimate velocity by fitting the linear moveout ($v_B \approx 10$ m/41 s ≈ 0.24 m/s). The automatic workflow for velocity estimation will be presented in the next section. Another useful signal for flow analysis is associated with the observed blue shadow following the Taylor bubble. The boundary between this zone and background noise is highlighted with a white dashed line. After analyzing the video record, we conclude that this blueish region is associated with a train of dispersed bubbles following the Taylor bubble. The smaller slope of the dashed white line compared to the Taylor bubble signal is associated with slower dispersed bubble train velocity (≈ 0.20 m/s). Other signals include waves, which propagate with relatively high velocity (≈ 1500 m/s), which results in vertical bands in the figure. The most intensive tube wave (indicated by black vertical arrow) is associated with ball valve opening and vibration of the entire flow loop due to this mechanical impact. Other smaller tube waves are generated when the bubble hits the pipe joint or reaches the top of the water column. The joints are indicated by horizontal blue arrows, while the corresponding tube waves by vertical blue arrows. Note that the tube waves associated with the joints mainly propagate downward, as their energy quickly dissipates in the upward direction where the Taylor bubble (gas) occupies most of the pipe cross-section.

5.3.3 Workflow for estimating Taylor bubble velocity and size

To further analyze the DAS signals associated with the Taylor bubble, we propose the following workflow. First, we remove the signal related to the valve opening by assigning zeros to all DAS data from 0 s to 12 s in Figure 5.3b. Next, we shift every subsequent channel by the number of time samples (N_t) to flatten signal associated with the Taylor bubble rise (Figure 5.4a). We can calculate velocity using the following equation:

$$v = \frac{\widetilde{dx}\widetilde{fs}}{N_t}. \tag{5.3}$$

As the Taylor bubble generates a negative strain rate response, we minimize the minimum amplitude of the averaged signal (Figure 5.4b) by changing v, as shown in Figure 5.4c. The minimum amplitude value in this plot corresponds to Taylor bubble velocity in a stagnant water column, which also known as a drift velocity $v_d = 0.249$ m/s.

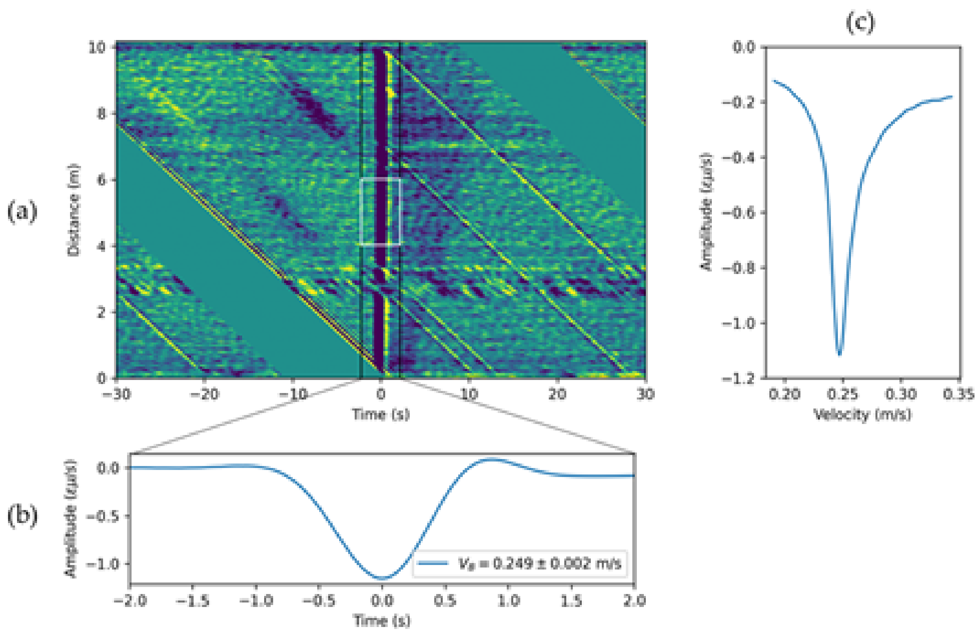

Figure 5.4 Example of Taylor bubble velocity and size estimation. (a) Flattened data with a velocity of 0.249 m/s. Time axis origin corresponds to the Taylor bubble signal. (b) DAS response averaged along distance axis zoomed into the region of ±2 s around Taylor bubble. (c) Minimum of the averaged DAS response for flattening procedure with different velocities.

The magnitude of the averaged signal (Figure 5.4b) is related to Taylor bubble size, as the larger Taylor bubble creates a larger absolute value strain rate anomaly. However, the uncertainty is high and the estimation depends on the flattening of the bubble signal. That is why for amplitude analysis, we used RMS amplitude in the ±2 s window around the

Taylor bubble signal in time and averaged from 4 m to 6 m in space. The window for RMS amplitude extraction is shown as a white rectangle in Figure 5.4a. For this example, the RMS amplitude is equal to 0.514 $\mu\varepsilon$/s.

5.4 Results

5.4.1 Influence of Taylor bubble size on DAS response

We conducted a series of experiments to analyze how the size of generated bubbles influences DAS response. Figure 5.5 illustrates the flattened responses for bubbles of different sizes, shown in Figure 5.2. The flattening velocity of 0.249 m/s was the same for all experiments. The results indicate that Taylor bubble velocity does not depend on bubble size, that is in agreement with [25]. [26] formulates that Taylor bubble velocity in a stagnant water column can be calculated using:

$$v_d = 0.35\sqrt{gD_I}, \tag{5.4}$$

where g is the acceleration due to gravity and D_I is the internal tube diameter. In our case $g = 9.798$ m/s^2 and $D_I = 5.199$ cm, which results in a velocity of $v_d = 0.250$ m/s, which is very close to the measured velocity. It is evident that the signal amplitude becomes more prominent as the volume of bubbles increase. Also, the time duration of the negative strain-rate disturbance broadens, as it takes more time to cross a particular DAS channel for the larger bubble.

To analyze the response more quantitatively, we utilize the proposed approaches in the previous section to extract DAS data products that are related to bubble properties. The products as a function of initial bubble volume are shown in Figure 5.6. Figure 5.6a presents the extracted velocity, which is constant for different volumes. Figure 5.6b shows the DAS distance-averaged response. We observe the increase in absolute amplitude perturbation and time duration of the negative region. However, as we mentioned before, a more robust way to extract associated amplitude changes is to use RMS amplitude, shown in Figure 5.6c. The linear fit could be a good first step for the estimation of a Taylor

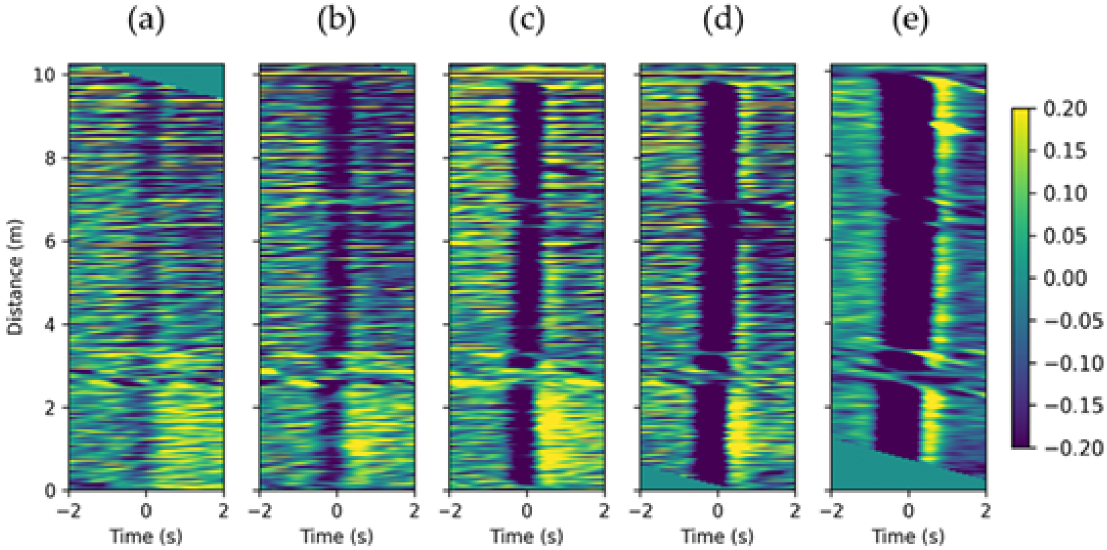

Figure 5.5 Flatten DAS response for bubbles of different size: (a) 10 cm^3, (b) 31 cm^3, (c) 60 cm^3, (d) 154 cm^3, and (e) 392 cm^3. The velocity of flattening is 0.249 m/s for every experiment.

bubble volume. However, DAS amplitude response is rather complicated, as it involves the pipe response to pressure drop associated with the bubble, mechanical coupling between the fiber and the pipe, and the effect of gauge length averaging.

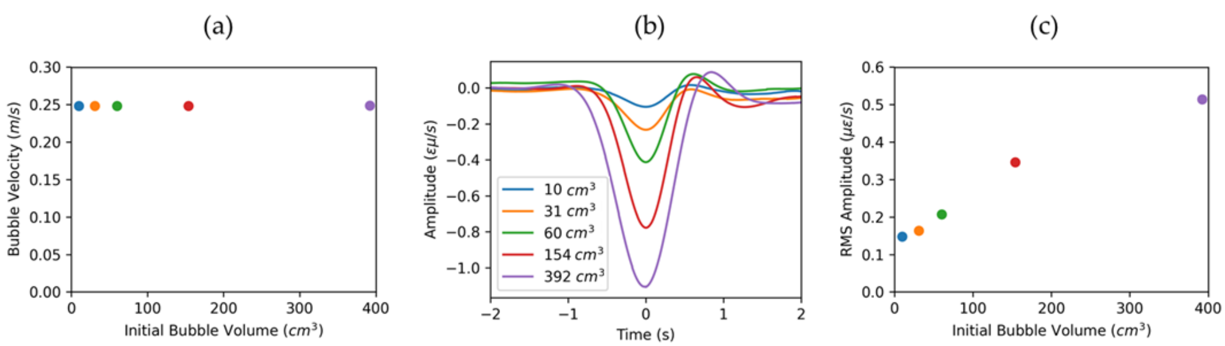

Figure 5.6 Extracted DAS data products as a function of initial bubble volume. (a) Taylor bubble velocity is constant for all experiments $v_d = 0.249$ m/s. (b) DAS response averaged along distance axis. (c) RMS amplitude in ± 2 s window around the Taylor bubble signal in time and averaged from 4 m to 6 m in space.

5.4.2 Multiple Taylor bubbles DAS response in a stagnant water column

Due to the distributive nature of DAS measurements, the suggested workflow can be highly beneficial to study Taylor bubble interactions, which is challenging with point sensors. The problem of Taylor bubble interactions is important in the fluid dynamics community, and a significant amount of research can be found in the literature [e.g., 102]. Using the bubble apparatus (Figure 5.1c), we generated two bubbles, separated by a defined length, to observe bubble merging process in DAS data (Figure 5.7).

In the presented experiment, bubbles were separated by 5 s (indicated by vertical black arrows), which initially equals about 1.25 m separation. From the previous experiment with the single bubble (Figure 5.3c), we estimated the velocity of the dispersed bubble train (wake), which is indicated as a white dashed line in Figure 5.7a. For the first 2 m of DAS data, both Taylor bubbles travel with the same velocity v_d; however, as soon as the second bubble intersects the wake region of the first bubble, the second Taylor bubble accelerates to a constant velocity of about 0.333 m/s (white dotted line). We validate that the observed signals are associated with the first (Figure 5.7b) and second (Figure 5.7c) bubbles using the recorded video from the camera. Note that the first bubble has a bullet shape. However, the second bubble shape is disturbed by the turbulent wake region of the first bubble. After the bubble merging occurred, the new Taylor bubble travels at the same velocity as the first Taylor bubble. Also, we noticed that there are more relatively large bubbles observed in the train of the second bubble (Figure 5.7d). The signals from them are also visible in DAS data. These bubbles are rising with the same velocity as the second Taylor bubble.

5.4.3 Influence of water velocity on DAS response

In the previous sections we analyzed the DAS response of rising Taylor bubbles in a stagnant water column. We conducted the following experiment to verify whether the suggested workflow can be applied to non-zero water superficial velocity. In the

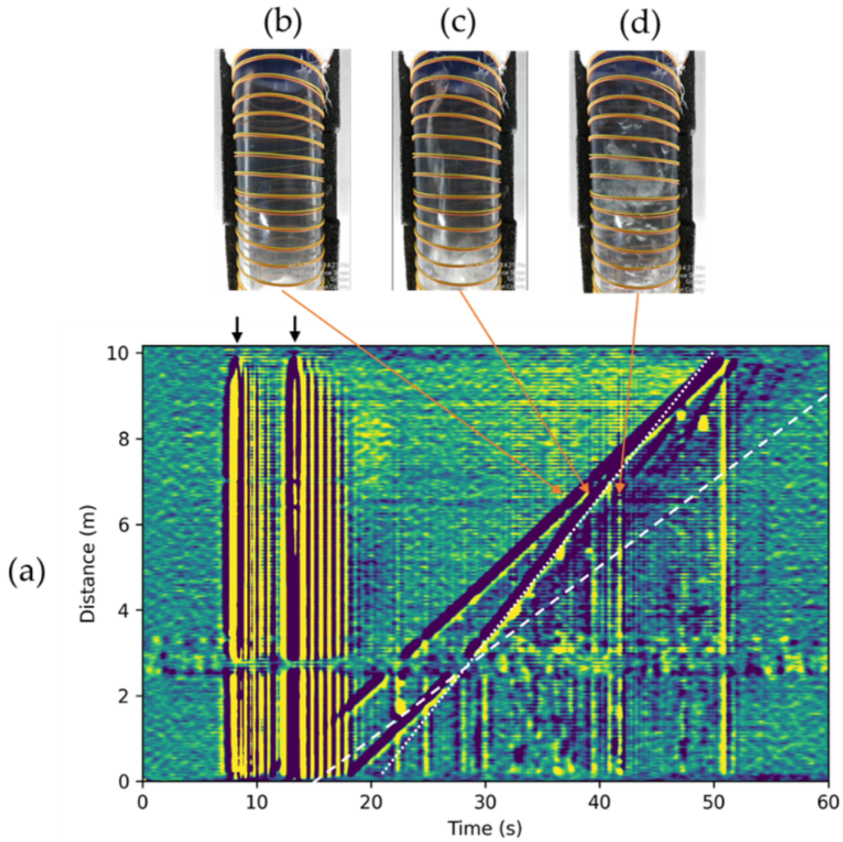

Figure 5.7 (a) DAS response for two 392 cm^3 bubbles simultaneously present in a stagnant water column. Black arrows indicate the signals associated with the opening of the ball valves. The first bubble signal is similar to the signal presented in Figure 5.3c. The white dashed line indicates the wake region of the first Taylor bubble. The second Taylor bubble changes its velocity as soon as it arrives at the wake region of the first bubble. The velocity of the second bubble is indicated by the white dotted line. (b) Photo of the first Taylor bubble. (c) Photo of the second Taylor bubble while in the wake region of the first bubble. (c) Photo of a bubble in the train of the second Taylor bubble.

experiment, the water was flowing with v_{SW}=0.096 m/s as measured by the flow meter. v_{SW} is the superficial water velocity, defined by the volumetric water flow rate divided by the cross-sectional area of the pipe. Figure 5.8a illustrates the observed DAS response to one 392 cm^3 Taylor bubble and Figure 5.8b to two 392 cm^3 bubbles present in the water column. Besides additional noise from flowing water, we still observe all features associated with the Taylor bubbles propagation. The Taylor bubble velocity in this case
$v_B = 0.385$ m/s.

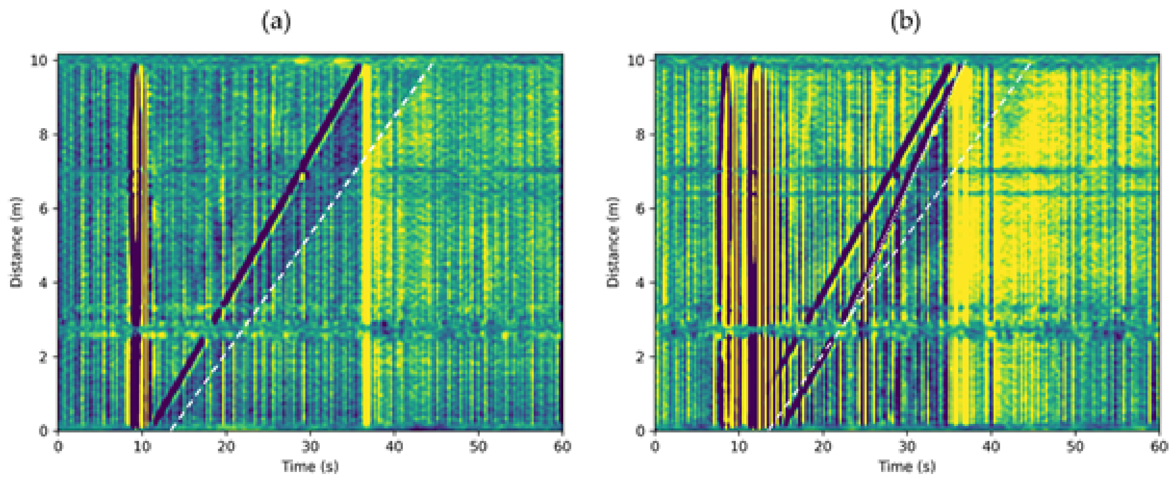

Figure 5.8 DAS response to Taylor bubbles rising in water column moving with $v_{SW} = 0.096$ m/s. (a) One 392 cm^3 bubble. (b) Two 392 cm^3 bubbles. White dashed lines indicate the wake region of the first Taylor bubble. The dotted white line in subplot (b) shows the velocity of the second Taylor bubble in the wake region of the first Taylor bubble.

Note that $v_B > v_M + v_d$, which is consistent with the theoretical estimates [26]:

$$v_B = C_0 v_M + v_d, \tag{5.5}$$

where $1.2 < C_0 < 2$ is the distribution coefficient representing the impact of the velocity and concentration profile [103]. v_M is the mixture velocity, given by

$$v_M = v_{SW} + v_{SA}, \tag{5.6}$$

where v_{SA} is the superficial air velocity, defined as the volumetric air flow rate divided by the pipe cross-sectional area. In this experiment, v_{SA} is negligible in equation 5.6.

5.5 Discussion and conclusions

In this manuscript we demonstrate that DAS is a promising tool for flow analysis, such as slug flow in the laboratory environment. After applying a low-pass filter, each DAS trace in the strain rate domain can be treated as a pressure gradient sensor, or a temperature gradient sensor, as we showed in Chapter 4 and our previous works [24, 95]. Extracting velocities associated with pressure (or temperature) change is robust and can be done with high accuracy in a wide range of values. We demonstrate that it is possible to capture the velocities associated with a Taylor bubble and its wake region. Moreover, due to the distributed nature of measurements, velocity tracking can be possible along all length of the laboratory setup, allowing us to observe and analyze the process of two Taylor bubbles merging.

DAS amplitude analysis can provide much more information regarding the measured processes. However, the DAS amplitudes should be treated carefully, as in non-invasive configuration (when the fiber is mounted on top of the piping) they are related to pressure (or temperature) variations inside a pipe as a function of DAS acquisition parameters (effective GL), pipe material, and extent of anomaly. If the anomaly is smaller than effective GL, the GL smoothing effect should be considered. Furthermore, inhomogeneities in fiber installation and the pipe itself can influence the strain transfer from pressure anomaly inside the pipe to the strain of optical fiber core, which is the actual measurand. Hence the calibration of DAS data with the point sensors is necessary to achieve quantitative results. Nevertheless, we were able to extract DAS amplitudes and relate them to the Taylor bubble size.

The suggested fiber installation can be easily upscaled for flow monitoring in surface facilities. Furthermore, similar physical principles of pressure anomaly detection are possible with straight fiber installation, allowing the proposed methodology to linear structures where the wrapped installation is not optimal, e.g., flow monitoring along pipelines or in wellbores.

5.6 Acknowledgments

We thank Ali Tura and Jennifer Miskimins at Colorado School of Mines for insightful discussions, Kristina Cameron at Colorado School of Mines for help with fiber installation, Michael Roelens and Nader Issa at Terra 15 for DAS acquisition support. We thank sponsors of RCP and FAST consortia and Dr. Yilin Fan's research group for their financial support.

5.7 Data availability statement

Data associated with this research are confidential and cannot be released.

CHAPTER 6

CONCLUSIONS

The main benefit of permanent fiber installation along a well is the vast number of different datasets that can be acquired using the same cable along the entire life span of a well. This thesis advances DAS technology for two applications related to different periods of well life: completion (Chapter 2 and Chapter 3) and production (Chapter 4 and Chapter 5).

First, we derived traveltime equations and performed numerical modeling to interpret the observed scattered events in the interstage DAS VSP data. The results indicate that the events in the data are converted PS-waves. The low-velosity zone model, representing a diffused SRV around hydraulic fractures, provides the best match to the data. Because converted PS-waves can be observed only in a limited range of DAS channels, one can estimate the half-height of the SRV by mapping the DAS channel range through a simple ray-tracing model. In the field data, we observed three major scattered events by stacking along the transmitted PS-wave moveout to increase the S/N and understand the distribution of the scattered events. The estimated half-height of SRV from these three events ranges from 245 to 310 m. Each event lasts more than one day. The stacked amplitude decay time is related to the fracture closure rate and indicates the permeability of the stimulated reservoir.

Furthermore, interstage DAS VSP surveys provide valuable insight into zipper-fracturing treatment. High-quality data from engineered fiber-optic cable allow for amplitude analysis of the observed PS-waves scattered on SRV. Amplitude distributions of these waves can be used for hydraulic fracturing effectiveness characterization. A single fiber well enables monitoring of the treatment of fiber well and adjacent wells via PS scattered events analysis to estimate SRV properties. This analysis includes SRV height, length, and width, as well as the fracture closure time. The results of 3D modeling gave insight into the 3D nature of seismic wave propagation and the interaction of the seismic wavefield with SRV. 3D modeling confirms the feasibility of the proposed method to estimate the SRV properties of fiber and adjacent wells. It also supports the quantitative interpretation of SRV properties.

To advance flow monitoring with DAS, we conducted a series of flow loop experiments to understand the fundamental physics of the interaction between the optical fiber and borehole flow. The goal of the experiments was to understand the potential of using fiber-optic sensing technology for production logging and surface facilities monitoring in the case of a two-phase (liquid and gas) slug flow. Results from a vertical flow loop show both thermal and acoustic signals measured by DAS are sensitive to the existence of a small amount of air. Furthermore, we found that thermal signatures derived from the DAS data are primarily sensitive to the water phase of the flow. In contrast, the gas phase of the flow provides distinctive features in the acoustic frequency range. Investigating both thermal and acoustic characteristics, it is possible to determine the velocities of liquid and gas phases separately, as well as to estimate liquid holdup. Based on these findings, a novel DAS-based flow monitoring algorithm was developed. This approach can also be used for other applications, such as monitoring a small gas leakage in the vertical section of a wellbore and pipeline flow profiling.

Finally, we demonstrate that DAS is a promising tool for flow analysis, such as slug flow in the laboratory environment. After applying a low-pass filter, each DAS trace in the strain rate domain can be treated as a pressure- or a temperature-gradient sensor. Extraction of velocities associated with pressure (or temperature) change is robust and can be done with high accuracy in a wide range of values. We demonstrate that capturing the velocities associated with a Taylor bubble and its wake region is possible. Moreover, due to the distributed nature of measurements, velocity tracking is possible along the entire length of the laboratory setup, allowing us to observe and analyze the merging process of two Taylor bubbles. DAS amplitude analysis can provide much more information regarding the measured processes, and we were able to extract DAS amplitudes and relate them to the Taylor bubble size.

The thesis showcases that DAS is a unique technology for monitoring processes during the entire life span of a well. The main focus was the applications of DAS in the unconventional oil and gas industry. However, the developed interstage DAS VSP analysis of PS-waves can be directly applied to monitoring well completion in enhanced geothermal systems. Moreover, it also can be expanded to the faults mapping. Similarly, the findings regarding DAS response to thermal, acoustic, and pressure attributes of a slug flow can be used in pipeline monitoring workflows and in chemical and processing industries.

REFERENCES

[1] Julia Correa, Anton Egorov, Konstantin Tertyshnikov, Andrej Bona, Roman Pevzner, Tim Dean, Barry Freifeld, and Steve Marshall. Analysis of signal to noise and directivity characteristics of DAS VSP at near and far offsets – a CO2CRC Otway Project data example. *The Leading Edge*, 36(12):994a1–994a7, 2017.

[2] P Richter, T Parker, C Woerpel, Y Wu, R Rufino, and M Farhadiroushan. Hydraulic fracture monitoring and optimization in unconventional completions using a high-resolution engineered fibre-optic distributed acoustic sensor. *First Break*, 37(4): 63–68, 2019.

[3] Arthur H Hartog. *An introduction to distributed optical fibre sensors*. CRC Press, 2017.

[4] Matthew W Becker and Thomas I Coleman. Distributed acoustic sensing of strain at Earth tide frequencies. *Sensors*, 19(9):1975, 2019.

[5] Patrick Paitz, Pascal Edme, Dominik Gräff, Fabian Walter, Joseph Doetsch, Athena Chalari, Cédric Schmelzbach, and Andreas Fichtner. Empirical investigations of the instrument response for distributed acoustic sensing (DAS) across 17 octaves. *Bulletin of the Seismological Society of America*, 111(1):1–10, 2021.

[6] Ge Jin, Herbert W Swan, Baishali Roy, and Kyle R Krueger. Measuring downhole temperature by combining DAS/DTS data, September 14 2017. US Patent App. 15/453,216.

[7] Thomas M Daley, Barry M Freifeld, Jonathan Ajo-Franklin, Shan Dou, Roman Pevzner, Valeriya Shulakova, Sudhendu Kashikar, Douglas E Miller, Julia Goetz, and Jan Henninges. Field testing of fiber-optic distributed acoustic sensing (DAS) for subsurface seismic monitoring. *The Leading Edge*, 32(6):699–706, 2013.

[8] C Didraga. DAS VSP recorded simultaneously in cemented and tubing installed fiber optic cables. In *77th EAGE Conference and Exhibition 2015*, number 1, pages 1–5. European Association of Geoscientists & Engineers, 2015.

[9] Jan Henninges, Evgeniia Martuganova, Manfred Stiller, Ben Norden, and Charlotte M Krawczyk. Wireline distributed acoustic sensing allows 4.2 km deep vertical seismic profiling of the rotliegend 150° c geothermal reservoir in the North German Basin. *Solid Earth*, 12(2):521–537, 2021.

[10] A Green. Game-changing technology for low cost, high quality borehole seismic data acquisition. In *82nd EAGE Annual Conference & Exhibition*, number 1, pages 1–5. European Association of Geoscientists & Engineers, 2021.

[11] Herbert F Wang, Xiangfang Zeng, Douglas E Miller, Dante Fratta, Kurt L Feigl, Clifford H Thurber, and Robert J Mellors. Ground motion response to an ML 4.3 earthquake using co-located distributed acoustic sensing and seismometer arrays. *Geophysical Journal International*, 213(3):2020–2036, 2018.

[12] Xiang Wu, Mark E Willis, William Palacios, Andreas Ellmauthaler, Oscar Barrios, Simon Shaw, and Dan Quinn. Compressional-and shear-wave studies of distributed acoustic sensing acquired vertical seismic profile data. *The Leading Edge*, 36(12): 987–993, 2017.

[13] Ivan Lim Chen Ning and Paul Sava. Multicomponent distributed acoustic sensing: Concept and theory. *Geophysics*, 83(2):P1–P8, 2018.

[14] Albena Mateeva, Jorge Lopez, Jeff Mestayer, Peter Wills, Barbara Cox, Denis Kiyashchenko, Zhaohui Yang, Wilfred Berlang, Rocky Detomo, and Samantha Grandi. Distributed acoustic sensing for reservoir monitoring with VSP. *The Leading Edge*, 32(10):1278–1283, 2013.

[15] Ge Zhang, Jan Kommedal, and Jay Nahm. VSP field trials of distributed acoustic sensing in Trinidad and Gulf of Mexico. In *85th Annual international Meeting*, pages 5539–5543. SEG, Expanded Abstracts, 2015.

[16] Sudhish K Bakku, Michael Fehler, Peter Wills, Jeff Mestayer, Albena Mateeva, and Jorge Lopez. Vertical seismic profiling using distributed acoustic sensing in a hydrofrac treatment well. In *SEG Technical Program Expanded Abstracts 2014*, pages 5024–5028. Society of Exploration Geophysicists, 2014.

[17] Grant Byerley, Dave Monk, Peter Aaron, and Mike Yates. Time-lapse seismic monitoring of individual hydraulic frac stages using a downhole DAS array. *The Leading Edge*, 37(11):802–810, 2018.

[18] Robert Hull, Robert Meek, Hector Bello, Kevin Woller, and Jed Wagner. Monitoring horizontal well hydraulic stimulations and geomechanical deformation processes in the unconventional shales of the Midland Basin using fiber-based time-lapse VSPs, microseismic, and strain data. *The Leading Edge*, 38(2):130–137, 2019.

[19] Gary Binder, Aleksei Titov, Youfang Liu, James Simmons, Ali Tura, Grant Byerley, and David Monk. Modeling the seismic response of individual hydraulic fracturing stages observed in a time-lapse distributed acoustic sensing vertical seismic profiling survey. *Geophysics*, 85(4):T225–T235, 2020.

[20] Aleksei Titov, Gary Binder, Youfang Liu, Ge Jin, James Simmons, Ali Tura, David Monk, Grant Byerley, and Mike Yates. Modeling and interpretation of scattered waves in interstage distributed acoustic sensing vertical seismic profiling survey. *Geophysics*, 86(2):D93–D102, 2021.

[21] Kjetil Johannessen, Brian Keith Drakeley, and Mahmoud Farhadiroushan. Distributed acoustic sensing-a new way of listening to your well/reservoir. In *SPE Intelligent Energy International*. Society of Petroleum Engineers, 2012.

[22] D Finfer, TR Parker, V Mahue, M Amir, M Farhadiroushan, and S Shatalin. Non-intrusive multiple zone distributed acoustic sensor flow metering. In *SPE Annual Technical Conference and Exhibition*. Society of Petroleum Engineers, 2015.

[23] Rakesh Paleja, Daria Mustafina, Timothy Park, David Randell, Juun van der Horst, and Roger Crickmore. Velocity tracking for flow monitoring and production profiling using distributed acoustic sensing. In *SPE Annual Technical Conference and Exhibition*. Society of Petroleum Engineers, 2015.

[24] Ge Jin, Kyle Friehauf, Baishali Roy, Jesse J Constantine, Herbert W Swan, Kyle R Krueger, and Kevin T Raterman. Fiber optic sensing-based production logging methods for low-rate oil producers. In *Unconventional Resources Technology Conference, Denver, Colorado, 22-24 July 2019*, pages 1183–1199. Unconventional Resources Technology Conference (URTeC), 2019.

[25] RM Davies and Geoffrey Ingram Taylor. The mechanics of large bubbles rising through extended liquids and through liquids in tubes. *Proceedings of the Royal Society of London. Series A. Mathematical and Physical Sciences*, 200(1062):375–390, 1950.

[26] DJ Nicklin. Two-phase bubble flow. *Chemical engineering science*, 17(9):693–702, 1962.

[27] Stephen A Holditch. The increasing role of unconventional reservoirs in the future of the oil and gas business. *Journal of Petroleum Technology*, 55(11):34–79, 2003.

[28] Steve H Mohr and Geoffrey M Evans. Long term prediction of unconventional oil production. *Energy Policy*, 38(1):265–276, 2010.

[29] Kan Wu and Jon E Olson. Mechanisms of simultaneous hydraulic-fracture propagation from multiple perforation clusters in horizontal wells. *SPE Journal*, 21 (03):1–9, 2016. doi: 10.2118/178925-PA.

[30] Shawn C Maxwell, Jim Rutledge, Robert Jones, and Michael Fehler. Petroleum reservoir characterization using downhole microseismic monitoring. *Geophysics*, 75 (5):75A129–75A137, 2010.

[31] M Kevin Fisher and Norman R Warpinski. Hydraulic-fracture-height growth: real data. *SPE Production & Operations*, 27(01):8–19, 2012.

[32] Ge Jin and Baishali Roy. Hydraulic-fracture geometry characterization using low-frequency DAS signal. *The Leading Edge*, 36(12):975–980, 2017.

[33] Michael J Mayerhofer, Elyezer Lolon, Norman R Warpinski, Craig L Cipolla, Douglas W Walser, and Claude M Rightmire. What is stimulated reservoir volume? *SPE Production & Operations*, 25(01):89–98, 2010.

[34] NR Warpinski, PT Branagan, BP Engler, R Wilmer, and SL Wolhart. Evaluation of a downhole tiltmeter array for monitoring hydraulic fractures. *International Journal of Rock Mechanics and Mining Sciences*, 34(3-4):318–e1, 1997.

[35] Robert R Stewart, Roger M Turpening, and M Nafi Toksoz. Study of a subsurface fracture zone by vertical seismic profiling. *Geophysical Research Letters*, 8(11): 1132–1135, 1981.

[36] HJ Vinegar, PB Wills, DC DeMartini, J Shlyapobersky, WFJ Deeg, RG Adair, JC Woerpel, JE Fix, and GG Sorrells. Active and passive seismic imaging of a hydraulic fracture in diatomite. *Journal of Petroleum Technology*, 44(01):28–90, 1992.

[37] Mark A Meadows and Don F Winterstein. Seismic detection of a hydraulic fracture from shear-wave VSP data at Lost Hills field, California. *Geophysics*, 59(1):11–26, 1994.

[38] Enru Liu, Stuart Crampin, and John A Hudson. Diffraction of seismic waves by cracks with application to hydraulic fracturing. *Geophysics*, 62(1):253–265, 1997.

[39] Jeroen Groenenboom and Dirkjan B van Dam. Monitoring hydraulic fracture growth: laboratory experiments. *Geophysics*, 65(2):603–611, 2000.

[40] Seiji Nakagawa, KT Nihei, and LR Myer. Shear-induced conversion of seismic waves across single fractures. *International Journal of Rock Mechanics and Mining Sciences*, 37(1-2):203–218, 2000.

[41] Mark E Willis, Daniel R Burns, Rongrong Lu, M Nafi Toksöz, and Nancy J House. Fracture quality from integrating time-lapse VSP and microseismic data. *The Leading Edge*, 26(9):1198–1202, 2007.

[42] Vladimir Grechka, Zhao Li, Bo Howell, Hugo Garcia, and Tom Wooltorton. High-resolution microseismic imaging. *The Leading Edge*, 36(10):822–828, 2017.

[43] Gregor Cedilnik, Gareth Lees, Poul Erik Schmidt, Søren Herstrøm, and Tommy Geisler. Pushing the reach of fiber distributed acoustic sensing to 125 km without the use of amplification. *IEEE Sensors Letters*, 3(3):1–4, 2019.

[44] Albena Mateeva, Jorge Lopez, Hans Potters, Jeff Mestayer, Barbara Cox, Denis Kiyashchenko, Peter Wills, Samantha Grandi, Kees Hornman, Boris Kuvshinov, Wilfred Berlang, Zhaohui Yang, and Rocco Detomo. Distributed acoustic sensing for reservoir monitoring with vertical seismic profiling. *Geophysical Prospecting*, 62(4): 679–692, 2014.

[45] P Webster, J Wall, C Perkins, and M Molenaar. Micro-seismic detection using distributed acoustic sensing. In *83rd Annual International Meeting*, pages 2459–2463. SEG, Expanded Abstracts, 2013.

[46] Martin Karrenbach, Steve Cole, Andrew Ridge, Kevin Boone, Dan Kahn, Jamie Rich, Ken Silver, and David Langton. Fiber-optic distributed acoustic sensing of microseismicity, strain and temperature during hydraulic fracturing. *Geophysics*, 84 (1):D11–D23, 2018.

[47] P Webster, B Cox, and M Molenaar. Distributed acoustic sensing for cross-well frac monitoring. In *GeoConvention 2014: FOCUS*. Canadian Society of Petroleum Geologists, 2014.

[48] Robert Meek, Robert Hull, Kevin Woller, Brian Wright, Mike Martin, Hector Bello, and James Bailey. Estimation of hydraulic fracture height and pressure deflation using a pulsed vertical seismic profile and a DAS fiber in the Midland Basin. In *SPE/AAPG/SEG Unconventional Resources Technology Conference*, pages 1174–1182. Unconventional Resources Technology Conference (URTeC), 2019.

[49] Ran Zhou, Mark E Willis, and William Palacios. Detecting hydraulic fracture induced velocity change using rapid time-lapse DAS VSP. In *SEG International Exposition and Annual Meeting*, pages 4859–4863. Society of Exploration Geophysicists, 2019.

[50] A Mateeva, J Lopez, D Chalenski, M Tatanova, P Zwartjes, Z Yang, S Bakku, K De Vos, and H Potters. 4D DAS VSP as a tool for frequent seismic monitoring in deep water. *The Leading Edge*, 36(12):995–1000, 2017.

[51] Jeroen Groenenboom and Joachim Falk. Scattering by hydraulic fractures: finite-difference modeling and laboratory data. *Geophysics*, 65(2):612–622, 2000.

[52] Richard T Coates and Michael Schoenberg. Finite-difference modeling of faults and fractures. *Geophysics*, 60(5):1514–1526, 1995.

[53] Chunling Wu, Jerry M Harris, Kurt T Nihei, and Seiji Nakagawa. Two-dimensional finite-difference seismic modeling of an open fluid-filled fracture: comparison of thin-layer and linear-slip models. *Geophysics*, 70(4):T57–T62, 2005.

[54] Kurt T Nihei, Seiji Nakagawa, and Larry R Myer. Fracture imaging with converted elastic waves. In *38th US Symposium on Rock Mechanics (USRMS)*. American Rock Mechanics Association, 2001.

[55] Kenneth D Mahrer and Frederick J Mauk. Seismic wave motion for a new model of hydraulic fracture with an induced low-velocity zone. *Journal of Geophysical Research: Solid Earth*, 92(B9):9293–9309, 1987.

[56] Gary Mavko, Tapan Mukerji, and Nicola Godfrey. Predicting stress-induced velocity anisotropy in rocks. *Geophysics*, 60(4):1081–1087, 1995.

[57] Kevin T Raterman, Yongshe Liu, and Logan Warren. Analysis of a drained rock volume: an Eagle Ford example. In *SPE/AAPG/SEG Unconventional Resources Technology Conference*, pages 4106–4125. Unconventional Resources Technology Conference (URTeC), 2019.

[58] Randolph R Settgast, Pengcheng Fu, Stuart DC Walsh, Joshua A White, Chandrasekhar Annavarapu, and Frederick J Ryerson. A fully coupled method for massively parallel simulation of hydraulically driven fractures in 3-dimensions. *International Journal for Numerical and Analytical Methods in Geomechanics*, 41(5): 627–653, 2017.

[59] Thomas E Blum, Kasper Van Wijk, Roel Snieder, and Mark E Willis. Laser excitation of a fracture source for elastic waves. *Physical review letters*, 107(27): 275501, 2011.

[60] Sergey Fomel, Paul Sava, Ioan Vlad, Yang Liu, and Vladimir Bashkardin. Madagascar: open-source software project for multidimensional data analysis and reproducible computational experiments. *Journal of Open Research Software*, 1(1):e8, 2013.

[61] Bjorn Olofsson and Alex Martinez. Validation of DAS data integrity against standard geophones – DAS field test at aquistore site. *The Leading Edge*, 36(12):981–986, 2017.

[62] Ariel Lellouch, Steve Horne, Mark A Meadows, Stuart Farris, Tamas Nemeth, and Biondo Biondi. DAS observations and modeling of perforation-induced guided waves in a shale reservoir. *The Leading Edge*, 38(11):858–864, 2019.

[63] Mehdi Rafiee, Mohamed Y Soliman, and Elias Pirayesh. Hydraulic fracturing design and optimization: a modification to zipper frac. In *SPE Annual Technical Conference and Exhibition*. Society of Petroleum Engineers, 2012.

[64] Craig L Cipolla, Elyezer Lolon, and Michael J Mayerhofer. Resolving created, propped and effective hydraulic fracture length. In *International Petroleum Technology Conference*. International Petroleum Technology Conference, 2008.

[65] Kevin T Raterman, Helen E Farrell, Oscar S Mora, Aaron L Janssen, Gustavo A Gomez, Seth Busetti, Jamie McEwen, Kyle Friehauf, James Rutherford, and Ray Reid. Sampling a stimulated rock volume: an Eagle Ford example. *SPE Reservoir Evaluation & Engineering*, 21(04):927–941, 2018.

[66] Shawn C Maxwell, TI Urbancic, N Steinsberger, and R Zinno. Microseismic imaging of hydraulic fracture complexity in the Barnett shale. In *SPE annual technical conference and exhibition*. Society of Petroleum Engineers, 2002.

[67] Jared Atkinson and Thomas Davis. Multicomponent time-lapse monitoring of two hydraulic fracture stimulations in an unconventional reservoir, Pouce Coupe field, Canada. In *SEG Technical Program Expanded Abstracts 2011*, pages 4097–4101. Society of Exploration Geophysicists, 2011.

[68] Kyle Haustveit, K Dahlgren, H Greenwood, T Peryam, B Kennedy, and M Dawson. New age fracture mapping diagnostic tools – a STACK case study. In *SPE Hydraulic Fracturing Technology Conference and Exhibition*. Society of Petroleum Engineers, 2017.

[69] Yamina E Aimene and Ahmed Ouenes. Geomechanical modeling of hydraulic fractures interacting with natural fractures – validation with microseismic and tracer data from the Marcellus and Eagle Ford. *Interpretation*, 3(3):SU71–SU88, 2015.

[70] A Mateeva, J Mestayer, B Cox, D Kiyashchenko, P Wills, J Lopez, S Grandi, K Hornman, P Lumens, and A Franzen. Advances in distributed acoustic sensing (DAS) for VSP. In *SEG Technical Program Expanded Abstracts 2012*, pages 1–5. Society of Exploration Geophysicists, 2012.

[71] Martin Karrenbach, Andrew Ridge, Steve Cole, Kevin Boone, Dan Kahn, Jamie Rich, Ken Silver, and David Langton. DAS microseismic monitoring and integration with strain measurements in hydraulic fracture profiling. In *Unconventional Resources Technology Conference, Austin, Texas, 24-26 July 2017*, pages 1316–1330. Unconventional Resources Technology Conference (URTEC), 2017.

[72] Gary Binder and Ali Tura. Convolutional neural networks for automated microseismic detection in downhole distributed acoustic sensing data and comparison to a surface geophone array. *Geophysical Prospecting*, 68(9):2770–2782, 2020.

[73] Harrison Schumann and Ge Jin. Inferring near-well conductivity from DAS-recorded tube waves generated by perforation shots. In *SEG Technical Program Expanded Abstracts 2020*, pages 455–459. Society of Exploration Geophysicists, 2020.

[74] Shuang Zhang, Aleksei Titov, Vikram Jayaram, Hector Bello, Robert Hurt, and Ge Jin. DAS recorded body and tube wave generated by perforation shots: Analysis and numerical modeling for completion monitoring and reservoir characterization. In *SPE/AAPG/SEG Unconventional Resources Technology Conference*. OnePetro, 2021.

[75] Menno M Molenaar, DJ Hill, Paul Webster, Erkan Fidan, and Bill Birch. First downhole application of distributed acoustic sensing for hydraulic-fracturing monitoring and diagnostics. *SPE Drilling & Completion*, 27(01):32–38, 2012.

[76] Xiaomin Zhao, Mark E Willis, Tanya Inks, and Glenn A Wilson. Quantifying hydraulically induced fracture height and density from rapid time-lapse distributed acoustic sensing vertical seismic profile data. *Geophysics*, 86(2):A15–A20, 2021.

[77] MG Bostock. Seismic waves converted from velocity gradient anomalies in the Earth's upper mantle. *Geophysical Journal International*, 138(3):747–756, 1999.

[78] Thomas Bohlen. Parallel 3-D viscoelastic finite difference seismic modelling. *Computers & Geosciences*, 28(8):887–899, 2002.

[79] Jesper Spetzler and Roel Snieder. The Fresnel volume and transmitted waves. *Geophysics*, 69(3):653–663, 2004.

[80] David WS Eaton, Robert R Stewart, and Mark P Harrison. The Fresnel zone for P-SV waves. *Geophysics*, 56(3):360–364, 1991.

[81] Bin Luo, Ariel Lellouch, Ge Jin, Biondo Biondi, and James Simmons. Seismic inversion of shale reservoir properties using microseismic-induced guided waves recorded by distributed acoustic sensing (DAS). *Geophysics*, 86(4):1–58, 2021.

[82] Juun Van Der Horst, Hans den Boer, Roel Kusters, Dayeeta Roy, Andrew Ridge, and Alastair Godfrey. Fiber optic sensing for improved wellbore surveillance. In *IPTC 2013: International Petroleum Technology Conference*, pages cp–350. European Association of Geoscientists & Engineers, 2013.

[83] Ö Haldun Ünalmis. Sound speed in downhole flow measurement. *The Journal of the Acoustical Society of America*, 140(1):430–441, 2016.

[84] G Naldrett, C Cerrahoglu, and V Mahue. Production monitoring using next-generation distributed sensing systems. *Petrophysics*, 59(04):496–510, 2018.

[85] Ge Jin, Kyle Friehauf, and Baishali Roy. Calibration of double-ended distributed temperature sensing system for production logging. In *Unconventional Resources Technology Conference, Denver, Colorado, 22-24 July 2019*, pages 3767–3778. Unconventional Resources Technology Conference (URTeC), 2019.

[86] Yehuda Taitel, Dvora Bornea, and AE Dukler. Modelling flow pattern transitions for steady upward gas-liquid flow in vertical tubes. *AIChE Journal*, 26(3):345–354, 1980.

[87] Yilin Fan, Eduardo Pereyra, Cem Sarica, Eckhard Schleicher, and Uwe Hampel. Analysis of flow pattern transition from segregated to slug flow in upward inclined pipes. *International Journal of Multiphase Flow*, 115:19–39, 2019.

[88] S Guet and G Ooms. Fluid mechanical aspects of the gas-lift technique. *Annu. Rev. Fluid Mech.*, 38:225–249, 2006.

[89] A Titov, G Jin, Y Fan, A Tura, K Kutun, and J Miskimins. Distributed fiber-optic sensing based production logging investigation: Flowloop experiments. In *First EAGE Workshop on Fibre Optic Sensing*, volume 2020, pages 1–5. European Association of Geoscientists & Engineers, 2020.

[90] Timothy Leighton. *The acoustic bubble*. Academic press, 2012.

[91] Nikolai Andrianov. A machine learning approach for virtual flow metering and forecasting. *IFAC-PapersOnLine*, 51(8):191–196, 2018.

[92] Timur Bikmukhametov and Johannes Jäschke. First principles and machine learning virtual flow metering: A literature review. *Journal of Petroleum Science and Engineering*, 184:106487, 2020.

[93] Hasan Asy'ari Arief, Tomasz Wiktorski, and Peter James Thomas. A survey on distributed fibre optic sensor data modelling techniques and machine learning algorithms for multiphase fluid flow estimation. *Sensors*, 21(8):2801, 2021.

[94] Matthew Becker, Thomas Coleman, Christopher Ciervo, Matthew Cole, and Michael Mondanos. Fluid pressure sensing with fiber-optic distributed acoustic sensing. *The Leading Edge*, 36(12):1018–1023, 2017.

[95] Aleksei Titov, Yilin Fan, Ge Jin, Ali Tura, Kagan Kutun, and Jennifer Miskimins. Experimental investigation of distributed acoustic fiber-optic sensing in production logging: Thermal slug tracking and multiphase flow characterization. In *SPE Annual Technical Conference and Exhibition*. OnePetro, 2020.

[96] Yehuda Taitel and Dvora Barnea. Two-phase slug flow. In *Advances in heat transfer*, volume 20, pages 83–132. Elsevier, 1990.

[97] EZ Massoud, Q Xiao, HA El-Gamal, and MA Teamah. Numerical study of an individual Taylor bubble rising through stagnant liquids under laminar flow regime. *Ocean Engineering*, 162:117–137, 2018.

[98] Steven James Frisken, Nader Issa, and Michael Alberic Freddy Roelens. Distributed optical sensing systems and methods, 2018. PCT Patent Application PCT/AU2018/050775.

[99] E Sidenko, A Bona, R Pevzner, N Issa, and K Tertyshnikov. Influence of interrogators' design on DAS directional sensitivity. In *EAGE Workshop on Fiber Optic Sensing for Energy Applications in Asia Pacific*, volume 2020, pages 1–5. European Association of Geoscientists & Engineers, 2020.

[100] Jihyun Yang, Jeffrey Shragge, and Ge Jin. 4D DAS fiber-coupling effects in freezing near-surface ground conditions. In *First International Meeting for Applied Geoscience & Energy*, pages 477–482. Society of Exploration Geophysicists, 2021.

[101] Stephen Ambrose, Ian S Lowndes, David M Hargreaves, and Barry Azzopardi. Numerical modelling of the rise of Taylor bubbles through a change in pipe diameter. *Computers & Fluids*, 148:10–25, 2017.

[102] AMFR Pinto, MN Coelho Pinheiro, and JBL Campos. On the interaction of Taylor bubbles rising in two-phase co-current slug flow in vertical columns: turbulent wakes. *Experiments in Fluids*, 31(6):643–652, 2001.

[103] Yaxin Liu, Eric R Upchurch, and Evren M Ozbayoglu. Experimental study of single Taylor bubble rising in stagnant and downward flowing non-newtonian fluids in inclined pipes. *Energies*, 14(3):578, 2021.

APPENDIX A

CONTRIBUTION STATEMENTS

A.1 Contribution statement for Chapter 2

Conceptualization, A. Titov, G. Binder, G. Jin, J. Simmons, and A. Tura; methodology, A. Titov, A. Tura, and G. Jin; software, A. Titov; validation, A. Titov and G. Binder; formal analysis, A. Titov; investigation, A. Titov, Y. Liu, D. Monk, G. Byerley, and M. Yates; resources, A. Tura and G. Jin; data curation, A.Titov, Y. Liu, and G. Binder; writing — original draft preparation, A. Titov; writing — review and editing, A. Titov, G. Binder, Y. Liu, G. Jin, J. Simmons, A. Tura, D. Monk, G. Byerley, and M. Yates; visualization, A. Titov and G. Binder; supervision, G. Jin and A. Tura; project administration, G. Jin and A. Tura; funding acquisition, G. Jin and A. Tura.

A.2 Contribution statement for Chapter 3

Conceptualization, A. Titov, G. Binder, G. Jin, and A. Tura; methodology, A. Titov and G. Jin; software, A. Titov; validation, A. Titov; formal analysis, A. Titov; investigation, A. Titov; resources, A. Tura and G. Jin; data curation, A. Titov; writing — original draft preparation, A. Titov; writing — review and editing, A. Titov, G. Binder, G. Jin, and A. Tura; visualization, A. Titov; supervision, G. Jin and A. Tura; project administration, G. Jin and A. Tura; funding acquisition, G. Jin and A. Tura.

A.3 Contribution statement for Chapter 4

Conceptualization, A. Titov, Y. Fan., G. Jin, A. Tura, K. Kutun, and J. Miskimins; methodology, A. Titov, Y. Fan, and G. Jin; software, A. Titov; Validation, A. Titov; formal analysis, A. Titov; investigation, A. Titov and K. Kutun; resources, A. Tura, J. Miskimins, Y. Fan, and G. Jin; data curation, A.Titov and K. Kutun; writing — original draft preparation, A. Titov; writing — review and editing, A. Titov, Y. Fan., G. Jin,

A. Tura, K. Kutun, and J. Miskimins; visualization, A. Titov; supervision, Y. Fan. and G. Jin; project administration, Y. Fan., G. Jin, A. Tura, and J. Miskimins; funding acquisition, Y. Fan., G. Jin, A. Tura, and J. Miskimins.

A.4 Contribution statement for Chapter 5

Conceptualization, A. Titov., Y. Fan., and G. Jin.; methodology, A. Titov. and G. Jin.; software, A. Titov.; validation, A. Titov; formal analysis, A. Titov; investigation, A. Titov and K. Kutun; resources, Y. Fan., and G. Jin.; data curation, A. Titov; writing — original draft preparation, A. Titov; writing — review and editing, A. Titov., Y. Fan., K. Kutun. and G. Jin; visualization, A. Titov; supervision, Y. Fan. and G. Jin; project administration, Y. Fan. and G. Jin; funding acquisition, Y. Fan. and G. Jin.

APPENDIX B

COPYRIGHT PERMISSIONS

B.1 Copyright permissions for Chapter 2

CCC | Marketplace™

This is a License Agreement between Aleksei Titov ("User") and Copyright Clearance Center, Inc. ("CCC") on behalf of the Rightsholder identified in the order details below. The license consists of the order details, the CCC Terms and Conditions below, and any Rightsholder Terms and Conditions which are included below.
All payments must be made in full to CCC in accordance with the CCC Terms and Conditions below.

Order Date	03-Dec-2021	Type of Use	Republish in a thesis/dissertation
Order License ID	1166032-1	Publisher	SOCIETY OF EXPLORATION GEOPHYSICISTS,
ISSN	0016-8033	Portion	Chapter/article

LICENSED CONTENT

Publication Title	Geophysics	Publication Type	Journal
Article Title	Modeling and interpretation of scattered waves in inter-stage DAS VSP survey	Start Page	D93
		End Page	D102
Author/Editor	SOCIETY OF EXPLORATION GEOPHYSICISTS., SOCIETY OF PETROLEUM GEOPHYSICISTS.	Issue	2
		Volume	86
Date	12/31/1935	URL	https://library.seg.org/journal/gpysa7
Language	English		
Country	United States of America		
Rightsholder	Society of Exploration Geophysicists (SEG)		

REQUEST DETAILS

Portion Type	Chapter/article	Rights Requested	Main product
Page range(s)	D93-D102	Distribution	Worldwide
Total number of pages	10	Translation	Original language of publication
Format (select all that apply)	Print, Electronic	Copies for the disabled?	No
Who will republish the content?	Author of requested content	Minor editing privileges?	No
Duration of Use	Life of current and all future editions	Incidental promotional use?	No
Lifetime Unit Quantity	Up to 999	Currency	USD

NEW WORK DETAILS

Title	Quantitative analysis of distributed acoustic sensing data for time-lapse vertical seismic profiling and multiphase flow monitoring	Institution name	Colorado School of Mines
		Expected presentation date	2022-01-14
Instructor name	Aleksei Titov		

ADDITIONAL DETAILS

Order reference number	N/A	The requesting person / organization to appear on the license	Aleksei Titov

REUSE CONTENT DETAILS

Title, description or numeric reference of the portion(s)	Geophysics	Title of the article/chapter the portion is from	Modeling and interpretation of scattered waves in inter-stage DAS VSP survey
Editor of portion(s)	Titov, Aleksei; Binder, Gary; Liu, Youfang; Jin, Ge; Simmons, James; Tura, Ali; Monk, David; Byerley, Grant; Yates, Mike	Author of portion(s)	Titov, Aleksei; Binder, Gary; Liu, Youfang; Jin, Ge; Simmons, James; Tura, Ali; Monk, David; Byerley, Grant; Yates, Mike
Volume of serial or monograph	86	Issue, if republishing an article from a serial	2
Page or page range of portion	D93-D102	Publication date of portion	2021-03-01

Figure B.1 Copy right permission from Copyright Clearance Center on behalf of *Geophysics*

From: Youfang Liu <liuyoufang@mines.edu>
Sent: Friday, December 3, 2021 2:28 PM
To: Aleksei Titov <alekseititov@mines.edu>
Subject: RE: Permission to include co-authored paper into Ph.D. thesis

Dear Aleksei,

Yes. I approve it.

Cheers,
Youfang

From: Aleksei Titov <alekseititov@mines.edu>
Sent: Friday, December 3, 2021 2:11 PM
To: Youfang Liu <liuyoufang@mines.edu>
Subject: Permission to include co-authored paper into Ph.D. thesis

Dear Mr. Liu,

Please respond to this email with your approval to reproduce our paper (Aleksei Titov, Gary Binder, Youfang Liu, Ge Jin, James Simmons, Ali Tura, David Monk, Grant Byerley, and Mike Yates. Modeling and interpretation of scattered waves in interstage distributed acoustic sensing vertical seismic profiling survey. Geophysics, 86(2): D93–D102, 2021.) as part of my Ph.D. thesis.

The screenshot of your response will be included in the appendix of my thesis as required by the Colorado School of Mines (https://www.mines.edu/graduate-studies/copyright-and-permissions/).

Best Regards,
Aleksei

Figure B.2 Permission statement from coauthor Youfang Liu.

From: James Simmons <jsimmons@mines.edu>
Sent: Friday, December 3, 2021 3:47 PM
To: Aleksei Titov <alekseititov@mines.edu>
Subject: Re: Permission to include co-authored paper in Ph.D. thesis

Aleksei,

I approve your request.

Best,
Jim

From: Aleksei Titov <alekseititov@mines.edu>
Sent: Friday, December 3, 2021 2:13 PM
To: James Simmons <jsimmons@mines.edu>
Subject: Permission to include co-authored paper in Ph.D. thesis

Dear Dr. Simmons,

Please respond to this email with your approval to reproduce our paper (Aleksei Titov, Gary Binder, Youfang Liu, Ge Jin, James Simmons, Ali Tura, David Monk, Grant Byerley, and Mike Yates. Modeling and interpretation of scattered waves in interstage distributed acoustic sensing vertical seismic profiling survey. Geophysics, 86(2): D93–D102, 2021.) as part of my Ph.D. thesis.

The screenshot of your response will be included in the appendix of my thesis as required by the Colorado School of Mines (https://www.mines.edu/graduate-studies/copyright-and-permissions/).

Best Regards,
Aleksei

Figure B.3 Permission statement from coauthor Dr. James Simmons.

From: Dave <dave@monksontheriver.com>
Sent: Friday, December 3, 2021 4:49 PM
To: Aleksei Titov <alekseititov@mines.edu>
Subject: [External] Re: Permission to include co-authored paper in Ph.D. thesis

Approved.

Dave Monk

Sent from my iPad

On Dec 3, 2021, at 3:16 PM, Aleksei Titov <alekseititov@mines.edu> wrote:

Dear Dr. Monk,

Please respond to this email with your approval to reproduce our paper (Aleksei Titov, Gary Binder, Youfang Liu, Ge Jin, James Simmons, Ali Tura, David Monk, Grant Byerley, and Mike Yates. Modeling and interpretation of scattered waves in interstage distributed acoustic sensing vertical seismic profiling survey. Geophysics, 86(2): D93–D102, 2021.) as part of my Ph.D. thesis.

The screenshot of your response will be included in the appendix of my thesis as required by the Colorado School of Mines (https://www.mines.edu/graduate-studies/copyright-and-permissions/).

Best Regards,
Aleksei

Figure B.4 Permission statement from coauthor Dr. David Monk.

From: Grant Byerley <gkbyerley@gmail.com>
Sent: Friday, December 3, 2021 5:17 PM
To: Aleksei Titov <alekseititov@mines.edu>
Subject: [External] Re: Permission to include co-authored paper in Ph.D. thesis

Hi Aleksei,

You have my permission. Good luck with the PhD. I'll be attending the RCP in person next week and hope we can meet up then!

Regards,

GRANT BYERLEY
+1 (865)-334-3232

On Dec 3, 2021, at 4:22 PM, Aleksei Titov <alekseititov@mines.edu> wrote:

Dear Mr. Byerley,

Please respond to this email with your approval to reproduce our paper (Aleksei Titov, Gary Binder, Youfang Liu, Ge Jin, James Simmons, Ali Tura, David Monk, Grant Byerley, and Mike Yates. Modeling and interpretation of scattered waves in interstage distributed acoustic sensing vertical seismic profiling survey. Geophysics, 86(2): D93–D102, 2021.) as part of my Ph.D. thesis.

The screenshot of your response will be included in the appendix of my thesis as required by the Colorado School of Mines (https://www.mines.edu/graduate-studies/copyright-and-permissions/).

Best Regards,
Aleksei

Figure B.5 Permission statement from coauthor Grant Byerley.

From: Yates, Mike <Mike.Yates@apachecorp.com>
Sent: Wednesday, December 22, 2021 10:11 AM
To: Aleksei Titov <alekseititov@mines.edu>
Subject: Re: [EXTERNAL] Re: Permission to include co-authored paper in Ph.D. thesis

Alexei,
Your request is approved by Apache.

Regards,

Mike Yates
Apache Corporation

On Dec 22, 2021, at 12:42 AM, Aleksei Titov <alekseititov@mines.edu> wrote:

Hello Mike,

I hope you are doing well.
Could you please send me approval to reproduce our paper in my thesis?

Happy Holidays,
Aleksei

From: Aleksei Titov
Sent: Friday, December 3, 2021 2:24 PM
To: Yates, Mike <Mike.Yates@apachecorp.com>
Subject: Permission to include co-authored paper in Ph.D. thesis

Dear Mr. Yates,

Please respond to this email with your approval to reproduce our paper (Aleksei Titov, Gary Binder, Youfang Liu, Ge Jin, James Simmons, Ali Tura, David Monk, Grant Byerley, and Mike Yates. Modeling and interpretation of scattered waves in interstage distributed acoustic sensing vertical seismic profiling survey. Geophysics, 86(2): D93–D102, 2021.) as part of my Ph.D. thesis.

The screenshot of your response will be included in the appendix of my thesis as required by the Colorado School of Mines (https://www.mines.edu/graduate-studies/copyright-and-permissions/).

Best Regards,
Aleksei

Figure B.6 Permission statement from coauthor Mike Yates.

B.2 Copyright permissions for Chapter 4

CCC | Marketplace™

This is a License Agreement between Aleksei Titov ("User") and Copyright Clearance Center, Inc. ("CCC") on behalf of the Rightsholder identified in the order details below. The license consists of the order details, the CCC Terms and Conditions below, and any Rightsholder Terms and Conditions which are included below.
All payments must be made in full to CCC in accordance with the CCC Terms and Conditions below.

Order Date	22-Dec-2021	Type of Use	Republish in a thesis/dissertation
Order License ID	1171131-1	Publisher	Society of Petroleum Engineers
ISBN-13	9781613997239	Portion	Chapter/article

LICENSED CONTENT

Publication Title	SPE Annual Technical Conference & Exhibition (20ATCE)	Country	United States of America
		Rightsholder	Society of Petroleum Engineers (SPE)
Date	12/31/2019	Publication Type	e-Book
Language	English		

REQUEST DETAILS

Portion Type	Chapter/article	Rights Requested	Main product
Page range(s)	1-11	Distribution	Worldwide
Total number of pages	11	Translation	Original language of publication
Format (select all that apply)	Print, Electronic	Copies for the disabled?	No
Who will republish the content?	Author of requested content	Minor editing privileges?	No
Duration of Use	Life of current and all future editions	Incidental promotional use?	No
Lifetime Unit Quantity	Up to 999	Currency	USD

NEW WORK DETAILS

Title	Quantitative analysis of distributed acoustic sensing data for time-lapse vertical seismic profiling and multiphase flow monitoring	Institution name	Colorado School of Mines
		Expected presentation date	2022-01-14
Instructor name	Aleksei Titov		

ADDITIONAL DETAILS

Order reference number	N/A	The requesting person / organization to appear on the license	Aleksei Titov

REUSE CONTENT DETAILS

Title, description or numeric reference of the portion(s)	SPE Annual Technical Conference & Exhibition (20ATCE)	Title of the article/chapter the portion is from	Experimental Investigation of Distributed Acoustic Fiber-Optic Sensing in Production Logging: Thermal Slug Tracking and Multiphase Flow Characterization
Editor of portion(s)	N/A	Author of portion(s)	Aleksei Titov; Yilin Fan; Ge Jin; Ali Tura; Kagan Kutun; Jennifer Miskimins
Volume of serial or monograph	N/A	Issue, if republishing an article from a serial	N/A
Page or page range of portion	1-11	Publication date of portion	2019-12-31

SPECIAL RIGHTSHOLDER TERMS AND CONDITIONS

The person requesting republication permission is an author of SPE-201534-MS.

Figure B.7 Copy right permission from Copyright Clearance Center on behalf of Society of Petroleum Engineers (SPE)

From: Yilin Fan <yilinfan@mines.edu>
Sent: Friday, December 3, 2021 2:44 PM
To: Aleksei Titov <alekseititov@mines.edu>
Subject: RE: Permission to include co-authored paper in Ph.D. thesis

Aleksei,

You have my approval to reproduce the paper as part of your Ph.D. thesis.

Thanks,
Yilin
--
Yilin Fan, Ph.D.
Assistant Professor
Petroleum Engineering
Colorado School of Mines
1600 Arapahoe Street,
Marquez Hall, Room#315
Golden, CO 80401-1887
Office: +1 (303) 273-3749
Email: yilinfan@mines.edu

From: Aleksei Titov <alekseititov@mines.edu>
Sent: Friday, December 3, 2021 2:30 PM
To: Yilin Fan <yilinfan@mines.edu>
Subject: Permission to include co-authored paper in Ph.D. thesis

Dear Dr. Fan,

Please respond to this email with your approval to reproduce our paper (Aleksei Titov, Yilin Fan, Ge Jin, Ali Tura, Kagan Kutun, and Jennifer Miskimins. Experimental investigation of distributed acoustic fiber-optic sensing in production logging: thermal slug tracking and multiphase flow characterization. Submitted.) as part of my Ph.D. thesis.

The screenshot of your response will be included in the appendix of my thesis as required by the Colorado School of Mines (https://www.mines.edu/graduate-studies/copyright-and-permissions/).

Best Regards,
Aleksei

Figure B.8 Permission statement from coauthor Dr. Yilin Fan.

From: Kagan Kutun <kutun@mines.edu>
Sent: Friday, December 3, 2021 3:30 PM
To: Aleksei Titov <alekseititov@mines.edu>
Subject: Re: Permission to include co-authored paper in Ph.D. thesis

Aleksei,

I approve this request.

Kagan Kutun
Colorado School of Mines
Ph.D. Candidate - Petroleum Engineering
kutun@mines.edu | 720-707-8689
https://www.linkedin.com/in/kagankutun/

From: Aleksei Titov <alekseititov@mines.edu>
Sent: Friday, December 3, 2021 2:31 PM
To: Kagan Kutun <kutun@mines.edu>
Subject: Permission to include co-authored paper in Ph.D. thesis

Dear Mr. Kutun,

Please respond to this email with your approval to reproduce our paper (Aleksei Titov, Yilin Fan, Ge Jin, Ali Tura, Kagan Kutun, and Jennifer Miskimins. Experimental investigation of distributed acoustic fiber-optic sensing in production logging: thermal slug tracking and multiphase flow characterization. Submitted.) as part of my Ph.D. thesis.

The screenshot of your response will be included in the appendix of my thesis as required by the Colorado School of Mines (https://www.mines.edu/graduate-studies/copyright-and-permissions/)

Best Regards,
Aleksei

Figure B.9 Permission statement from coauthor Kagan Kutun.